Investigation of Arterial Luminal Topography and Design of Crimped Fiber Composites

by

Nandan N Pitre

B.Tech in Engineering Design, Indian Institute of Technology Madras, 2016

M.Tech in Engineering Design with specialization in Biomedical Design, Indian Institute of Technology Madras, 2017

MS in Biomedical Engineering, Carnegie Mellon University, 2019

Submitted to the Graduate Faculty of the

Swanson School of Engineering in partial fulfillment

of the requirements for the degree of

Doctor of Philosophy

University of Pittsburgh

2023

UNIVERSITY OF PITTSBURGH

SWANSON SCHOOL OF ENGINEERING

This dissertation was presented

by

Nandan N Pitre

It was defended on

October 31, 2023

and approved by

Edith Tzeng, MD, UPMC Professor of Surgery, Department of Surgery, UPMC

Steven Abramowitch, PhD, Professor, Department of Bioengineering, University of Pittsburgh

David Vorp, PhD, Professor, Department of Bioengineering, University of Pittsburgh

Dissertation Director: Sachin Velankar, PhD, Department of Chemical and Petroleum Engineering, University of Pittsburgh

Investigation of Arterial Luminal Topography and Design of Crimped Fiber Composites

Nandan N Pitre, PhD

University of Pittsburgh, 2023

The lumen of arteries usually appears corrugated in histological cross-sections. These corrugations occur due to the wrinkling of the Internal Elastic Lamina (IEL) and have often been attributed to fixation artefacts. We quantify the IEL topography and test whether the corrugations are actually present in arteries under physiological conditions. This is done by imaging cross-sections of fixed arteries at different diameters and comparing them to the diameter measured in-vivo using ultrasound. It is seen that the IEL corrugations flatten out as the arterial diameter increases, and the IEL contour length is ~10% more than the circumference at ultrasound diameter. These results provide evidence that the luminal topography is not completely flat under physiological conditions.

Fibrous collagen exists in biological tissues in the form of crimped fibers. This crimped nature of fibers enables them to uncrimp before stretching and provide an increased stiffness as the tissue stretches, thus imparting 'strain-hardening' behavior to the tissues. Composites of soft material embedded with short stiffer crimped fibers have the potential to show similar mechanical behavior and have the advantage of being flow processible. Here we study the mechanics of crimped fiber composites by quantifying the stress transfer between a single crimped fiber and a an embedding soft matrix, and examining the mechanical response of crimped multifiber composites under tension, using 3D finite element analysis.

As the composite is stretched, fibers with large crimp amplitude and large relative modulus straighten significantly at small strains without bearing significant load. Thus, crimped fiber composites show a super-linear increase in stress upon tension. Stress-transfer mechanics of a crimped fiber are captured using a shear lag model, where the crimped fiber can be replaced by an equivalent softer straight fiber with increasing strain-dependent modulus. Multifiber composites show that higher fiber volume fraction yields higher reinforcement. Moreover, maximum reinforcement is achieved when the fibers are oriented along the direction of the stretch. Thus, the degree of strain-hardening and the degree of reinforcement of multi-crimped-fiber composites can be tuned by changing fiber parameters to achieve the desired mechanical behavior of the composite.

Table of Contents

List of Tables

List of Figures

Preface

It is my honor to present here my research work over the duration of my doctorate program. Firstly, I would like to express my gratefulness to my advisor, Dr. Sachin Velankar for guiding me through this time. I was fortunate to get the opportunity to work with Dr. Velankar; and his interest, efforts and guidance in my work helped me not only develop a good understanding of the subject but also a very strong passion to keep going in the field of research. Our regular meetings and discussions gave me an insight into objective thinking and taught me much more than just the science of the subject. In Dr. Velankar's Lab, I got the opportunity to conduct both experimental and computational studies as well as develop theoretical models and I thank him heartily.

I want to thank my co-advisor, Dr. Edith Tzeng for giving me the opportunity to work more closely with the medical side of biomedical engineering. Dr. Tzeng's insights and knowledge guided me in every step of my research, and it was my privilege working with her. I got the opportunity to work with biological materials and animals as part of our collaborative work. I would like to thank Dr. J B Moses and Dr. Derek Afflu for teaching me skills like tissue dissection and fixation, which were crucial to this work. Dr. Moses also helped and guided me in the collaborative projects that we were part of.

I would like to thank Dr. Steven Abramowitch for his huge contribution to my research. Dr. Abramowitch taught and advised me regarding the computational aspect of the study, and I learnt how even computationally huge simulations can become fun and illuminating. I thank Dr. Abramowitch for sparing me so much of his time and taking an interest in my work. It was a privilege to collaborate with him.

I thank Dr. David Vorp for agreeing to be on my thesis committee and for giving invaluable feedback regarding the work. I am fortunate to be presenting my research to him and taking his valuable advice. I would like to thank Dr. Sanjeev Shroff and Dr. Vorp for making me part of the Cardiovascular Bioengineering Training Program (CBTP), where we were exposed to highly interesting research in the cardiovascular field as well as got the opportunity to hear from excellent researchers in the field.

I want to thank my advisors in Master's program, Dr. Keith Cook (Carnegie Mellon University), Dr. R Krishna Kumar (IIT Madras) and Dr. K R Balakrishnan (Fortis Malar Hospital, Chennai) for inspiring me in the field of cardiovascular and respiratory mechanics and computational analysis. Their efforts and guidance helped me find my liking and interest in the subject.

I want to thank Dr. Siamak Salvatian, Dr. Aman Mahajan for enabling us to work with animals for the research. I also want to thank Dr. Yuki Kuwabara and Madison Fischer for helping me with the surgical part of the animal study. I also heartily thank Dr. Simon Watkins and everyone at the Center for Biologic Imaging (CBI), UPMC for enabling us to work with the microscopes and imaging instruments, which was an inherent part of this research. I thank Andrew Holmes for helping us with our fabrication and for training and providing us with machine shop facilities which facilitated implementation of our ideas into physical systems. I also thank Dr. Neeraj Gandhi and the Bioengineering department for their support and cooperation during my time at University of Pittsburgh.

I want to thank the people I worked with in Dr. Velankar's lab: Dr. Joseph Pugar, Dr. Nhung Nguyen and Dr. Rahul Ramachandran for helping me with doubts and questions regarding my work; and Luke Barnett and Dylan Buttler for working with me on the experimental portion

of the work. I would like to thank all my lab mates for supporting me and sharing their research ideas during our meetings.

I want to thank Prof. M Prakash with whom I learnt the fundamentals of mathematics and learning, and who has a huge contribution in my life. I want to thank my physics professor Sanjeet Singh Adarsh for showing how wonderful physics can be and for creating in me a great curiosity and passion towards the subject.

I would once again like to thank everyone on my committee for their mentoring, support and valuable input during our meetings. It is an honor to present my research to them.

I would like to thank my parents and family for their support during my PhD. Lastly, I want to thank my friends for being my family during my college days and here in Pittsburgh, and for making this journey so enjoyable. I am very grateful for their love and support.

“Thankful to those who taught,

And grateful to those I’ve learnt from…

For the ‘me’ that I say has learnt,

Is but a projection, and that will go.

But the learning

And the gratefulness

Will stay on…”

Introduction to Dissertation

This dissertation examines two aspects of the straightening of thin wavy structures under tension. Both aspects are related to vascular mechanics, in one case the actual microstructure of arteries, and in the second case, in the mechanics of materials that mimic arterial tissue. The internal elastic lamina (IEL) in arteries serves as the wavy structure in the study in Part 1, and we investigate the role it plays in the morphology of the arterial lumen. Here, arterial luminal topography and its relevance under physiological conditions is investigated. In Part 2, mechanics of the arterial tissue are considered with the primary goal of designing a synthetic tissue substitute that can mimic the mechanical behavior of the arterial wall and other soft tissues which show strain-hardening properties. Here crimped fibers embedded in a matrix serve as the wavy structure, and their effect on the mechanical behavior is studied.

Part 1

Part 1 consists of investigation into the microstructure observed in arteries. It has been known for many decades that cross-sections of fixed arteries that are imaged under microscope show that the inner lumen is wrinkled. However, these images necessarily require extraction of the arteries from the body. Biological tissues like arteries undergo changes when taken out of the body, both because many factors in vitro are different as compared to in vivo (e.g. excision causes loss of luminal pressure) as well as preparation methods (e.g. dehydration during fixation). Thus, these wrinkles of the lumen have often been attributed to artifacts due to fixation, handling and other changes in temperature and moisture. However, since imaging the arterial lumen at high resolution is not possible in vivo, the issue of whether these structures are indeed an artifact, or are they

present under physiological conditions remains unresolved. Our approach starts with the idea that the IEL corrugations are a geometric and mechanical effect. Thus, we seek to examine fixed arteries at the same diameter as they used to be prior to excision. This study is conducted on porcine carotid arteries and the in-vivo measurements of arterial diameter are done using ultrasound. Here we also develop an innovative way of fixing the arteries in conical segments that allows us to obtain a range of diameters for the same artery in order to evaluate how the IEL topography changes with the blood vessel diameter. Chapter 1 presents this study along with a discussion of the results.

Part 2

Biological tissues contain fibrous collagen which exists in the form of crimped fibers in unstressed state. This crimped state allows the fibers to uncrimp before stretching, thus imparting a strain-hardening behavior to the tissue. A composite reinforced with crimped fibers may be considered as a biomimetic analog of collagenous tissues. Short fibers (often glass or carbon fibers) are often used as reinforcing fillers in composites. In the context of soft materials however, if the fibers are crimped and embedded in a soft matrix, it may be possible to achieve mechanical behavior similar to that of biological tissues, where the composite stiffness increases super-linearly with stretch. Such a composite material may have potential applications as synthetic tissue substitutes, but being composed of chopped fibers, would still be flow-processible. In Part 2, we look at such short crimped-fiber composites and their mechanical behavior.

In order to control and predict the behavior of these composites, it is necessary that to understand the mechanics underlying how crimped fibers contribute to the mechanical response of the composite. Here we present two studies examining the composite mechanics.

As the first step in understanding the mechanics of crimped fibers, in Chapter 2, we conduct a computational study of the stress transfer occurring between a single finite-length crimped fiber and the soft matrix within which it is embedded. Different parameters of the crimped fibers are tested for their effect on fiber loading. Here we look at whether crimped fibers initially uncrimp without bearing significant load and become increasingly load-bearing as they straighten out. This behavior would validate the use of crimped fibers as strain-hardening reinforcers. We also look at the end-effects of the fiber, specifically the extent to which the portion near the ends of the fiber is less load bearing, as is known to happen for straight fibers. At the end of this chapter, we discuss how the shear lag model can be modified to form a model for crimped fibers, and the concept of an Equivalent Straight Fiber (ESF) model is developed. A further study into the reduction in fiber crimp amplitude that occurs as the composite is stretched is presented in Section 1.01(a)(i)Appendix C, along with experimental verification.

In chapter 3, we extend this study to the case where there are multiple such crimped fibers embedded in a soft matrix. This is also a computational study using 3D finite element simulations. The parameter space is wider and includes the volume fraction of fibers as well as their alignment. We look at how the orientation of fibers in the composite affects the degree of strain-hardening. In this study we discuss how some computational models can be used to predict these multifiber simulation results. Here we also develop a computational workflow that can efficiently generate highly complex geometries of composites with dispersed crimped fibers, with control of alignment and fiber geometry while still having random placement of fibers. We also provide an experimental verification of the results, where actual multi-crimped-fiber composite samples are created and tensile stretched.

At the end of Part 2, we have a mathematical basis and experimental verification for a short crimped fiber reinforced composite material with tunable properties to match a range of mechanical behaviors.

This can then be extended to developing vascular prosthesis as well as synthetic substitutes for other tissues. Combining with the study in part 1 and Appendix B, which shows a method for fabricating tubes with luminal topography, vascular grafts can be fabricated with luminal topography as well as matching the mechanical behavior of arteries.

Chapter 4 summarizes the research in this dissertation and discusses the ways in which it can be taken further, as well as the limitations and challenges that need to be addressed in doing so.

Part 1

Relevance of Internal Elastic Lamina Corrugations Under Physiological Conditions

Overview

A variety of complex microstructures are often seen in images of biological tissues. Many of these can only be observed after the tissues are taken out of the body and the tissues are fixed. Then the question remains: are they actually present in the body, or are they an artifact of the process by which they are observed? And do they have a potential biological function?

The focus of this chapter is on the wrinkled microstructures seen on the luminal surface of fixed arterial cross-sections. In Part 1, we look at this aspect, where we investigate the presence and the relevance of luminal corrugations in arteries. Although known that these are caused by the wrinkling of the Internal Elastic Lamina, little evidence exists with regards to answering the above questions: are they present in a normal functioning body, and do they have a biological function. Here, we study porcine arteries which are inflated to diameters comparable to the in-vivo measured diameters and compare the topography, in order to answer the question: do IEL corrugations exist under physiological conditions?

The following schematic illustrates the logical flow of this study.

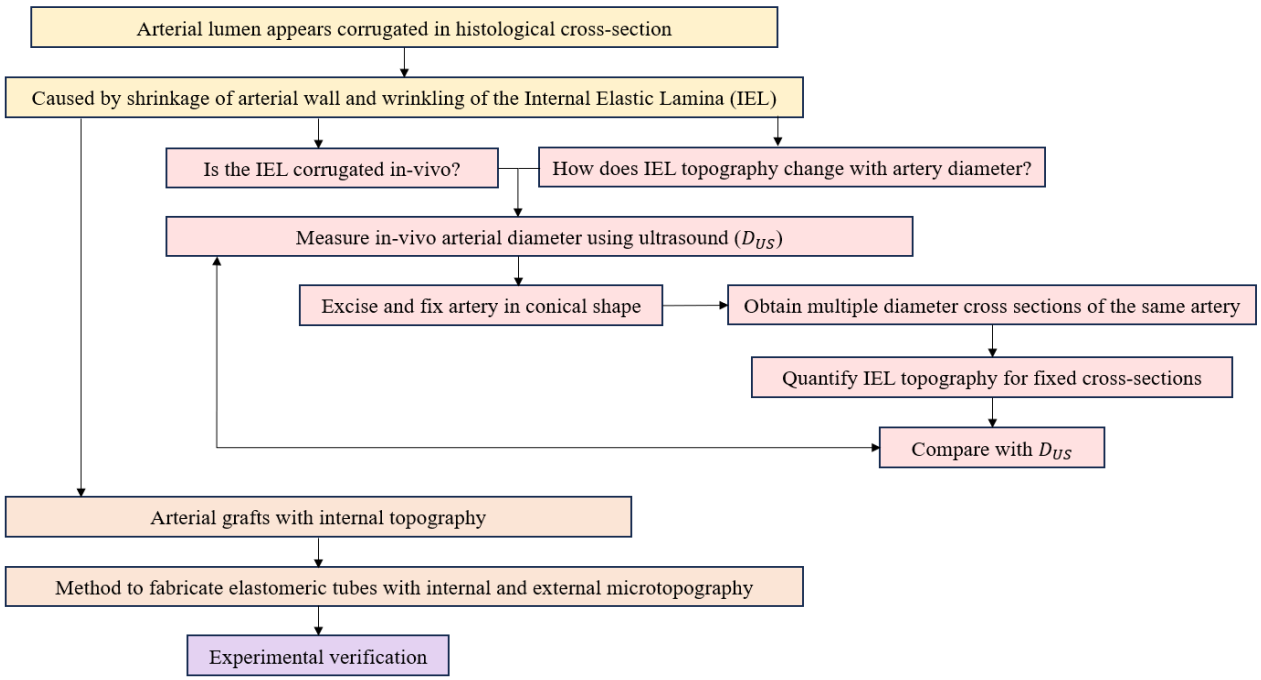

1.0 Investigation of the Relevance of Internal Elastic Lamina (IEL) Corrugations Under Physiological Conditions

1.1 Introduction

Muscular arteries are multi-layered structures: the innermost intima, followed by the media, and the outermost adventitia [1-5] (Figure1. 1). The intima consists of a continuous layer of endothelial cells lining the lumen of the artery. The media consists of elastin lamellae, collagen fibers and smooth muscle cells, and the adventitia primarily consists of large bundles of crimped collagen fibers and fibroblast cells, and anchors the artery to the surrounding tissue [1-5]. Between these two layers is the media, which consists of multiple layers of elastin and smooth muscle cells oriented circumferentially interspersed with collagen fibers. The number of elastin layers varies with the size and function of the artery. However, all arteries have an internal elastic lamina (IEL) that separates the intima from the media[2, 4]. This layer is comprised by roughly 79% elastin[6] and is much thicker in large arteries than in arterioles [2, 6]. The IEL includes fenestrations of around 3-4 μm in diameter [7] which are needed for mass transport between the intimal and medial layers [7, 8].

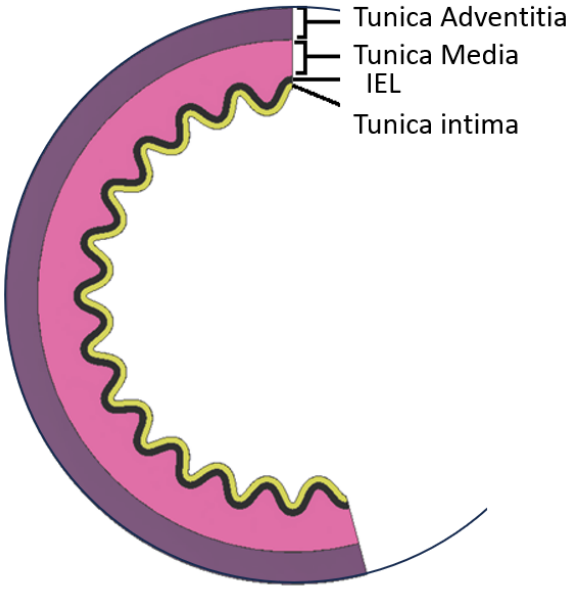

Figure1. 1 Cartoon schematic showing layers of artery

In most histological cross-sections of arteries[9-19], the IEL appears to be heavily corrugated with wavelengths on the order of a few tens of microns (example Figure1.2). The literature from 1930 to the late 1980's revealed the presence of arterial luminal corrugations by optical or electron microscopy as summarized by Tindall and Svendsen[19]. These corrugations were thought to be an artifact of the fixation process, attributable to the vasoconstriction that occurs when arteries are extracted and preserved [20-22]. Our study was initiated to determine if these IEL corrugations exist in vivo under physiological conditions[19] or if they are indeed a fixation artifact.

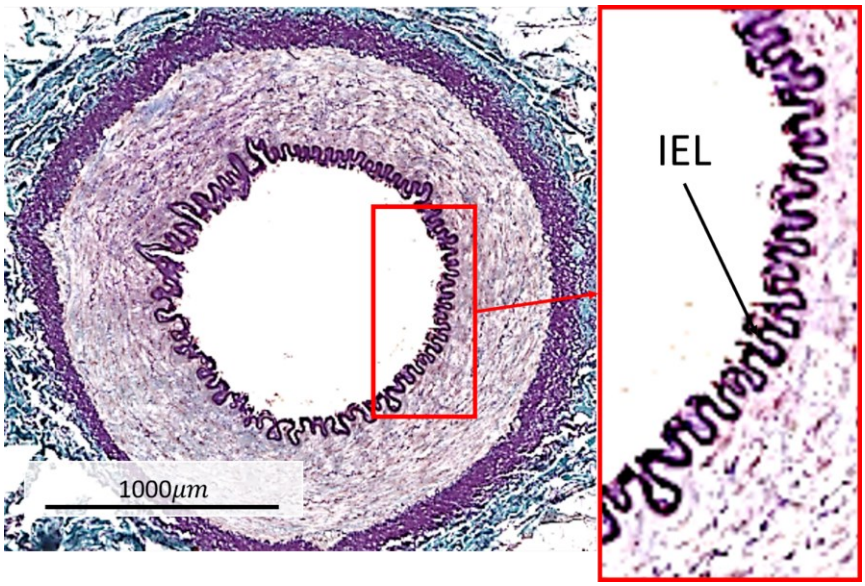

Figure1. 2 Histological arterial cross-section

Left pericardiacophrenic artery (image source: University of Michigan histology library (License: CC BY-NC-SA 4.0 Deed))

This question of whether corrugations exist in vivo is difficult to address by experiments on live animals. Corrugations on the order of a few tens of microns are too small to detect using current noninvasive imaging techniques such as ultrasound imaging. Invasive techniques such as optical coherence tomography or intravascular ultrasound also lack the necessary resolution. While microCT imaging can reach these resolutions, the dynamic nature of arterial pulsations makes the technique unsuitable for in vivo imaging. Ex vivo studies of fixed arteries allow the corrugated structure visualized with exquisite precision, but most fixation processes can induce significant distortion of the tissues. Moreover, arteries undergo vasoconstriction in the setting of hypotension, dehydration, tonus of the arterial wall, hypoxia, hypothermia, or from handling during tissue isolation and fixation[20-28].

In vitro studies have also examined how the amplitude of the corrugations become smaller as arteries are distended. Lee and Chien [13] held canine carotid arteries (roughly 1.5 mm inner diameter) at various pressures up to 100 mm Hg during fixation. Scanning electron microscopy

revealed that the lumen was heavily corrugated at 0 mm Hg with typical corrugation width and height being 15 μm and 10 μm, respectively. These corrugations became shorter in amplitude with increasing luminal pressure (and hence increasing diameter) but were still clearly visible at 60 mm Hg. Their amplitude reduced sharply at 80 mm Hg and was nearly flat at 100 mm Hg.

Greensmith and Duling [11] examined smaller vessels using arterioles of typical inner diameter 80 μm. Unlike Lee, the vessels were tuned not by varying luminal pressures. Instead, norepinephrine was used to vasoconstrict the vessels while maintaining a fixed transmural pressure of 50 mm Hg. By using the vasoconstrictor, the vessels could be constricted to diameters below their unstressed diameter. Corrugations appeared when vessels were 110-125% of their unstressed diameter and the arteries became highly corrugated when they were less than 90% of their unstressed diameter. The corrugations were typically several microns wide and several microns in amplitude.

Finally as a portion of a computational study on buckling phenomena in tissues [29], we reported measurements of pig carotid arteries of typical diameter 4 mm. As in Lee et al, the arteries were fixed while being held at various luminal pressures of up to 160 mm Hg. The arteries were observed to be very corrugated (34 μm peak to peak distance between the corrugations and 20 μm amplitude) at pressures below 100 mm Hg, but rapidly lost amplitude above 125 mm Hg.

These and other studies agree that for arteries ranging from a few mm to less than 100 μm in diameter, the corrugation amplitude increases with decreasing diameter or luminal pressure. This raises the question of whether arteries are sufficiently distended that they are smooth or are insufficiently distended such that they retain significant corrugations under physiologic conditions. Although this question of whether arteries are corrugated in vivo was specifically discussed by

Tindall and Svendsen with evidence "for" and "against" this structure, they did not come to a definitive conclusion.

Before proceeding, it is useful to clarify the mechanics underlying a corrugated topography. Composed primarily of elastin, the IEL is much stiffer than the underlying medial smooth muscle cell layer. Thus, the near-lumen mechanics is expected to follow that of layered composites comprising a thin stiff layer bonded to a thicker but softer layer. Under compressive loading, the thin stiff layer responds by deforming (rather than compression) and these corrugations grow in amplitude. Indeed, similar stiff-on-soft layer mechanics is also responsible for the wrinkling of skin. In the extreme case when the modulus mismatch is large, the stiff layer may behave as an "inextensible" layer, i.e. accommodate the compression entirely by bending without bearing any compressive strain. In this limiting case, the topographic corrugations become a geometric effect, i.e. the corrugations solely depend on the diameter of the blood vessel. Accordingly, any mechanism that causes arterial shrinkage such as loss of pressure upon excision or vasoconstriction, would also induce the IEL to become corrugated. That the IEL mechanics follow stiff-on-soft layer mechanics is implicit in the previous literature, although it has not been explicitly stated.

This physical picture also suggests that the question of physiological relevance may be addressed by quantifying the ratio:

$$\frac{contour\ length\ of\ IEL}{physiological\ luminal\ circumference}$$

The denominator is the reference value against which the IEL contour length is compared. A ratio exceeding 1 would imply that the IEL cannot remain smooth under physiological conditions. In fact, a similar ratio was used for quantification by Greensmith and Duling who used the zero-pressure diameter, and by Svendson and Tindall, who used a luminal circumference

calculated from external measurement of in vivo diameter for normalizing (rather than the physiological diameter).

Our approach is as follows: We measure the physiological diameter in a live animal under anesthesia using ultrasound measurements. We then extract and fix the artery at various diameters. Quantitative image analysis is done to measure the IEL length and compare it against the physiological diameter. One significant aspect of this research is that we greatly reduce the uncertainty in our measurements by fixing a single artery at a variety of diameters. In contrast, in previous research on this topic, a different artery had to be used at each different diameter. Thus, the reference value for comparison varied in each specimen, thus leading to greater uncertainty in the measurements.

1.2 Methods

1.2.1 Data Collection

Artery diameters were measured in vivo using GE Vscan Air^{TM} ultrasound. Carotid arteries (Left Carotid (LC) and Right Carotid (RC)) in pigs between the weights of 40 and 55 kgs were imaged. The animals were part of other experimental research unrelated to this article and did not involve the carotid arteries. Ultrasound imaging was conducted under general anesthesia (Isoflurane, 2% with 2.5 l/min O_2) and prior to any surgical process. After euthanasia, the imaged arteries were harvested. A total of 9 arteries from 6 animals were included in this study.

The excised arteries were rinsed in saline and the surrounding tissue was surgically removed. The arteries were mounted on the luer connectors in the inflation setup and secured in

place. Figure1. 3(A) is a diagram depicting the inflation setup while Figure1. 3(B) shows a photograph of the actual setup. 3D printed rigid conical sleeves were placed over the artery before inflating as shown in Figure1. 3 (C). These conical sleeves were designed to have inner diameter ranging from 3 mm on one end to 7 mm on the other. These sleeves ensured that inflation of the covered section of the artery is restricted to the inner diameter of the sleeve. Additional conical sleeves were sometimes used upon an artery if the length of the excised artery allowed (Eg. Figure1. 3 (C) shows an artery with 3 conical sleeves). This allowed us to obtain additional conical sections on the same artery which offered additional spare cross-sections, although one conical section was sufficient for analysis. One end of the artery was connected to the air outlet while the other end was closed off using a luer stop. The arteries were then subjected to pulsatile inflation cycles so as to relax the constricted artery to allow distension when pressurized. Standard tissue fixation protocol was followed for fixing the arteries under inflation. The arteries were filled with 4% paraformaldehyde, while being immersed in the same solution and inflated to a high pressure for 1 hour. This pressure was regulated so that the arteries had maximum contact with the conical sleeve without damaging the tissue. After 1 hour, the arteries were emptied of the solution, and filled with and immersed in 30% sucrose in phosphate buffer solution (PBS) for 24 hours. After fixation, the arteries were then taken off the setup and stored at -80° C. Figure1. 4 shows artery (P10322 LC) fixed using the above method, showing conical segments where the sleeves restricted expansion. The central benefit of this approach is that it allows *the same* artery to be examined across a range of diameters that encompass the range of diameters measured by ultrasound on the anesthetized animal. A secondary benefit is that since the arteries are pressed against a circular surface during fixation, their cross-sections remain almost perfectly circular which facilitates further data analysis.

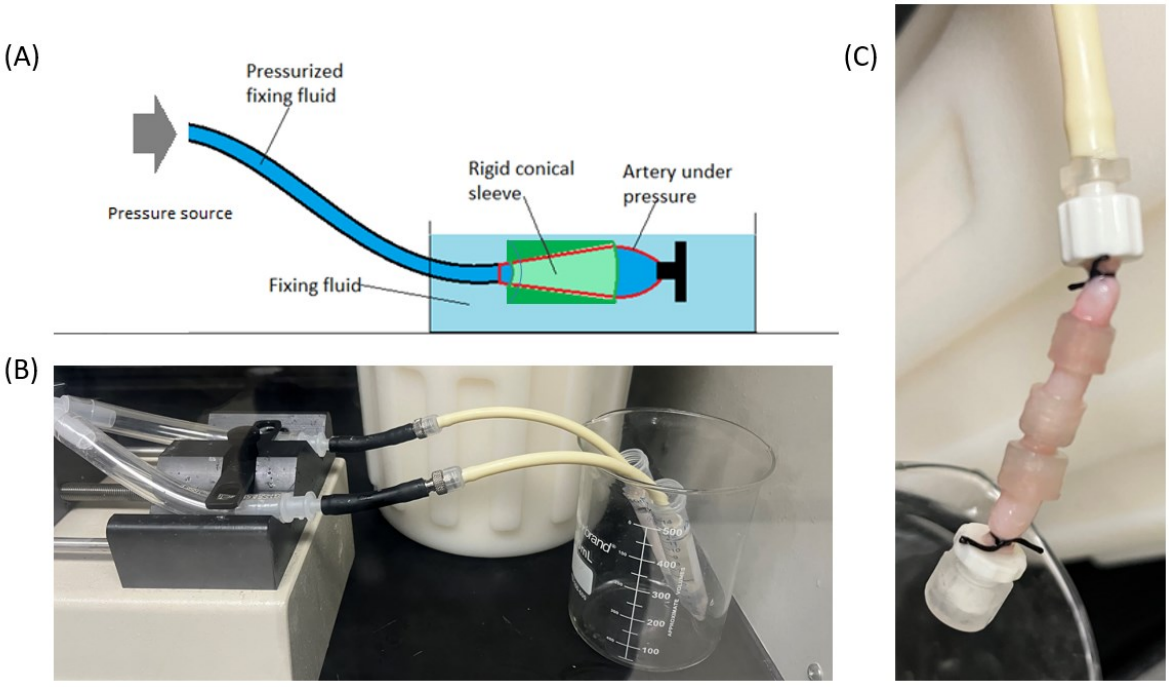

Figure1. 3 Artery inflation-fixation setup

(A) Conceptual cartoon of the inflation setup, (B) Actual experimental setup, and (C) Inflated artery with 3D printed conical sleeves, filled with fixation fluid

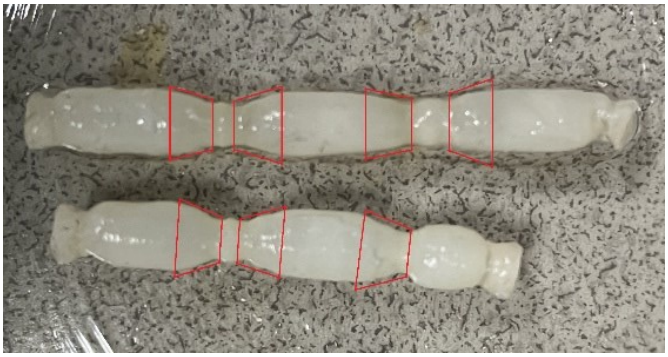

Figure1. 4 Fixed porcine arteries

P10322 Right and Left Carotid: showing conical segments where the sleeves were present (indicated by red trapeziums)

10 µm thick sections were taken from the conical part of the frozen arteries. 2-3 sections were taken at each diameter for 4-5 different diameters along the length of the conical part. To observe the effect of vessel diameter on the luminal corrugations, sections at different diameters

were imaged. The range of diameters was chosen such that the diameter of artery observed in the ultrasound lies between the smallest and largest section and at least one section has a diameter close to that observed in vivo. These included diameters small enough to observe heavy corrugations to larger ones where the IEL had flattened out. The inflation setup allowed getting circular cross-sections of the same artery at different luminal diameters. The artery sections were imaged under Nikon A1 spectral confocal microscope. Auto-fluorescence of elastin was used to image the IEL. The thickest innermost layer of elastin in the images was considered for IEL topography analysis. Figure1. 5 (A to C) shows representative confocal images of artery sections (P723 LC) at different diameters, and the magnified view below each image shows the degree to which the IEL corrugations flatten as the artery diameter increases. We emphasize that all three images were obtained from the same artery.

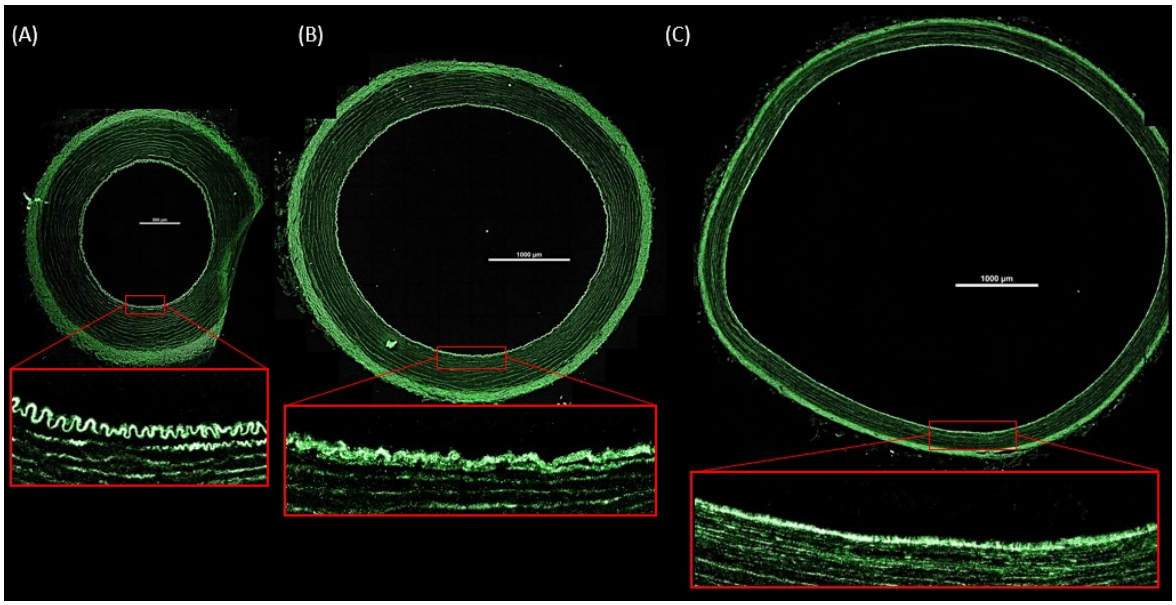

Figure1. 5 Confocal images of arterial cross-sections

(A to C) Confocal images of artery (P723 LC (cross-sections # 1, 3 and 5)) at increasing diameters and zoomed in view (red box) of the IEL

1.3 Data Analysis and Results

For each image, the degree of IEL corrugations (the quantity C_f defined below) and the degree to which the cross section is compressed with respect to the diameter measured by ultrasound were measured. To do so, the images were first converted to binary and the IEL layer was isolated (Figure1. 6 (A)). Boundaries of the isolated IEL were then converted to XY data. The center of the arterial cross-section was calculated and the XY data was then converted to polar coordinates (r, θ). The inner and outer boundaries were thus separated and an average radius (r_{avg}) was calculated from this data. This gave us the average cross-section diameter ($D_{avg} = 2\, r_{avg}$). D_{avg} was normalized by the diameter observed in ultrasound (D_{US}) and the various values of D_{avg}, D_{US} and their ratios are shown in Table 1.1. Figure1. 6 (B) shows the XY data of the isolated IEL along with the circle of radius, $r = r_{avg}$. Figure1. 6 (C) shows the inner and outer boundaries of the corrugated IEL along with r_{avg} when converted to polar coordinates. Resolution of the images was 1000x1000 ($\pm$ 50) pixels. Scalebars from the images were also converted to XY data for converting pixel data to mm scale.

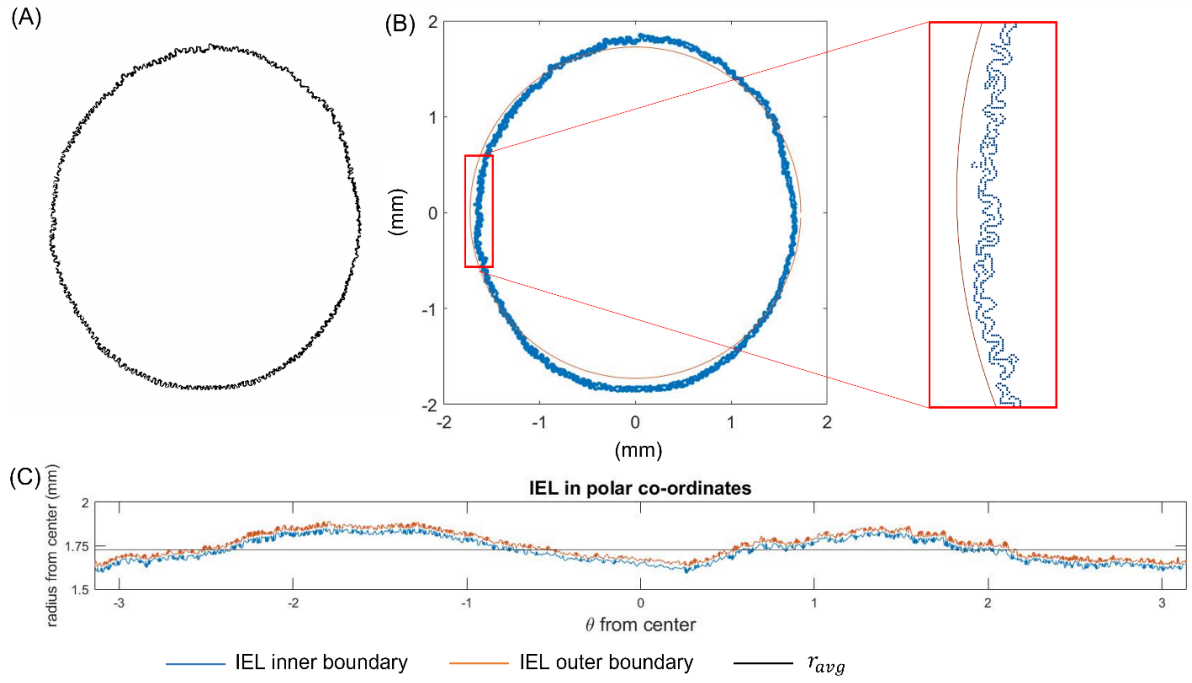

Figure1. 6 Data analysis for arterial cross-sections

(A) Isolated IEL binary image, (B) IEL mapped with fitted circle of radius, $r = r_{avg}$ and zoomed in view (red box), and (C) IEL inner and outer boundary mapped in polar coordinates with r_{avg}, for a section of the artery (P723 LC, cross-section #1 ($C_f = 2.68$))

The non-corrugated circumference (L_{avg}) and the diameter (D_{avg}) of the arterial cross-section was calculated using r_{avg}. Contour length of the IEL (L_c) was calculated using the inner boundary of the isolated IEL in polar coordinates (Figure1. 6(C)). These quantities are shown schematically in Figure1. 7.

$$L_{avg} = \pi D_{avg}$$

$$L_c = \sum (\Delta\theta . r)^2 + \Delta r^2$$

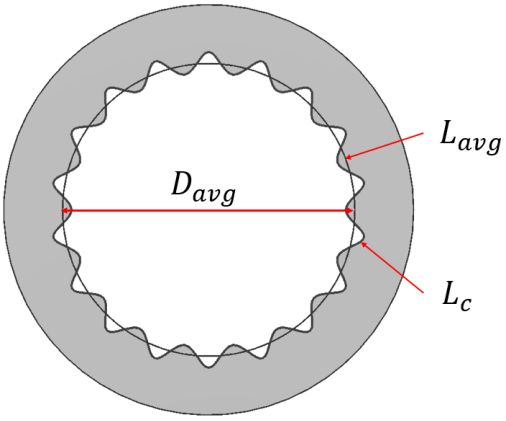

Figure1. 7 Schematic of arterial cross section showing calculated quantities D_{avg}, L_{avg} and L_c

The degree of corrugation then was calculated using the quantity Corrugation factor, C_f, defined as the ratio of the IEL contour length to the non-corrugated circumference of the cross-section.

$$C_f = \frac{L_c}{L_{avg}} = \frac{L_c}{\pi D_{avg}} \tag{1.1}$$

$C_f > 1$ indicated the presence of a corrugated IEL whereas $C_f = 1$ indicated that the corrugations had flattened out. The values of C_f for the various cross sections are listed in the last column of Table 1. 1, and the dependence of C_f on D_{avg}/D_{US} is shown in Figure1. 8 (A).

Corrugation factor (C_f) for all cross-sections of successfully imaged arteries was compared against the normalized diameter of the cross-section, normalized by the diameter observed in ultrasound imaging (D_{US}), shown in Figure1. 8. The average corrugation amplitude was measured from the cross-sections, compared with the normalized diameter in Appendix A Figure 2. Table 1. 1 lists all the measured and calculated quantities for the cross sections, and Appendix A Figure 3 shows the range of D_{avg}/D_{US} obtained for the different arteries.

Table 1. 1 Calculated quantities from arterial cross-section images

Pig ID	Artery	D_{US} (mm)	Cross-section image #	D_{cs} (mm)	D_{cs}/D_{US}	Amp (μm)	C_f
10322	LC	4.8	1	2.51	0.52	8.47	1.56
			2	2.60	0.54	7.28	1.51
			3	2.61	0.54	6.21	1.50
			4	4.23	0.88	4.22	1.23
			5	4.73	0.99	2.54	1.07
12422	LC	4.73	1	1.03	0.22	12.05	3.17
	RC	5.19	1	1.34	0.26	9.72	3.16
			2	2.28	0.44	7.36	1.89
			3	2.27	0.44	7.48	1.75
			4	3.48	0.67	7.94	1.42
			5	4.10	0.79	5.84	1.22
			6	5.48	1.06	2.74	1.10
12622	LC	3.76	1	1.45	0.39	10.18	2.56
			2	2.46	0.66	5.04	1.30
			3	3.47	0.92	3.34	1.22
			4	4.58	1.22	2.59	1.04
	RC	4.96	1	1.34	0.27	11.01	2.87
			2	2.55	0.51	5.54	1.37
			3	3.41	0.69	4.03	1.28
			4	4.98	1.00	3.04	1.09
723	LC	4.77	1	1.73	0.36	9.24	2.68
			2	2.17	0.46	9.21	2.00
			3	3.30	0.69	7.84	1.34
			4	3.19	0.67	7.16	1.42
			5	4.93	1.03	2.84	1.11
			1	2.56	0.54	8.61	1.58

	RC	4.73	2	3.21	0.68	6.78	1.09
			3	4.02	0.85	3.52	1.08
			4	5.40	1.14	2.74	1.08
3523	LC	4.59	1	1.42	0.31	8.19	3.21
			2	2.12	0.46	6.22	1.57
			3	4.30	0.94	4.52	1.10
			4	5.05	1.10	2.94	1.10
3623	RC	4.23	1	2.19	0.52	8.42	1.51
			2	2.53	0.60	8.24	1.34
			3	3.66	0.87	5.01	1.11
			4	4.43	1.05	2.86	1.07

1.4 Discussion

As expected, C_f reduces, and hence the degree of corrugations reduces, as arteries expand (Figure1. 8 (A)). Some of the arterial cross sections are severely compressed with respect to the ultrasound-measured diameter, with Cf values reaching as high as 3. These are of questionable practical relevance, and certainly not relevant to the question of whether the IEL is corrugated under physiological conditions. Accordingly, we now focus only on relatively modest Cf values (Figure1. 8 (B)).

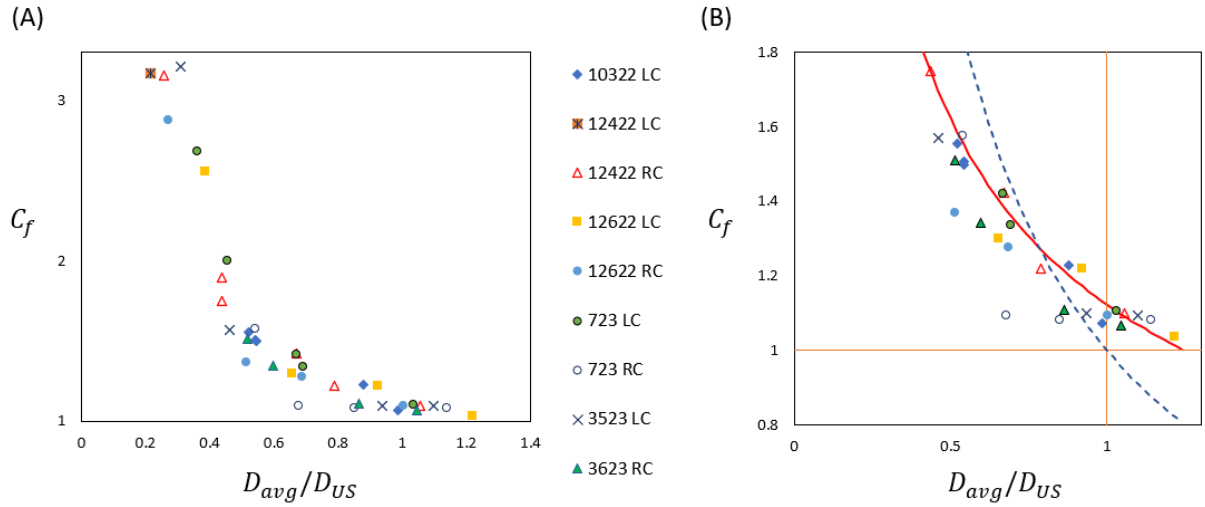

Figure1. 8 Dependence of C_f on D_{avg}/D_{US}

(A) Showing C_f *vs* D_{avg}/D_{US} for all arterial cross-sections (colored dots), (B) A subset of the data magnifying the region with $C_f < 1.6$

The vertical line in Figure1. 8 (B), drawn at $D_{avg}/D_{US} = 1$, represents a fixed arterial cross section matches that measured by the ultrasound. The data in Figure1. 8 seem to cross this line with an intercept of approximately 1.1 suggesting that the IEL is 10% longer than the circumference for a diameter measured by ultrasound.

Before discussing the data further, it is important to emphasize that the C_f defined in Eq. 1.1 is not a direct measure of amplitude, but a measure of how the contour length of the IEL compares with the circumference of the artery as measured by ultrasound. As mentioned in the introduction, the simplest mechanical picture of corrugation mechanics is to treat the IEL as an inextensible layer. In that case, Eq. 1 can be rewritten as

$$C_f = \frac{L_c}{\pi D_{US}} \left(\frac{D_{US}}{D_{avg}} \right)^{-1} \tag{1.2}$$

Motivated by this, we sought to compare Figure1. 8 (B) against

$$C_f = a\left(\frac{D_{US}}{D_{avg}}\right)^{-b} \tag{1.3}$$

The dashed blue line corresponds to $a = 1$ (or equivalently $L_c = \pi D_{US}$) and $b = 1$. This represents an inextensible IEL which the corrugations disappear *exactly* at the diameter of the ultrasound experiment. The experimental values clearly deviate upwards from the data in the vicinity of $\frac{D_{US}}{D_{cs}} = 1$ (i.e. the arteries are significantly corrugated as the diameter approaches the ultrasound value), but C_f also has a weaker dependence on $\frac{D_{US}}{D_{cs}}$ than expected. By trial and error, we find that $a = 1.1$ and $b = 0.5$ give reasonable fits to the data (two other pairs of parameters: ($a = 1.06\,;\ b = 0.6$ and $a = 1.12\,;\ b = 0.4$) also give reasonable fits. Values of a less than 1.06 fall below all of the rightmost points in Figure1. 8 (B) regardless of the value of b. While one may consider other variations to Eq. 1.2 which allow more than two parameters, these do not capture the data any better than Eq. 1.3.

The fact that values less than 1.06 are unable to capture the data suggests that the IEL is longer than the circumference corresponding to the ultrasound-measured diameter. Further, since the data are far better captured by values of b much less than 1 suggest that the IEL is not strictly inextensible. This may be seen more directly in Appendix A Figure 4 which directly plots the measured L_c vs diameter for each of the arteries examined, where we see that L_c increases with increase in cross section diameter.

While similar data have been published by previous researchers, in those cases, the IEL contour length was compared against the normalization done based either on the image itself [16], or on the zero-pressure diameter of the excised artery prior to fixation [11]. Svendson and Tindall

[16] quantified the corrugations by measuring length of the IEL in fixed arterial cross sections, and compared it to the in vivo luminal circumference. This in vivo circumference was calculated from the in vivo outer diameter measured for the exposed aorta of anesthetized rabbits. This study showed that the IEL circumferential length was 10-30% more than the approximated in vivo luminal circumference.

Figure1. 9 illustrates how a cross-section with IEL contour length = 10% larger than the circumference of the artery looks like. Figure1. 9 (A) shows a cross-section modelled in CAD with a corrugation factor = 1.1, comparing to the actual confocal image for one of the cross-sections with C_f = 1.1 (Figure1. 9 (B)). Qualitatively, we see that in the confocal image, The IEL corrugations look flattened out even though the IEL contour length given by the calculations is 10% more than the artery circumference. However, there are a few things that need to be considered. Firstly, the arterial cross sections are not exactly circular when fixed – meaning that there is a variation in local curvatures. As can be seen in the zoomed in sections of the IEL, the IEL is not entirely flat but has a fine variation which changes with the local curvature. Thus, at places where the local curvature is smaller, the corrugations are more prominent than those with a larger local curvature. Our measure of corrugations (C_f) is the average value of IEL contour length: circumference ratio, averaged over the entire cross-section. Hence there are portions of the cross-section, where this ratio is locally higher or lower than the calculated C_f. Secondly, the scale of the corrugations in the model (Figure1. 9 (A)) is much larger than that of the artery (Figure1. 9 (B)) is, which enables them to be more visible in a zoomed-out image of the model. When the images are converted to binary, these minute variations are taken into consideration during calculating the corrugation factor.

We observed that the diameter at which the corrugations flatten is larger than the diameter measured by ultrasound, supporting the presence of a corrugated luminal surface at the in vivo diameter. However, the surface contour length at this diameter was ~10% larger than the circumference of the artery which suggests that the corrugations are not very prominent at the ultrasound diameter. To determine if the luminal corrugations are significant at physiological diameters, we need to verify whether the diameter observed in ultrasound truly represents the physiological in vivo diameter of the artery. In the above mentioned study by Svendson and Tindall, the anesthetized artery diameters were found to be around 30% larger than the diameters of the fixed arterial cross-sections [16]. It has been well demonstrated that vasodilation occurs during anesthesia [30-35]. Thus, the arterial diameters measured by ultrasound in our study are larger than the physiological diameter in non-anesthetized animals. Smaller arterial diameter corresponds to a larger C_f and hence more prominent corrugations in the IEL topography. Hence, at physiological diameters, the IEL would be more corrugated than that at the larger diameters we observed in this study.

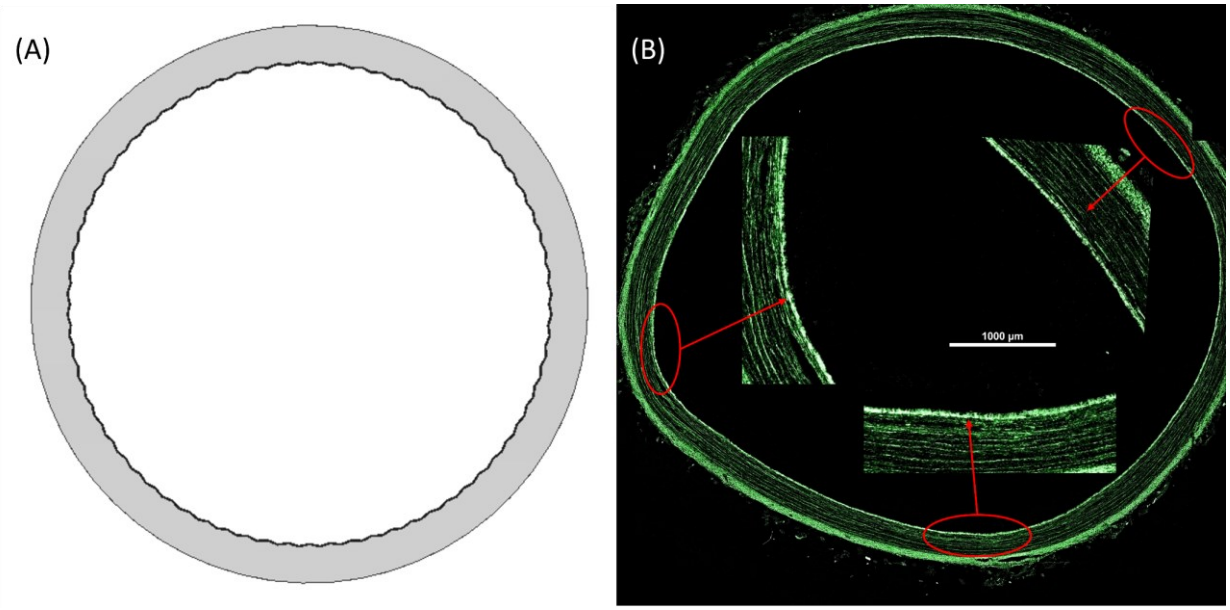

Figure1. 9 IEL topography for C_f ~ 1.1

(A) CAD model showing how the topography looks at C_f = 1.1, and (B) 723 LC, cross-section #5 (C_f = 1.11)

When there exist ridges on the inner lumen of a tubular conduit, these ridges flatten as the diameter of the conduit increases. Thus, in a pulsatile flow, these ridges provide a dynamic surface topography which could play an important role in reducing platelet adhesion and as a self-cleaning mechanism [36, 37]. Inspired by this principle, we looked at fabricating tubular conduits with surface topography. This study is shown in Section 1.01(a)(i)Appendix B and was conducted primarily as a fabrication methods study to create tubes with internal or external topography. These tubes have different potential applications including vascular replacements, and more details are given in Section 1.01(a)(i)Appendix B.

1.5 Conclusion

To summarize, we have examined the anatomy of arterial corrugations using optical microscopy of pig carotid arteries. Histological sections of arteries generally show that the luminal surface is strongly-corrugated. This is most evident from the tortuous and wavy appearance of the internal elastic lamina (IEL) that defines the boundary of the lumen. Yet, arteries are known to constrict upon excision from the body and also shrink during fixation, and hence these corrugations are sometimes believed to be an artifact of specimen fixation. Indeed, research on arteries fixed in an inflated state shows that the corrugations reduce as they are inflated. The central question underlying this research is whether the luminal surface of arteries is smooth or corrugated under physiological conditions.

The methodology followed in this article makes two main advances over previous research on arterial topography. First, we measure the diameter the carotid arteries using ultrasound while the animal is under anesthesia prior to excising the arteries. Second, we develop an innovative method of inflating each artery against the inside of a conical surface so that the exact same artery can be fixed simultaneously at many different diameters. Taken together, these innovations greatly reduce the uncertainty about the exact value of the physiological diameter, and also quantify the dependence of topography on diameter without the ambiguities caused by sample-to-sample variability.

Two central results appear from the quantification. First, the contour length of the IEL is roughly 10% longer than the arterial circumference from the ultrasound images. This indicates that under anesthesia when the ultrasound measurements were taken, the IEL is not entirely smooth. In fact, the physiological diameter is likely to be even smaller than the ultrasound diameter since anesthesia generally induces vasodilation. Thus, our results suggest that the arteries are corrugated

under physiological conditions. Second, we find that as the IEL corrugations flatten grow with increasing diameter, the IEL contour length does not remain fixed, but instead increases approximately as (diameter)$^{0.5}$. Thus, even though the IEL has a high stiffness as compared to the surrounding tissue, it does not appear to behave like an inextensible membrane.

Part 2

Design of Crimped Fiber Composites

Overview

The arterial wall consists of a number of different elements, among which the collagen fibers, elastin and smooth muscle cells dictate the mechanical response of the arteries. These elements together allow the arteries to distend, and also provide them with strain-hardening properties wherein the arterial wall stiffness increases as the arterial tissue stretches. These properties can be thus given to vascular prosthesis in order to make their mechanical behavior closer to that of biological arterial tissue. Such a behavior is observed not only in arterial tissue but in other biological soft tissues such as skin, bladder walls, etc. as well. The goal of Part 2 is to develop soft composites which seek to mimic the strain hardening behavior of tissues.

Combining more than one material to make a composite can lead to newer mechanical properties of the composite material. As mentioned above, tissues in our body consist of multiple different components which impart different properties to their mechanical behavior. Thus, different composites can achieve different behaviors depending on the constituents used. Short fiber composites are one such type where the behavior of the composite can be altered simply by varying the mechanical and geometric properties of two components: a softer matrix and short stiff fibers. In Part 2 of this dissertation, we present studies wherein such a strain hardening behavior can be replicated in a composite comprising a soft matrix with short stiffer crimped fibers embedded in it. Here we explore the parameters that come into play when designing such a material and the effect of those parameters on the mechanical behavior.

To control the mechanical response of the composite, it is necessary to understand how each component affects the composite properties. Thus, the first step is to understand how these crimped fibers affect the mechanical response of the composite. We therefore examine the mechanics of stress transfer for a single finite-length crimped fiber embedded in a soft matrix in

Chapter 2. This study was published as a paper J. Biomechanics and Modelling in Mechanobiology [38].

With a fundamental understanding of how a single crimped fiber affects the mechanical properties of short crimped fiber composites, we can now investigate what happens when there are multiple such fibers dispersed in a soft matrix to some target volume fraction. In Chapter 3, we explore additional parameters such as fiber volume fraction and fiber orientation, and the dependence of the mechanical behavior of the composite on these parameters. We also compare how the Equivalent Straight Fiber model for a single fiber (proposed in Chapter 2) predicts the behavior of multifiber composites. Multifiber composites are also fabricated in this study and the computational results are verified in this section.

The logical flow of Part 2 is illustrated in the following schematic.

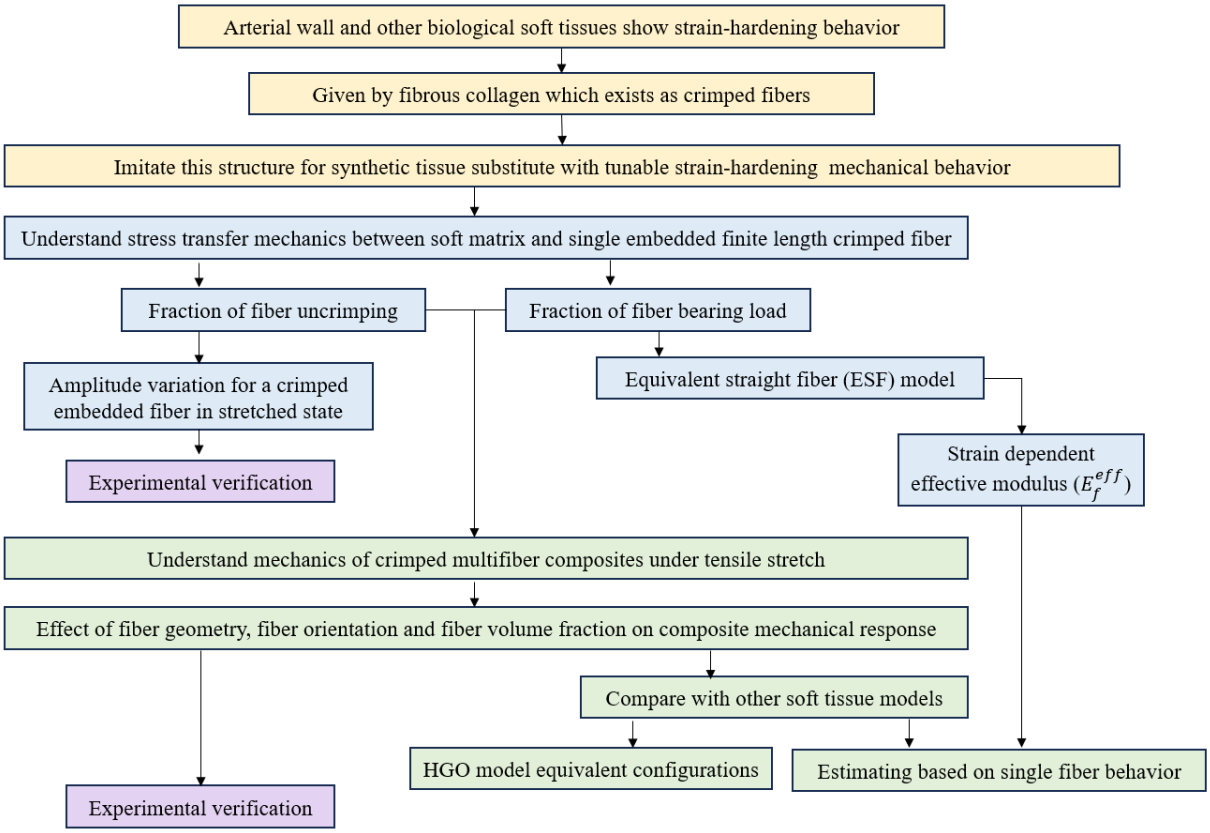

2.0 Mechanics of a Single Finite-Length Crimped Fiber Embedded in a Soft Matrix

2.1 Introduction

In a stress-free state, fibrous collagen in the body is organized with a periodic crimp pattern [39, 40]. This structure is observed in numerous tissues such as blood vessels, valve leaflets, intestine, ligaments, and tendons [39-41]. The crimped nature of collagen affects the mechanical and load-bearing properties of these tissues [39, 40, 42-45]. The crimp pattern allows for highly nonlinear behavior wherein tissues act as soft materials at low strains as fibers uncrimp without bearing much load, but as stiffer materials at higher strains as fully uncrimped fibers become increasingly load-bearing [39-44, 46, 47]. This phenomenon is well studied, and there have been numerous studies of collagen structure and its contribution to the mechanics of tissues [46-49].

In computational studies, soft tissues are often modelled as composites comprising of stiffer fibers embedded in a softer hyperelastic matrix, and their behavior has been modelled using finite element method for various types of fiber arrangements [50-57]. The fibers in these studies are treated as having periodic crimps defined by either helical [58] or planar sinusoid [50, 52, 57] geometry. Boundary conditions are prescribed such that they undergo tensile loading within the simulations [51, 55]. Such computational studies have helped develop an understanding of the mechanisms responsible for the experimentally observed non-linear elastic response of these tissues in response to externally applied loads [59-64].

Devices intended for implantation within the body have sought to replicate the mechanical behavior of collagen containing tissues, for example, using wavy knitted patterns as a graft

material [61, 62] to manufacture long continuous crimped fibers for applications such as vascular conduits [59-65]. Other approaches aiming to replicate these behaviors include electrospinning crimped fibers onto graft surfaces [59, 63, 64]; using multilayer collagen fiber reinforced tissue engineered composites [60]; suturable scaffolds [65, 66], stents [67], and bladder matrix[68]. However, a common limitation of these approaches is that it is difficult to process these materials into arbitrary shapes [69, 70]. Indeed, this problem is not unique to crimped fibers – all continuous fiber composites are difficult to fabricate into arbitrary shapes, though there has been more recent progress in this direction [71]. Outside of the biomedical area, it has long been common to use chopped fiber composites (sometimes also called short fiber composites) to overcome the processability limitations of continuous fiber composites. Such composites are typically based on glass or carbon fibers cut to several-mm lengths and dispersed within a polymer matrix. Also, conceptually related are nanocomposites which comprise stiff nanoscale fillers of high aspect ratio such as carbon nanotubes, cellulose whiskers, or clay platelets dispersed into plastics [72-74]. Since the reinforcing fillers are no longer continuous, such chopped fiber composites or nanocomposites can be processed via conventional plastics processing operations including extrusion, molding, and extrusion-based 3D printing [57, 75-80]. However, since the fillers are not in a crimped form, such composites do not replicate the strain-hardening behavior of collagen containing tissues. The eventual goal of this research is to develop synthetic tissue substitutes where crimped fibers of a finite length act as reinforcing agents for a softer matrix. Such short fiber composites with crimped fibers may mimic the strain hardening behavior of collagen-rich tissues. Their mechanical properties may be tuned by changing the properties of the fibers such as the modulus, orientation, crimp geometry, and volume fraction of fibers [81-83]. Most

importantly, similar to other chopped fiber composites, they would be processible, e.g. by molding or extrusion, thus facilitating manufacture of arbitrary shapes [77, 80, 84].

This chapter is the first step in understanding the mechanics of short fiber reinforced composites where we quantify the contribution of a single fiber to the properties of the composite. As reviewed in 2.2, such a single-fiber analysis has provided enormous insights into how a fiber's length and mechanical properties affect the modulus of the composite for non-crimped fibers. Thus, this study aims to take the same approach for crimped fiber composites by considering a single crimped fiber embedded in a sufficiently large soft matrix and examining the mechanics of uncrimping as the surrounding matrix is stretched.

2.2 Shear Lag Model for Straight Fiber Composites

When a composite composed of straight fibers embedded in a softer matrix is placed under tensile stress, there occurs a transfer of stress from the matrix to the fiber thread [85]. A commonly-used model for this stress transfer is based on the shear lag theory [85, 86], first developed by Cox (1952) to model the behavior of discontinuous fiber composites when all of the fibers are aligned along the tensile direction. This theory assumes that each fiber (of length $2L$ and radius r_f) is located at the center of a cylindrical matrix such that the ratio of fiber volume to the cylinder volume matches the volume fraction ϕ of fibers in the composite. When the matrix is stretched along the x-direction (i.e. along the axis of the cylinder) to a strain of ε, the stress in the fiber rises from zero at the fiber ends as per

$$\sigma_f(x) = E_f \varepsilon \left[1 - cosh\left(\frac{n}{r_f}x\right).sech\left(n\frac{L}{r_f}\right)\right] \tag{2.1}$$

where x is the coordinate along the fiber direction such that the fiber spans $-L < x < L$. Note that σ_f/E_f is simply the strain ε_f in the fiber. The quantity n is

$$n = \left[\frac{2\,E_m}{E_f(1+\,\nu_m)\,ln\,\left(\frac{1}{\phi}\right)}\right]^{\frac{1}{2}} \tag{2.2}$$

where E_f and E_m are the moduli of the fiber and matrix, respectively and ν_m is the Poisson's ratio of the matrix. The quantity E_f/E_m will be called relative modulus henceforth. Exemplary profiles of $\varepsilon_f(x) = \sigma_f/E_f$ are shown as solid lines in **Error! Reference source not found.**(A) discussed l ater. Integration of Eq. 2.1 over the fiber length gives the mean stress in the fiber as

$$\bar{\sigma_f} = E_f \varepsilon \left(1\ - \frac{tanh\,(nL/r_f)}{nL/r_f}\right) \tag{2.3}$$

Since the fibers are taken as aligned along the loading direction, the stress of the composite can be obtained by a weighted average of the fiber and the matrix. The ratio of this composite stress to the applied strain ε gives the composite modulus:

$$E_{com} = \frac{\bar{\sigma_f}}{\varepsilon}\phi + E_m(1-\phi) \tag{2.4}$$

where the subscript *com* indicates composite.

It is also useful to define a dimensionless quantity $\varepsilon_f(x) = \frac{\sigma_f(x)}{E_f}$ which is a measure of the strain in the fiber so that Eq. 2.1 can be rewritten as

$$\varepsilon_f(x) = \frac{\sigma_f(x)}{E_f} = \varepsilon\left[1 - cosh\left(\frac{3x}{l_s}\right).sech\left(\frac{3L}{l_s}\right)\right] \tag{2.5}$$

where $l_s = 3r_f/n$ is defined as the shear lag length. The factor of 3 is generally included in the definition of l_s because for sufficiently long fibers, the quantity in the square brackets is nearly 1 everywhere except within a distance of l_s from the ends.

Eqs. 2.1-2.5 offer key insights on how the length of fibers affects the mechanics of chopped fiber composites. Two limits can be identified readily. In the long fiber limit, $\frac{L}{l_s} = \frac{nL}{3r_f} \gg 1$, Eq. 2.1 and 2.2 state that the entire length of the fiber except for the region within a distance l_s from the ends has $\sigma_f(x) \approx E_f\varepsilon$, or equivalently $\varepsilon_f(x) \approx \varepsilon$. Accordingly, most of the fiber is loaded to the highest extent possible at the applied strain, and hence Eq. 2.4 states that the composite modulus E_{com} is simply a volume-weighted average of the moduli of the fiber and the matrix. However, the fiber strain drops to zero over the length of roughly l_s adjacent to each end. Within this region, stress is transferred by shear from the matrix to the fiber. In the short fiber limit, when $\frac{L}{l_s} = \frac{nL}{3r_f}$ is on the order of 1 or smaller, Eq. 2.1 and 2.2 state that $\sigma_f(x) < E_f\varepsilon$, or $\varepsilon_f(x) < \varepsilon$. In this case, no portion of the fiber is fully-loaded, and the chopped fiber is a relatively ineffective reinforcing agent.

Although the mechanics of crimped fiber composites are expected to differ from that of straight fiber composites, two effects may be expected from the discussion above. First, we anticipate that because the fiber can accommodate stretching by uncrimping, the actual strain in the fiber will be lower than the strain in the matrix, i.e. unlike Eq. 8, $\varepsilon_f < \varepsilon$ is expected in the mid-section of a fiber even if the fiber is very long. Under these uncrimping conditions, the mid-section of the fiber contributes relatively little to the composite modulus because it bears only a low stress. Yet, as the fiber uncrimps, it will increasingly resemble a straight fiber, i.e. ε_f will approach ε as the strain increases, leading to the strain hardening that mimics collagen-bearing tissues. Second, even for crimped fibers, we anticipate a near-end section where the fiber experiences lower strain than the

central section. In this region, only partial uncrimping is expected, and hence this region will contribute less to strain hardening. The central goal of this article is to quantify these two effects as the crimp amplitude and the modulus of the fibers is varied.

With the above background, we can now formulate the questions to be addressed by simulations in this paper: (a) At what strain does the mid-section of a long fiber uncrimp, how does the uncrimping affect the load borne by the fiber, and how does the uncrimping tune the strain hardening behavior of the composite?, (b) Over what length near the fiber ends does the stress reduce significantly – which in turn defines the minimum length of crimped fiber necessary to achieve the desired strain hardening, and (c) How are the previous two questions affected by the fiber geometry and modulus of the fiber relative to the matrix?

2.3 Methods

We examined the mechanics of stress transfer of a crimped fiber embedded in a matrix using 3D finite element simulations. A single crimped fiber was embedded in a matrix of a relatively low Young's modulus and of dimensions $2L_m$ along the x-direction, $2H_m$ along the y direction, and W_m along the z-direction (Figure 2. 1 (A)). Taking advantage of symmetry, only half of the geometry was modelled. For straight fiber simulations, the fiber was specified as a hemicylinder of radius r_f and length $2L = 400\, r_f$ centered on the x-axis. The crimped fiber was modelled as a sequence of circular arcs, with the cross-section being hemicylindrical (Figure 2. 1 (B-C)). These arcs were defined by a parameter θ, the projected angle. The wavelength of the crimps was fixed $\lambda = 40\, r_f$ and thus a change in θ corresponded to a change in the initial

amplitude of the crimps (Figure 2. 1 (D)). The dimensions of the matrix were chosen to be $2L_m = 2000\ r_f, 2H_m = 2400\ r_f$ and $W_m = 400\ r_f$. Doubling the dimensions of the matrix did not change the results significantly, showing that these dimensions were sufficiently large for the matrix to be regarded as infinite in extent. The simulation geometry was modelled in Autodesk Inventor (2018) and meshed in the FeBio software [87].

The left face of the matrix (the plane $x = -L_m$) was held fixed while the right face ($x = L_m$) was displaced along the x-direction using a rigid body connection. The applied displacements corresponded to nominal strains (ratio of x-displacement to $2L_m$) of up to 0.69. Symmetry boundary conditions were imposed on the center plane (z=0), whereas the remaining surfaces ($y = \pm H_m$ and $z = W_m$) were kept stress-free. Neo-Hookean material was chosen both for the thread and the surrounding matrix. An adaptive tetrahedral mesh was used for the fiber and matrix. The mesh density was uniform across the fiber and the total number of elements increased with contour length of the fiber (i.e. with the amplitude), ranging from 21916 for straight fiber to 31620 for fiber with semicircular arcs. Facet-to-facet no-slip contact was applied between fiber and the matrix. Figure 2. 1 (E) shows a screenshot of the fiber mesh as seen at the central plane. The simulation results were found to be nearly identical when the mesh density was doubled, i.e. with 8-fold increase in the number of elements, showing that the mesh density was adequate to correctly resolve the mechanics.

Two sets of simulations were conducted. In the first, the modulus ratio was held fixed at 1000 and four values of θ (0°, 120°, 150° and 180 °) were examined. The corresponding ratios of peak-to-trough amplitude to the wavelength were 0, 0.29, 0.38 and 0.5. This set of simulations allowed a clear assessment of the strain-dependent uncrimping of fibers, and the comparison with a straight fiber. In the second set, the initial amplitude was held fixed at θ = 150°, while the modulus ratio

was varied. These simulations were also compared against simulations for a straight fiber geometry. The simulations also provided end reaction forces that had to be applied at the $x = \pm L_m$ boundaries to maintain the specified displacement. These forces allowed calculation of the contribution of the embedded fiber to the stiffness of the composite as described in the Appendix.

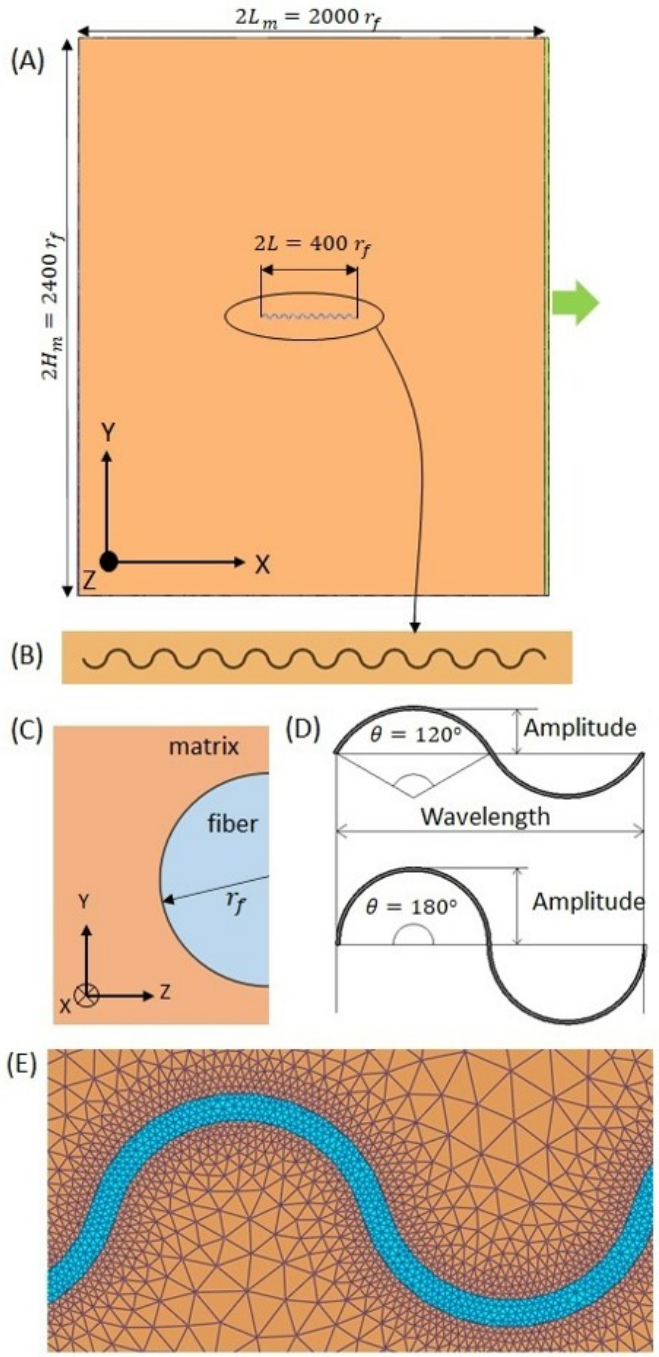

Figure 2. 1 Geometry of single fiber simulations

(A) Relative dimensions of the matrix and embedded fiber (B) Magnified view of the geometry of the fiber, (C) Semi-circular cross section of the hemicylindrical fiber, (D) Examples of how θ affects the initial amplitude of the fiber, (E) Tetrahedral adaptive mesh near the fiber-matrix interface illustrated for the fiber with $\theta = 150°$

2.4 Results

2.4.1 Stress Evolution of Uncrimped Vs Crimped Fiber

To illustrate the effect of crimps on the stretching behavior, Figure 2. 2 compares two cases: $\theta = 0°$ (straight fiber) vs $\theta = 150°$, both at a relative modulus value of 1000. In both cases, we plot the stress profile in the fiber normalized by its modulus (σ_f/E_f) at four values of applied strain (ε =0.15, 0.33, 0.51 and 0.69) which are indicated by the horizontal dotted lines in Figure 2. 2 (A). Here, σ_f refers to the σ_{xx} component of the in-fiber Cauchy stress tensor. These values are. Consistent with Section 2.2, the quantity σ_f/E_f is defined as ε_f henceforth. Figure 2. 2 (A) shows that the profiles of ε_f in the straight fiber are in reasonable agreement with those predicted by the shear lag model Eq. 2.1 with no fitting parameters. The L/l_s calculated using Eq. 2.5 is 1.2, thus showing that the half-length of the fiber only slightly exceeds the shear lag length. Accordingly, Eq. 2.5 predicts, and simulations confirm, that the $\varepsilon_f(x)$ in the mid-section of the fiber is nearly constant and nearly equal to the applied strain, whereas it reduces to zero over a distance of roughly l_s from the ends.

Figure 2. 2 (B) shows the $\varepsilon_f(x)$ profiles for an embedded crimped fiber with $\theta = 150°$. Although modulated by the crimp wavelength, the gross distribution of ε_f qualitatively resembles that in Figure 2. 2 (A): the mid-section of the fiber has a nearly uniform value of ε_f, which reduces to zero near the ends. The major quantitative difference however is that the magnitude of ε_f near the middle is much lower than the applied strain because, as explained the end of Section 2, the applied strain is accommodated by uncrimping. A second, more subtle difference is that with increasing strain, the uniformly-loaded mid-section shrinks. Equivalently, there is an increase in the length

near the ends where stress is lower than in the mid-section. The solid lines in Figure 2. 2 (B) are discussed later in Section 2.5.1, along with Eq. 2.5.

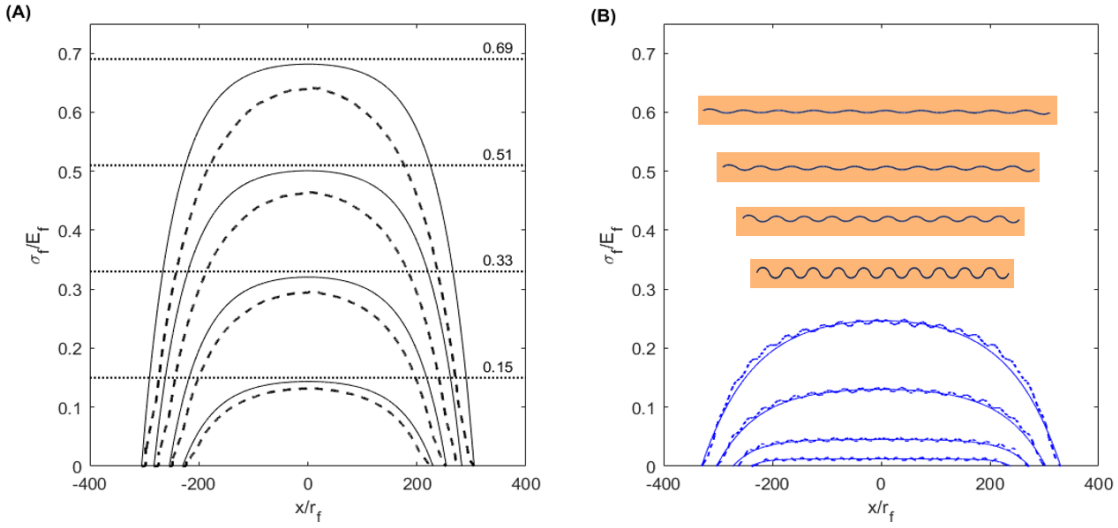

Figure 2. 2 Stress evolution of uncrimped vs crimped fiber

(A) Distribution of $\varepsilon_f = \sigma_f/E_f$ for straight fiber: simulation data (black dashed line), Eq. 5 (black solid line), and (B): σ_f/E_f, where σ_f is the x-component of the Cauchy stress in the fiber; for crimped fiber with θ =150°: simulation data (blue dashed line), Eq. 9 (blue solid line, discussed in section 5.1). In both graphs, the data are shown at applied strain values (going from top to bottom) of 0.69, 0.51, 0.33, 0.15. These four values are shown as horizontal dotted black lines in A. The images in B are screenshots of the fiber at the same four strains to illustrate uncrimping.

2.4.2 Effect of Initial Amplitude

We will now quantify the uncrimping behavior by comparing fibers of various initial amplitudes (i.e. various θ values), all at a relative modulus of 1000. Figure 2. 3 shows the spatial distributions $\varepsilon_f(x)$ of the various fibers, all at an applied stretch of 0.69. Snapshots of the fiber shape before and after stretching to an applied strain of 0.69 are shown in Figure 2. 4.

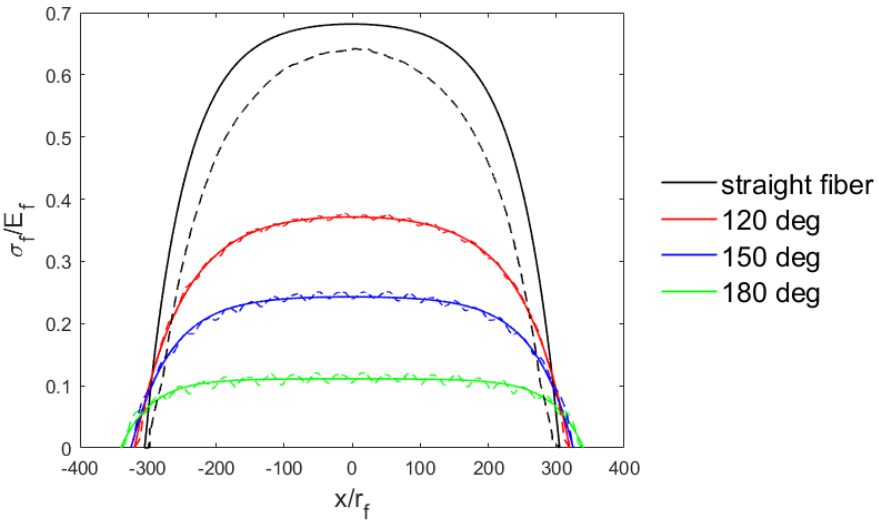

Figure 2. 3 Normalized stress in fiber: effect of crimp amplitude

Non-dimensional stress $\varepsilon_f(x) = \sigma_f(x)/E_f$ for different initial crimp amplitudes given by θ = 0° (straight fiber), 120°, 150° and 180°; for E_f/E_m = 1000 and applied strain = 69% (dashed lines), and Eq. 9 (solid lines, discussed in section 5.1)

As in Figure 2. 2 (B), in all cases, the mid-section of the fiber has an approximately flat distribution of ε_f. Further the mid-section also has a nearly uniform crimp amplitude (upper portion of **Error! Reference source not found.**). Both these observations suggest that the mid-sections of the fibers are isolated from any effects of shear lag from the fiber ends. Therefore, the mechanics of uncrimping – independent of end effects – can be quantified by examining a narrow section of the fiber near the middle. For this, we selected a two-wavelength-wide region at the center and calculated two quantities: the peak-to-trough amplitude which quantifies the geometric aspects of uncrimping, and the mean value of $\langle\varepsilon_f\rangle = \langle\sigma_f\rangle/E_f$ which quantifies the strain borne by the fiber.

Figure 2. 4 (A) shows that for the straight fiber, the mean value of $\langle\varepsilon_f\rangle$ is only slightly smaller than applied strain ε and increases almost linearly with ε. The slight nonlinearity is a geometric effect of the fiber length increasing as strain increases. For all the crimped fibers, $\langle\varepsilon_f\rangle < \varepsilon$ at small applied strain, and then grows non-linearly in a manner similar to collagen recruitment.

Concurrently, the amplitude reduces rapidly at low strain before levelling off as the fibers straighten. In effect, since the fiber straightens at small applied strain, further stretching must be accommodated by fiber stretching, rather than uncrimping. As discussed in Section 1, this increase in $\langle \varepsilon_f \rangle$ (and hence $\langle \sigma_f \rangle$) relates to strain hardening, and will be quantified later in this paper. As expected, all three quantities ($\varepsilon - \langle \varepsilon_f \rangle$), the ε value at which $\langle \varepsilon_f \rangle$ increases rapidly, and the ε value at which the amplitude significantly reduces all increase with θ. All three trends indicate an increasing degree of uncrimping with increasing initial crimp amplitude.

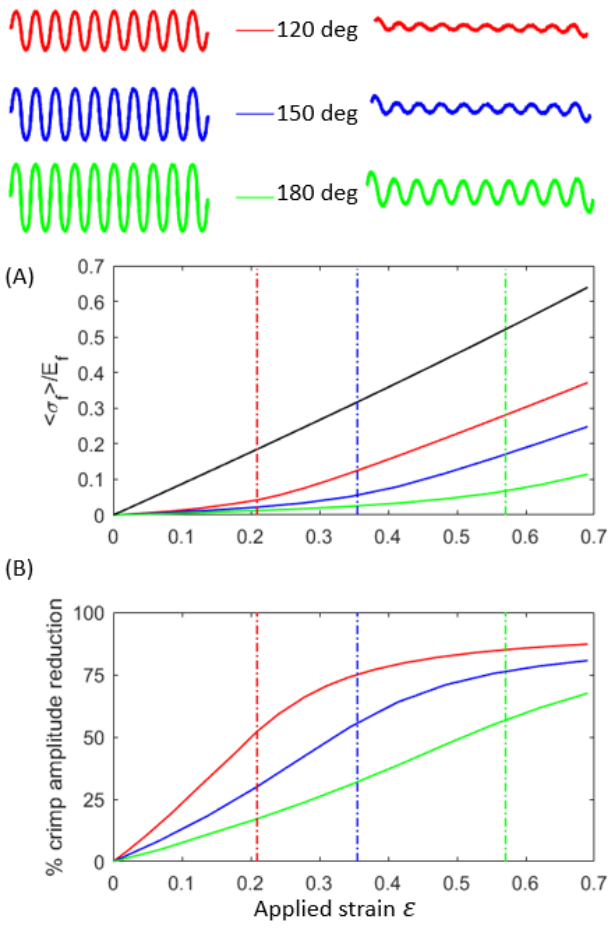

Figure 2. 4 Reduction in amplitude: effect of crimp amplitude

Upper images show amplitude profiles at applied strain ε= 0 (top left) and ε =0.69 (top right). (A) Mean value $\langle \varepsilon_f \rangle$ averaged over two wavelengths near the center, and (B) percent decrease in crimp amplitude in the mid

portion of the fiber for E_f = 1000. Vertical lines correspond to the strains needed for geometric straightening (see text).

The vertical lines in Figure 2. 4 correspond to "geometric straightening", and are calculated as the strain needed to make the end-to-end length of the uncrimped fibers equal to the fiber contour length of the original crimped fiber. Figure 2. 4 (B) shows that at a strain corresponding to geometric straightening, the amplitude has only reduced by about 55-60% of the original value, i.e. a significant portion of the straightening continues beyond this point.

Finally, the amplitude profiles at the top of Figure 2. 4 show that the crimp amplitude does not decrease as much near the ends. This is not surprising: it is the tensile stress that induces straightening, and the end-region has a much lower tensile stress. Since the amplitude change is modest, one may expect that this end region would make only a small contribution to strain hardening.

2.4.3 Effect of Relative Modulus

The effect of relative modulus was examined by comparing fibers with three values of (E_f/E_m) = 10, 100 and 1000. The angle was held fixed at θ = 150°. Qualitatively, all three values of relative modulus show similar behavior, and in all cases, the mid-section of the crimped fiber has a plateau in ε_f. Quantitatively, two effects are readily apparent. First, with decreasing relative modulus, the ε_f increases (Figure 2. 5) indicating that fibers of lower stiffness accommodate the applied strain by stretching rather than uncrimping. Second, as fiber modulus reduces, the mid-section where the fiber has nearly-constant ε_f becomes wider (equivalently, the near-end region of the fiber which bears a lower stress becomes shorter).

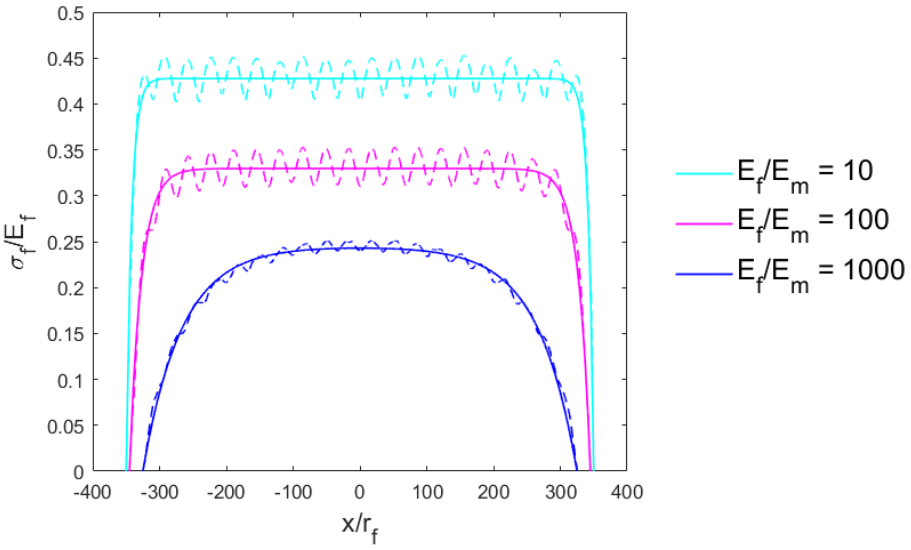

Figure 2. 5 Normalized stress in fiber: effect of relative modulus

Non-dimensional stress $\varepsilon_f(x) = \sigma_f(x)/E_f$ for E_f = 10, 100 and 1000, and θ = 150°

Analogous to Figure 2. 5, Figure 2. 6 (A) shows the evolution of the average value $\langle \varepsilon_f \rangle$ over two-wavelengths at the center of the fiber, whereas Figure 2. 6 (B) shows the % decrease in crimp amplitude in the mid-section. The crimp amplitude decreases much less with decreasing relative modulus: for a relative modulus of 1000, the amplitude reduces by 82% of the original value, whereas for a relative modulus of 10, the decrease is only 21%. Similar to Figure 2. 4, beyond the strain for geometric straightening (vertical line), the decrease in amplitude with strain continues, but becomes more gradual (Figure 2. 6 (B)).

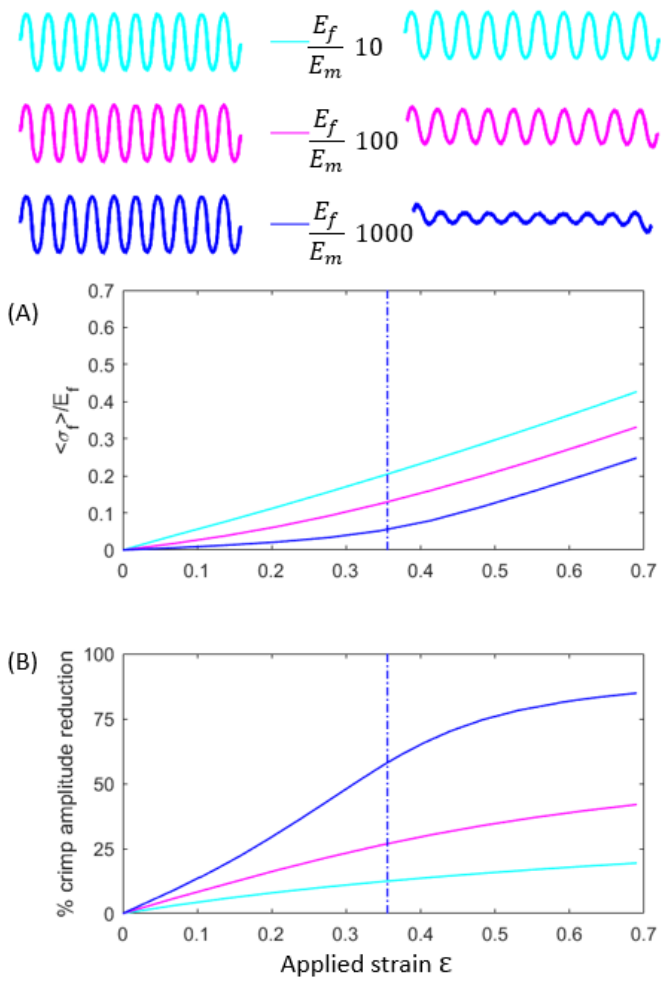

Figure 2. 6 Reduction in amplitude: effect of relative modulus

Upper images show amplitude profiles at applied strain ε= 0 (top left) and ε=0.69 (top right). Note that the end-to-end length for profiles on the right are 69% longer than those on the left. (A) Mean value $\langle \varepsilon_f \rangle$ averaged over two wavelengths near the center, and (B) percent decrease in crimp amplitude in the mid section of the fiber for θ = 150°

2.5 Discussion

The simulations show that at any given value of applied strain, the mid-section of the crimped fiber bears a lower stress than a straight fiber of the same aspect ratio and modulus. Further, similar to

a straight fiber, the crimped fiber has a near-end region that is loaded less than the mid-section. The ultimate goal of these simulations is to inform the design of composites that use chopped crimped fibers to achieve strain-hardening behavior that mimics collagen-rich tissues. In this Discussion section, we do so in two steps: Section 2.5.1 proposes that the crimped fiber may be treated as an equivalent straight fiber. Section 2.5.2 then uses the equivalent straight fiber concept to estimate the modulus of composites comprising crimped fibers embedded in a soft matrix.

2.5.1 Equivalent Straight Fiber (ESF) Model

As discussed above, Figure 2. 2, Figure 2. 3 and Figure 2. 5 show that the gross shape of $\varepsilon_f(x)$ profile resembles that of straight fibers, albeit with a wavelength-scale modulation. This suggests that we may regard the crimped fiber as an equivalent straight fiber which has the same end-to-end length as the crimped fiber, but a different effective radius, shear lag length, and stiffness. Accordingly, the stress in the crimped fiber may be postulated to follow Eq. 2.1, but in modified form

$$\sigma_f(x) = E_f^{eff}\varepsilon\left[1 - cosh\left(\frac{n^{eff}}{r_f^{eff}}x\right).sech\left(n^{eff}\frac{L}{r_f^{eff}}\right)\right] \tag{2.6}$$

where n^{eff} is defined identically as Eq. 2.2, but with E_f replaced with E_f^{eff}. Here $E_f^{eff} < E_f$ is the modulus of the equivalent straight fiber. For a sufficiently long crimped fiber, Eq. 2.5 has a flat profile near its middle, however, unlike the for a straight fiber, the magnitude of the stress far from the ends is $E_f^{eff}\varepsilon$. The ratio E_f^{eff}/E_f may be regarded as a fiber efficiency factor, and we anticipate that its value increases with applied strain as the fiber uncrimps and approaches a straight

fiber. Further the stress decays towards zero within an effective shear lag distance $l_s^{eff} = 3r_f^{eff}/n^{eff}$. Eq. 2.5 was fitted to the strain profiles using E_f^{eff} and r_f^{eff} as the fitting parameters, and the solid lines in Figure 2. 2 (B), Figure 2. 3 and Figure 2. 5 show that reasonable fits are obtained. The corresponding fitting parameters, and the calculated values of l_s^{eff}, all suitably non-dimensionalized, are shown in Figure 2. 7 (A-C) at fixed modulus ratio, and (E-G) for fixed amplitude. The shear lag length for fiber with large amplitude ($\theta = 180$) and modulus ratio of 1000 is smaller than half of the crimp wavelength for $\varepsilon < 0.15$, making the fits unreliable for small strains for this fiber, and hence are not reported in Figure 2. 7.

The results of Figure 2. 7 can now guide the design of composites based on chopped crimped fibers. Figure 2. 7 (A and E) quantify the degree to which sufficiently long crimped fibers can act as strain-hardening reinforcers. Specifically, Figure 2. 7 (A) shows that at a relative modulus of 1000, crimped fibers have $\frac{E_f^{eff}}{E_f} < 0.1$ at small strain, i.e. they have an effective modulus that is over 10-fold lower than their actual modulus. Equivalently, the stress in the fiber is less than 10% of the value expected for a long straight fiber. With increasing strain, their effective modulus increases analogous to collagen recruitment, and further, fibers with larger initial crimp amplitudes require larger strains to be recruited. Indeed, at the highest amplitude corresponding to $\theta = 180°$, $\frac{E_f^{eff}}{E_f}$ remains below 0.1 up to an applied strain of nearly 0.52, indicating that the fibers are approximately inextensible. i.e. they uncrimp with very little stretching. An unexpected result from Figure 2. 7 (E) is that for fibers with a modulus ratio of 10, E_f^{eff} is nearly independent of ε suggesting that these fibers are altogether ineffective at realizing strain hardening, i.e. crimped

fibers with the geometry used here can only confer significant strain hardening if their modulus is at least 100-fold larger than of the matrix.

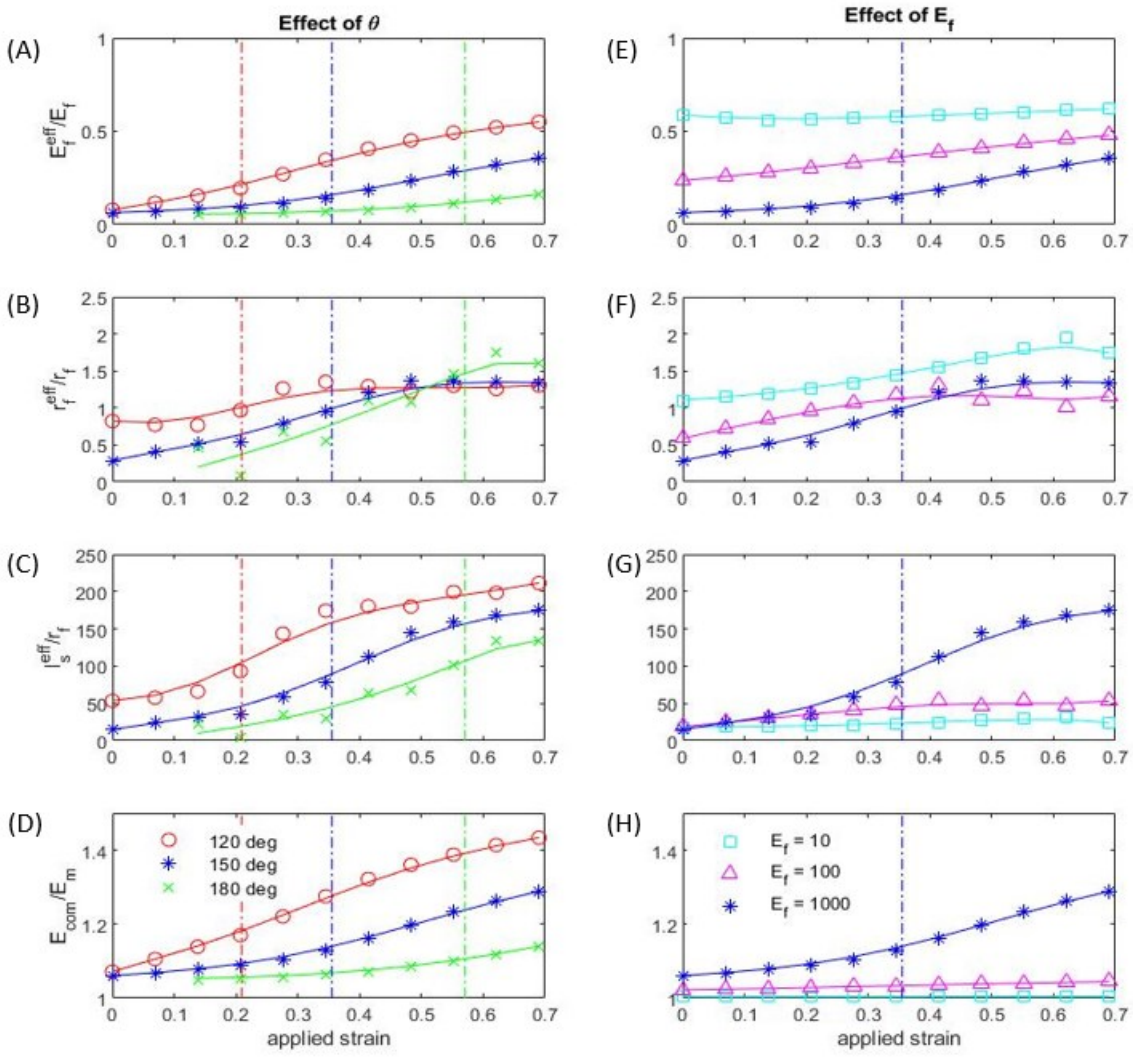

Figure 2. 7 ESF results for single fiber simulations

Variation in (A&E) equivalent effective modulus factor E_f^{eff}/E_f), (B&F) normalized effective radius (r_f^{eff}/r_f), (C&G) normalized effective shear lag length (l_s^{eff}/r_f) and (D&H) normalized modulus of the composite (E_{com}/E_m) with applied strain using $\phi = 1 \times 10^{-3}$. Left column shows effect of varying crimp amplitude at fixed relative modulus of 1000. Right column shows effect of relative modulus at fixed crimp

amplitude corresponding to θ = 150°. Vertical lines indicate the strains for geometric straightening of the crimps.

Figure 2. 7 (A and E) only comment on the uncrimping behavior of sufficiently-long fibers since the value of E_f^{eff} only determines stress in the fiber far from the ends. To understand fiber length effects, we turn to . Figure 2. 7 (C and G) which plots the strain-evolution of the effective shear lag length l_s^{eff}. As discussed above, a straight fiber with $L < l_s$ cannot be loaded to its fullest extent and hence may be regarded as an ineffective reinforcing agent. Analogously, for a crimped fiber if $L < l_s^{eff}$, the mid-section of the fiber bears a stress even lower than $E_f^{eff}\varepsilon$. Such a fiber will uncrimp less than a long fiber, and be unsuitable to realize strain-hardening behavior. Figure 2. 7 (C) shows that for a relative modulus of 1000, l_s^{eff} is comparable to the wavelength at small strain, but increases significantly with strain, i.e. a fiber that is long enough to approximate infinite-length at small strain may have more significant end-effects at large strain.

2.5.2 Modulus of Composites

The modulus of such composites can be estimated from adding the matrix and the fiber contributions as per Eq. 2.4. We now take advantage of the equivalent fiber concept and hence integrate Eq. 2.5 over the fiber length to estimate the mean stress in the fiber, $\bar{\sigma}_f$. The final expression for $\bar{\sigma}_f$ is identical to Eq. 2.3, but with effective quantities on the right hand side. Appendix A shows that an independent method of estimating $\bar{\sigma}_f$ using end-reaction forces is in excellent agreement with the equivalent fiber approach. The values of E_{com} thus calculated from Eq. 2.4 are plotted in Figure 2. 7 (D and H). They show how the desired level of strain hardening can be achieved by an appropriate choice of initial amplitude and relative modulus of the fibers.

For small strains, all the composites (but especially those with crimped fibers of high initial amplitude) have a modulus that is only slightly higher than of the matrix. At high relative modulus, the fibers make increasing contributions to modulus as strain increases, analogous to collagen recruitment. The strain for onset of strain hardening approximately matches the geometric limit of the strain needed to completely uncrimp the fibers. As mentioned above, the degree of strain hardening is very modest for modulus ratios of 100 and 10 (Figure 2. 7 (H)), i.e. for the geometry considered here, crimped fibers would be useful for strain hardening only if the relative modulus is on the order of 1000 or higher.

The limitations of Eq. 2.4 must be noted: it is only justifiable if the fibers are aligned along the tensile direction and dilute (and hence their stress fields are non-interacting). In our calculations, we have used a volume fraction (ϕ) of 1×10^{-3} for the fiber in the simulated matrix as representative of dilute conditions. A more detailed computational study would be needed to identify the volume fraction at which fibers interact with each other, and to estimate the modulus of the crimped fiber composites with a high volume fraction of fibers.

2.5.3 Fiber Contribution to Reinforcement

As illustrated in Fig. 1 in the main text, the simulation outputs the tensile force F that must be applied on the boundary at $x = L_m$ to achieve the desired strain. Simulations were also conducted without a fiber to obtain the force F_m when the matrix alone is stretched. We may now define β as

$$\beta = \frac{F - F_m}{F_m} \tag{2.7}$$

β represents the fractional extra force needed to stretch the matrix due to the presence of the fiber.

The quantity β may be compared against the force-contribution of the fiber calculated using the effective fiber approach described in the main text. The quantity $\frac{\overline{\sigma_f}}{E_m\,\varepsilon}$ defined in Section 2.4.1, as the ratio of average stress in the fiber to that in the matrix, is obtained from simulation data. The contribution of the single fiber is then estimated by integrating the stress profile over the entire fiber to obtain

$$\alpha = \frac{\bar{\sigma}_f}{E_m\,\varepsilon}.\phi = \frac{E_f^{eff}}{E_m}\left(1 - \frac{tanh\left(n^{eff}L/r_f^{eff}\right)}{n^{eff}L/r_f^{eff}}\right)\phi \tag{2.8}$$

where ϕ is the volume fraction of the fiber in the matrix. α represents the ratio of average stress in fiber to average stress in the matrix, when experiencing the same strain, scaled to the volume fraction of the thread.

The contribution of the fiber to the composite stiffness obtained in these two distinct ways – β using the total force, and α using the average of the stress distribution – are compared in Figure 2. 8 for the same simulations as Figure 2. 3 and Figure 2. 4. Figure 2. 8 also includes a theoretical value of α for a straight fiber from the shear lag model (dashed). This is obtained from averaging Eq. 2.3 in the main text over the length of the straight fiber

$$\alpha^{straight} = \frac{E_f}{E_m}\left(1 - \frac{tanh\,(nL/r)}{nL/r}\right)\phi \tag{2.9}$$

For the straight fiber, α and β start at a higher value and remain nearly constant. The slight increase in the quantities is due to in increase in the fiber length as strain increases. For the crimped fibers, α and β, start at low values and increase non-linearly with strain, indicating increasing contribution as the fiber uncrimps. The good agreement between the two methods establishes that Eq. 2.8 can be used to accurately obtain the contribution of the crimped fiber to the composite once the quantities E_f^{eff} and r_f^{eff} are found for the equivalent fibers.

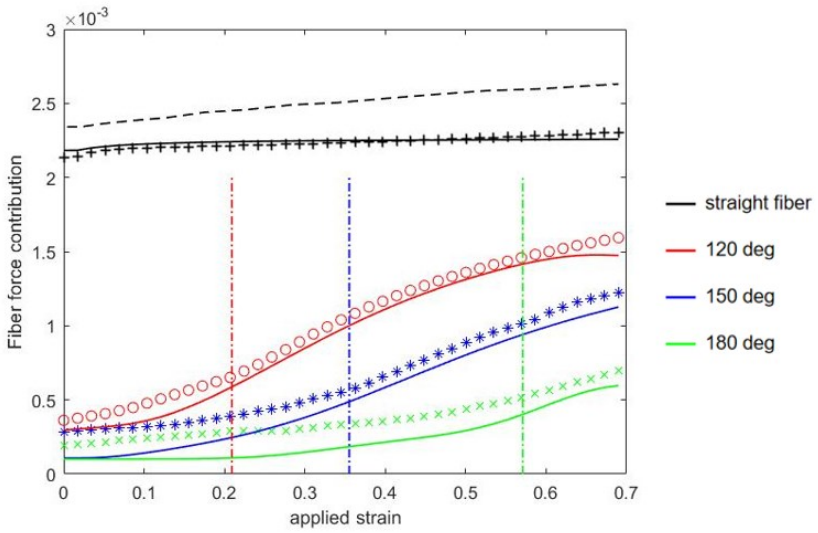

Figure 2. 8 Fiber force contribution

Comparison of two different methods of calculating the contribution of single fibers to the force in the composite. Stars show the value of β calculated from the end-reaction forces (Eq. A1). Solid lines are calculations of α from the equivalent fiber model (Eq. A2). Dashed black line is the prediction of shear lag model (Eq. A3) with no fitting parameters.

2.6 Summary and Conclusion

The crimped structure of collagen fibers is well-recognized as contributing to the strain hardening behavior of tissues. We consider the mechanics of composites composed of chopped crimped fibers embedded in a softer matrix. Such discontinuous fiber composites have the potential to show strain hardening behavior while also being flow-processible. This paper examines the behavior of a single crimped fiber of a specified length as the matrix embedding the fiber is stretched. Simulations show that such a crimped fiber bears lower load than a straight fiber of the same modulus, but that the load borne by the fiber increases non-linearly as the matrix strain increases. Concurrently, the fiber is found to straighten (i.e. the crimp amplitude reduces) analogous to collagen recruitment.

As with traditional chopped-fiber (also known as short-fiber) composites, there are significant end-effects. There is a certain length near the ends of the crimped fiber where the stress is significantly lower than the stress in its mid-section, analogous to the shear lag length in straight fiber composites. Consequently, the fiber does not uncrimp in this less-loaded region near the ends. This can be verified experimentally as well. A more detailed study of the amplitude variation along the fiber and experimental verification is presented in Section 1.01(a)(i)Appendix C. Thus, crimped fibers can significantly contribute to the modulus of the composite (and hence to the strain hardening behavior of the composite) only if the fiber is much longer than this shear lag length. This can also be seen by looking at the crimp amplitude along the fiber.

Broadly, the stress profiles in crimped fibers resemble those in straight fiber composites, and hence we develop the concept of an equivalent fiber. Accordingly, a crimped fiber can be treated as an equivalent straight fiber, but with an effective modulus and effective radius that is different from

its true modulus and radius. This allows prediction of the contribution of the fiber to the modulus of the composite.

We quantify how all the relevant quantities: the load bearing capability of the fiber, the shear lag length, and the modulus of the composite, depend on the crimp amplitude and the modulus of the fiber relative to the matrix. Fibers with small crimp amplitude or modest relative modulus are load bearing even at small strain. Such fibers raise the modulus of the composite, but not in a strain-hardening fashion. In contrast, large crimp amplitude and large relative modulus first straighten significantly without bearing significant load, and then bear increasing load once they become taut. This mimics the strain hardening behavior of collagen-containing tissues such as skin or arterial walls. Surprisingly high relative modulus values, on the order of 1000, are necessary to see significant strain hardening behavior. In summary, the degree of non-linearity and the extent of fiber loading can be controlled by changing fiber parameters such as fiber length, relative stiffness, and crimp geometry.

3.0 Mechanics of Multi-Fiber Composites with Short Crimped Fibers

3.1 Introduction

Fibrous collagen is observed in numerous tissues such as blood vessels, valve leaflets, intestine, ligaments, and tendons, and exists in the form of crimped fibers[39-41]. The crimp pattern of fibers gives the tissues strain hardening properties, wherein they act as soft materials at low strains as fibers uncrimp at low loads, but as stiffer materials at higher strains as fully uncrimped fibers become increasingly load-bearing[39-44, 46, 47]. Hence, soft tissues are often modelled as composites comprising stiffer fibers of helical[58] or planar sinusoid [50, 52, 57] geometries, embedded in a softer hyperelastic matrix, and their behavior has been modelled using finite element method for various types of fiber arrangements [50-57].

Inspired by this, we consider composites comprising stiff crimped fibers embedded in a soft matrix, which could provide similar strain hardening behaviors. Specifically, following the literature on chopped fiber-reinforced composites, we consider finite-length crimped fibers dispersed randomly in a matrix. The benefit of such short fiber composites is that they can be flow-processed by extrusion, molding, and extrusion-based 3D printing [57, 75-80], whereas continuous fiber composites cannot.

As a first step to understanding the mechanics of such composites, we previously studied [38] the stress transfer between a single finite length crimped fiber embedded in a softer matrix as the matrix is stretched. We showed that if the crimped fiber with a relatively high modulus (e.g. 1000-fold higher than that of the matrix), the fiber bore very little load at small strain; instead the stretching was almost entirely accommodated by straightening (i.e. uncrimping). At larger strain,

the fiber became increasingly load-bearing, analogous to the strain hardening contribution of a wavy collagen fiber. In contrast, crimped fibers with a relatively small modulus (e.g. 10-fold higher than that of the matrix) became load-bearing even at small strains, and hence did not behave in a strain hardening fashion. Incidentally, we also showed how the finite length of the fiber affected the results, specifically that each fiber was incompletely loaded near its ends, analogous to the shear lag effect [86] in straight-fiber composites. Since this end-section did not experience significant stretching, it also did not uncrimp significantly.

Moreover our results in the study showed that for a crimped fiber to have a significant non-linear contribution towards composite stiffness, the modulus ratio between the fiber and the matrix needs to be on the order of 1000 or higher [38].

In this chapter, we now turn to composites in which multiple crimped fibers are randomly dispersed into a matrix and test the extent to which the fibers confer strain hardening behavior in a realistic model of a fiber-reinforced composite. The central research questions to be tackled computationally are two-fold. First, how does composite mechanics depend on the loading of the crimped fibers? Specifically, due to the relatively large aspect ratio of the fibers, we anticipate significant interaction between the strain field surrounding each fiber, and the computations provide guidance on the volume fraction of dispersed fibers needed to realize the targeted mechanical behavior. Second, in a realistic material-processing operation, fibers are not likely to be perfectly aligned along the same direction. Thus, computations allow us to test how variations in alignment affect the mechanics. Computational approaches are especially powerful for this latter task because it is difficult to realize controllable alignments in experiments. We also compare the results of the multi-fiber simulations with the Equivalent Straight Fiber model from section 2.5.1 for predicting composite behavior from the behavior of a single embedded fiber, and to the

Holzapfel-Gasser-Ogden model[88] of tissues to show how crimped fiber composites may be regarded as fiber composites with a certain alignment angle of fibers.

3.2 Methods

3.2.1 Modelling and Simulations

We examined the mechanics of crimped fiber composites under tensile stretch using 3D finite element simulations. Crimped fibers were created and embedded in a soft matrix of dimensions L_m along the x-direction (stretching direction), H_m along the y-direction (width direction) and W_m along the z-direction (thickness direction of of the matrix).

The geometry of the matrix and fibers was modelled in Houdini. Similar to our previous research [38], the wavelength of the crimps was fixed at $\lambda = 40r_f$, where r_f is the fiber radius. The end-to-end length of each fiber was fixed at $2L = 10\lambda$. As the crimp amplitude of the fibers increased, the contour length of fibers also increased proportionately, in turn increasing the volume fraction of fibers in the sample, as shown in Table 3. 1. The fiber geometry was modelled as sinusoidal (Figure 3. 3 (D, E)) with circular cross-section. Four different fiber geometries with different amplitudes, corresponding to A/λ = 0 (straight fiber), 0.144, 0.192 and 0.25 were modelled. Normal of the fiber plane was set parallel to the z-axis and they were then distributed in the matrix using a randomized scatter function which allowed us to specify the number of fibers (n_f). Three different volume fractions of fibers were examined corresponding to n_f = 100, 200 and 300. A wrangle node in Houdini was used to determine the orientation (θ_f) of these fibers. Three different orientations were created for θ_f = 0° (fibers oriented in the direction of stretch),

fibers oriented randomly between $\{0, 180°\}$, and 90° (fibers oriented perpendicular to the direction of stretch). The matrix was modelled as a box with dimensions $H_m = 2400r_f, L_m = 2000r_f$ and $W_m = 80r_f$. The fiber distribution and the box were then intersected using a boolean node in order to cut off those parts of fibers which were out of the matrix. These models were then exported to fTetWild [89] meshing software. Adaptive mesh was used with number of elements in the fibers ranging from 227363 for straight fibers ($n_f = 200$) to 383324 for fibers with A3 geometry ($n_f = 200$) and total elements in geometry ranging from 12.3 million to 19.5 million. Doubling the mesh density did not change the results significantly, showing that the mesh density was adequate to correctly resolve the mechanics. Meshed models were then imported into FeBio software [90] for further simulations. Figure 3. 1 shows the detailed flow of the process used to model the geometry in Houdini. The details about the geometry are shown in Table 3. 1. Note that $\phi_f \propto n_f$ and hence the volume fractions for other n_f values can be obtained readily from the last column.

Table 3. 1 Details of fiber geometry for different crimp amplitudes of fiber

Fiber geometry name	A/λ	Fiber Contour Length	ϕ_f for $n_f = 200$
Straight fibers	0	$400r_f$	0.000379
A1	0.144	$472.5r_f$	0.000447
A2	0.192	$519.3r_f$	0.000492
A3	0.25	$585.2r_f$	0.000554

Neo-Hookean material model was chosen for the matrix and fibers. Since the single fiber study [38] showed that the relative stiffness of the fibers must be on the order of 1000 for the fibers to have a significant contribution, the modulus ratio (E_f/E_m) was fixed at 1000. Poisson's ratio of $\nu = 0.4$ was chosen for the material. The surface at x = 0 was constrained in space and a stretch of 1.5 was applied to the surface x = L_m in the positive x-direction using a rigid body connector.

All the other surfaces were unconstrained. Figure 3. 2 shows meshed simulation setup and Figure 3. 3 (A-E) show the geometry in detail.

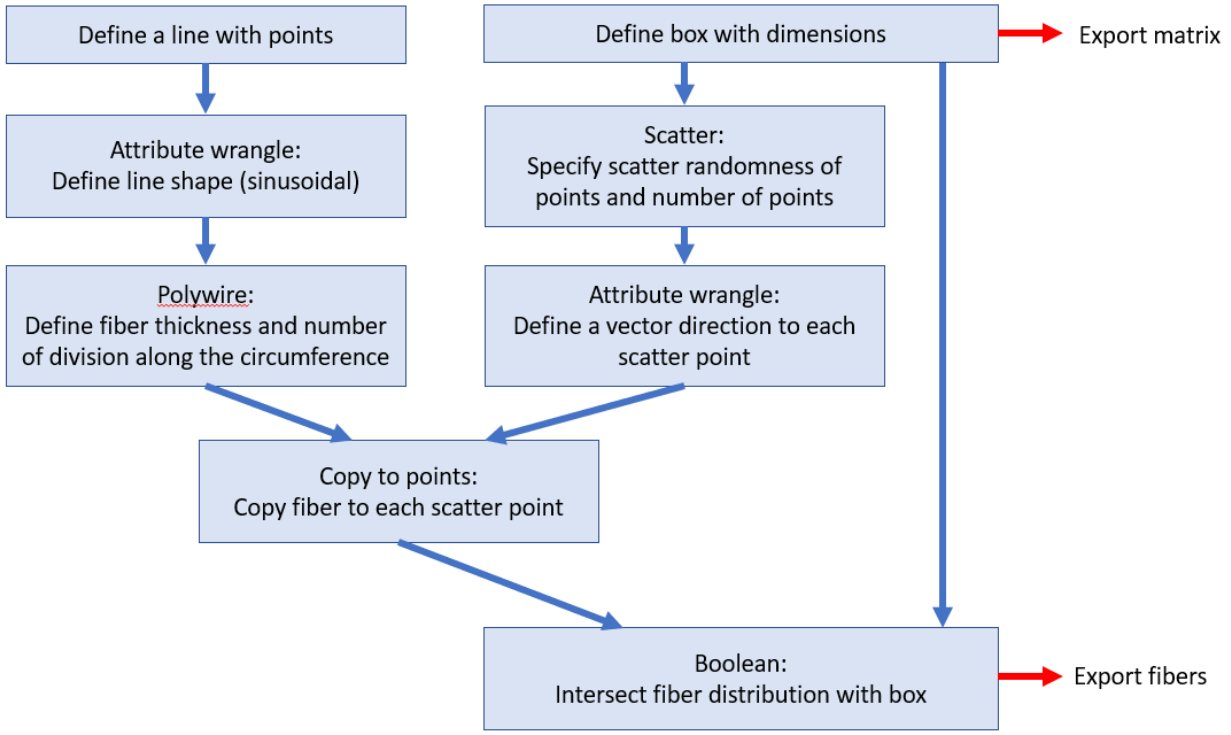

Figure 3. 1 Flow of process to model the fibers and matrix in Houdini

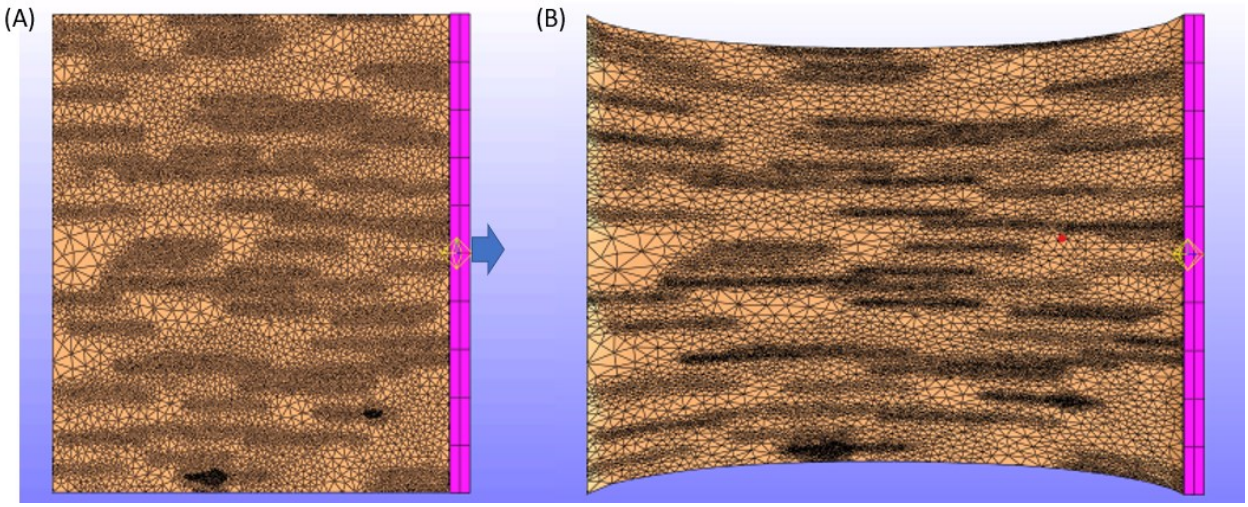

Figure 3. 2 Meshed simulation setup at (A) ε=0 and (B) ε=0.5

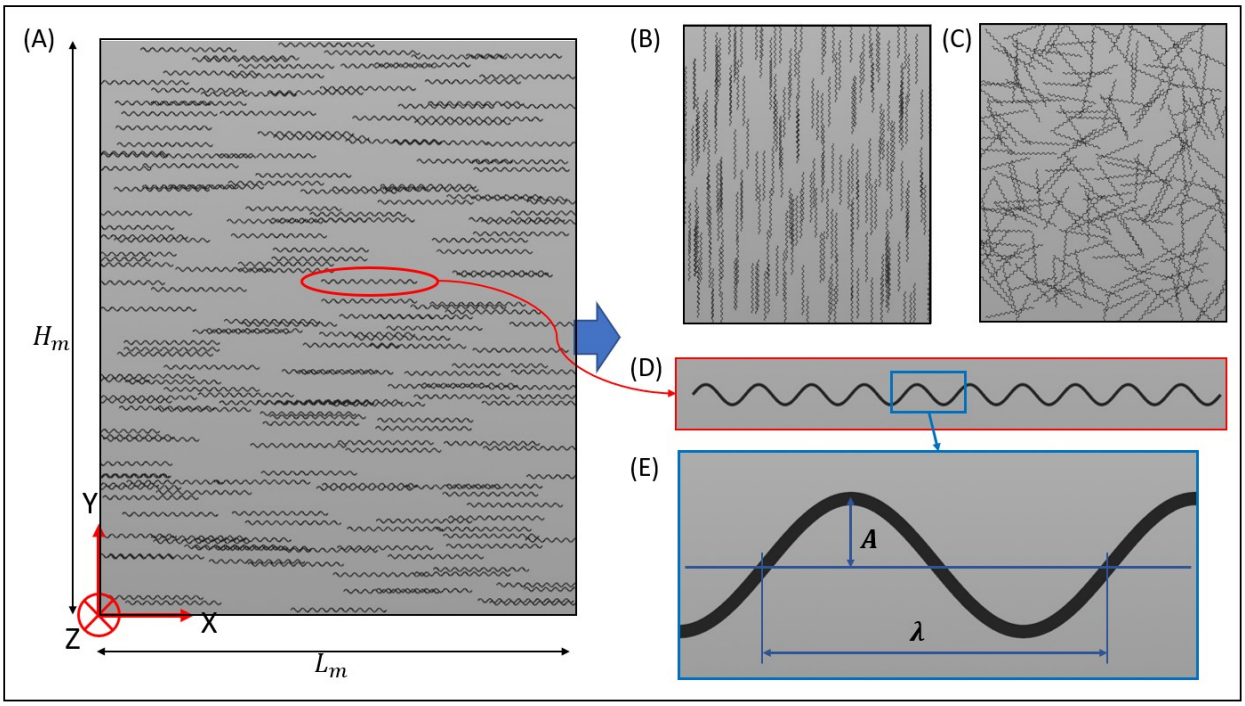

Figure 3. 3 Geometry modelled in Houdini

Geometry of composite with crimped fibers (geometry A2) for (A) $\theta_f = 0°$, (B) $\theta_f = 90°$, (C) $\theta_f =$ *random orientation*; (D) and (E) Close-up snapshot of the fiber showing sinusoidal geometry

Three sets of simulations were conducted where each of the three parameters (fiber amplitude, fiber orientation angle, and the number of fibers) were varied in turn, keeping the other two fixed. In the first, fiber orientation angle θ_f was fixed at 0° (oriented in the direction of stretch), n_f held fixed at 200, and fiber geometry was varied with increasing A/λ (straight fiber, A1, A2, A3). In the second set, the fiber was kept fixed at the A2 geometry, θ_f was fixed at 0° and volume fractions were varied corresponding to n_f = 100, 200, 300 fibers for straight fiber. In the third set, n_f was kept fixed at 200 with different$\theta_f = 0°, randomly\ oriented\ and\ 90°$) for straight fibers and for the A2 fiber geometry.

3.3 Results and Analysis

3.3.1 Effect of Amplitude

The effect of the added fibers can be illustrated from the difference in the stress between simulations of the composite vs the simulation of the matrix without embedded fibers (Figure 3. 4 (A)). Here σ and σ_m refer to the σ_{11} component of the true Cauchy stress for the simulations of the fiber-containing composites and the simulation of the matrix alone (without fibers) respectively. This stress is calculated by dividing the force experienced by the rigid body to attain a strain of 0.5, by the true cross-sectional area ($A_0(1-\nu\varepsilon)^2$). The fibers in these simulations are oriented at $\theta_f = 0°$, and the volume fraction corresponds to $n_f = 200$. It is seen from Figure 3. 4 (A) that straight fibers have a higher contribution to stress than the crimped fibers. The contribution of crimped fibers decreases with increase in crimp amplitude, showing that higher crimp leads to a softer behavior of the composite. Moreover, unlike the case of straight fibers, the contribution of crimped fibers increases more steeply (i.e. super-linearly) with strain. This is shown more clearly by comparing the fractional increase in stress relative to the no-fiber simulation ($(\sigma-\sigma_m)/\sigma_m$), as in Figure 3. 4 (B). This quantifies how the crimped fibers make only modest contribution to the stress at lower strains, but much more as the applied strain increases. The vertical lines in Figure 3. 4 correspond to the geometric straightening strain (ε_{geo}, when the end-to-end fiber length (2L) = contour length of the fiber) for the different geometries A1, A2 and A3. If the fibers were approximately inextensible (i.e. with low bending modulus, but high stretching modulus), one would expect them to uncrimp completely and become load bearing when at a matrix strain of

ε_{geo}. In this case we see that the fibers already become somewhat load bearing at the strain of ε_{geo} as was also noted for single embedded fibers [38].

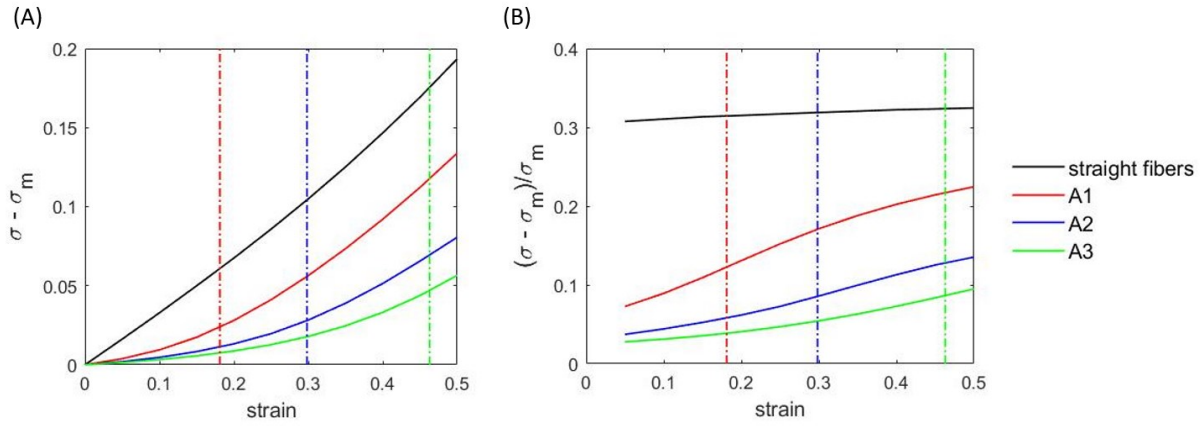

Figure 3. 4 Multi-fiber composites: effect of amplitude

(A) Difference between composite simulation stress and no-fiber simulation stress, and (B) relative increase in stress with respect to no-fiber simulation for straight fibers (black), A1(red), A2 (blue) and A3 (green), and vertical lines represent ε_{geo} for the crimped geometries.

3.3.2 Effect of Fiber Volume Fraction

Figure 3. 5 compares three different volume fractions corresponding to $n_f = 100, 200$ and 300, all for straight fibers oriented at $\theta_f = 0°$. The fiber contribution $(\sigma - \sigma_m)$ increases linearly with strain (Fig. 5A), and increases roughly proportionally to the volume fraction. The fractional increase in stress $(\sigma - \sigma_m)/\sigma_m$ is nearly strain-independent (Fig. 5(B)) and this value is also proportional to the volume fraction.

The simplest model for the tensile stress in a composite containing long, well-aligned fibers is to take a volume-weighted average $\sigma = \varepsilon(E_m + \phi_f E_f)$. The corresponding predictions are shown by the dot-dashed lines in Figure 3. 5, and are seen to overestimate the simulations. We

believe this is because in the simulations, there is a finite length near the end of the fiber (called shear lag length) where the fiber is incompletely loaded, and hence the ends of the fiber do not contribute as much as the central portion of the fiber. In contrast, the volume-weighted average assumes that the entire fiber is loaded, and hence over-predicts the stress.

Figure 3. 6 is similar to Figure 3. 5, except for crimped fibers of geometry A2, at orientation $\theta_f = 0°$. As compared to the straight fiber composites, for a strain up to 0.25, the crimped fiber contribution is lower than that of straight fibers, and the crimped fiber contribution increases non-linearly at higher strains. The vertical line corresponds to ε_{geo} for the crimped fiber and it can be seen from Figure 3. 6 (A and B) that the difference in stresses and relative increase in stress, both increase at a higher rate beyond the ε_{geo}.

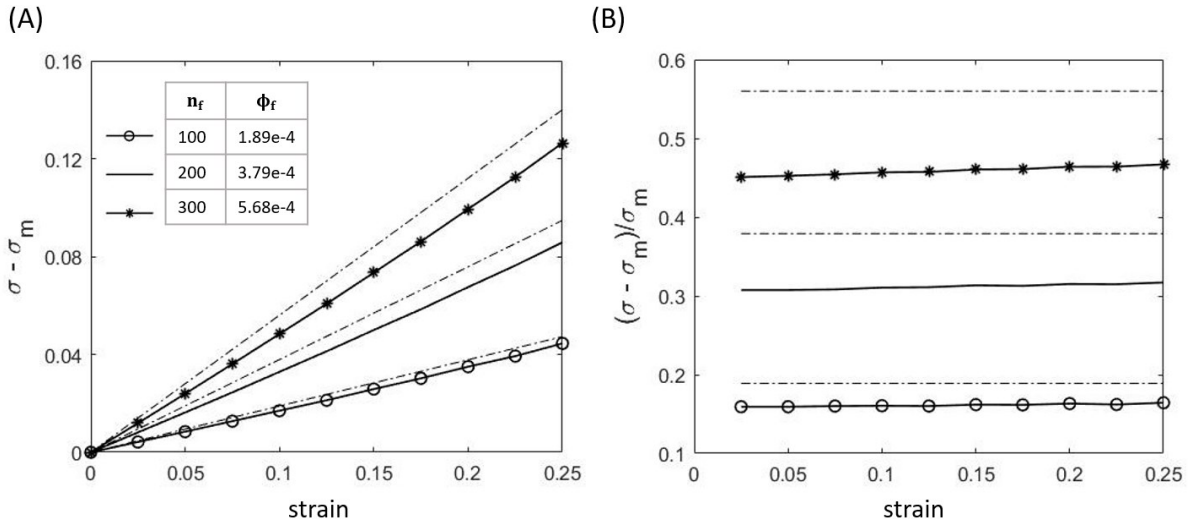

Figure 3. 5 Multi-fiber composites: effect of volume fraction for straight fibers

(A) Difference between straight fiber composite simulation stress and no-fiber simulation stress, and (B) relative increase in stress with respect to no-fiber simulation for $n_f = 100, 200$ and 300; and theoretical trend (dotted lines)

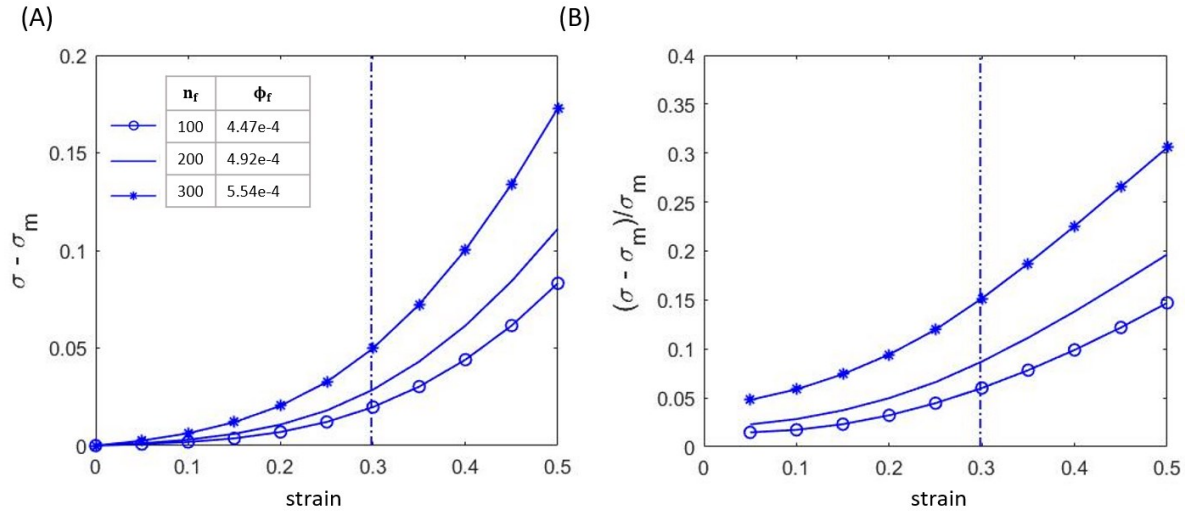

Figure 3. 6 Multi-fiber composites: effect of volume fraction for crimped fibers

(A) Difference between crimped fiber (geometry A2) composite simulation stress and no-fiber simulation stress, and (B) relative increase in stress with respect to no-fiber simulation for $n_f = 100, 200$ and 300; vertical line corresponds to ε_{geo}

3.3.3 Effect of Fiber Orientation

Three different orientations of the fibers were modelled: $\theta_f = 0°$ (fibers oriented in the direction of the stretch), $\theta_f = \{0, 180°\}$ (random orientation of fibers), and $\theta_f = 90°$ (fibers oriented perpendicular to the direction of stretch) (Figure 3. 3). The A2 geometry was used in all cases, and the volume fraction of fibers was kept constant ($n_f = 200$) for these comparisons. For straight fibers, the fiber contribution to the stress, $(\sigma - \sigma_m)$ increased approximately linearly with strain (Figure 3. 7 (A)) and therefore the fractional increase in stiffness was nearly strain-independent (Figure 3. 7 (B)). Fibers oriented in the direction of stretch contributed far more as compared to composite with random fiber orientation, whereas. Fibers aligned perpendicular to the direction of stretch hardly contributed since the matrix between the fibers bore the strain.

Similar results were observed for crimped fibers, except that similar to Figure 3. 4 and Figure 3. 6, the contribution for $\theta_f = 0°$ and randomly oriented crimped fibers was non-linearly incremental with strain (Figure 3. 8). However fiber contribution to the stress in the random case was found to be about 60% of that for the well-aligned case. This shows showing that the additional stiffness to the composite decreases as the crimped fiber orientation deviates from the direction of stretch. The central conclusion of this section is that even a random orientation of crimped fibers can give strain-hardening behavior, although the degree of strain-hardening is weaker than for uniaxially-oriented fibers. These results provide direct guidance to experimental implementations, since flow-processing of crimped fiber composites is unlikely to give perfect orientation of fibers.

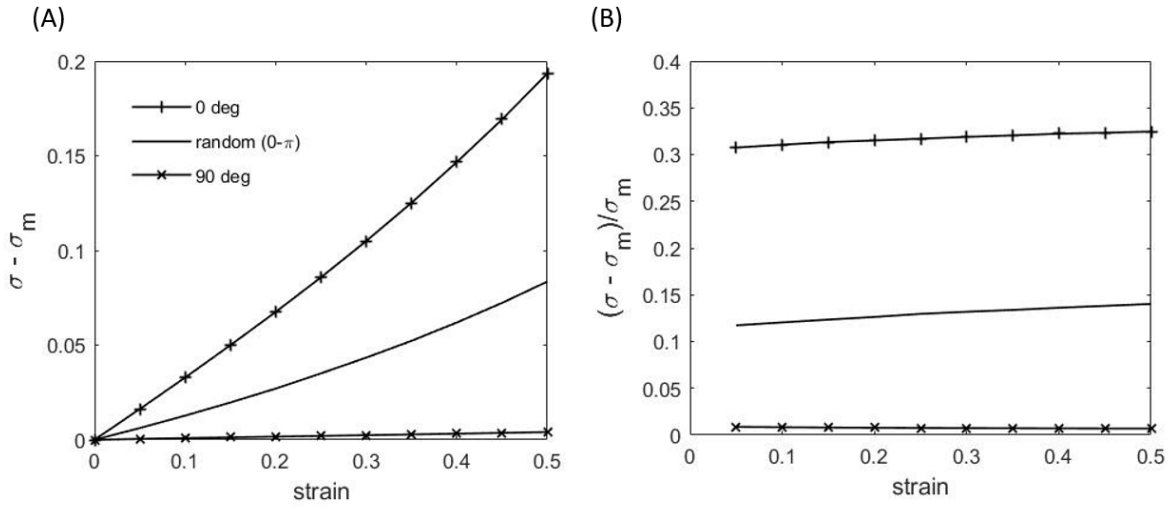

Figure 3. 7 Multifiber composites: effect of orientation for straight fibers

(A) Difference between straight fiber composite stress and no-fiber simulation stress, and (B) relative increase in stress with respect to no-fiber simulation for different orientations and $n_f = 200$

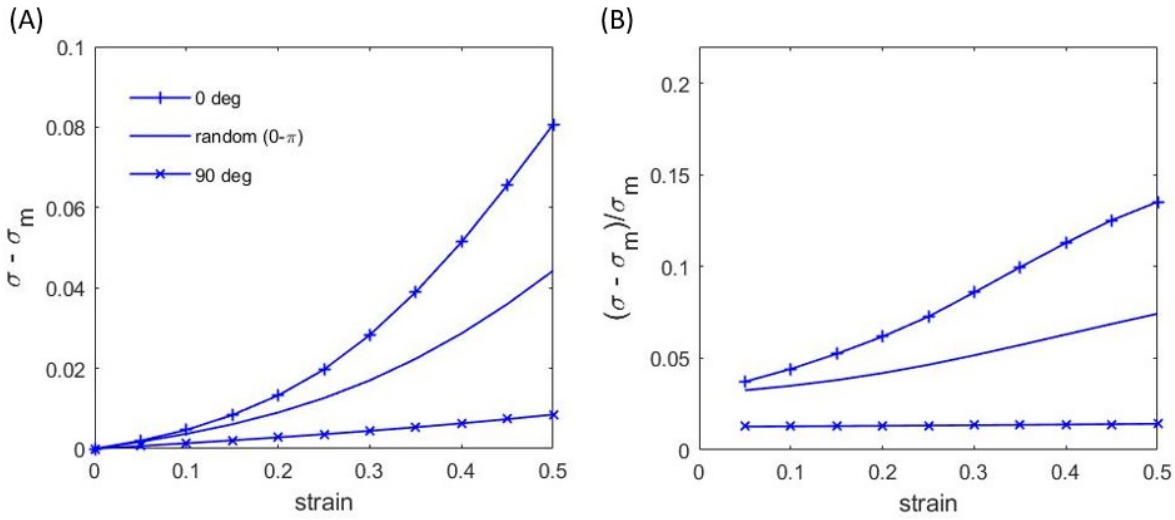

Figure 3. 8 Multifiber composites: effect of orientation for crimped fibers

(A) Difference between crimped fiber (geometry A2) composite stress and no-fiber simulation stress, and (B) relative increase in stress with respect to no-fiber simulation for different orientations and $n_f = 200$

3.3.4 Scatter-Seed Variability

Fiber distribution inside the matrix is determined by a randomized function in Houdini[], which creates seed points to which the fiber geometry is then copied. The number of scatter seed points is equal to the number of fibers (n_f). In order to look at the variability in the results when the scatter seed points are differently distributed, 5 different configurations of different scatter seeds were simulated for i) Straight fibers ($\theta = 0°, n_f = 200$) and ii) Crimped fiber (geometry A1, $\theta = 0°, n_f = 200$). The difference in stress and the no-fiber simulation stress for these two cases are plotted in Figure 3. 9 (A and B). Here Scatter_0 refers to the configuration whose results are presented in this study. The maximum deviation in stress from Scatter_0 configuration for straight fibers is {-0.48%,0.11%}, whereas that for crimped fibers (geometry A1) is {-0.13%,0.26%}. This

shows that different random configurations give similar simulation results, or equivalently, that the system size is sufficiently large to be statistically-meaningful.

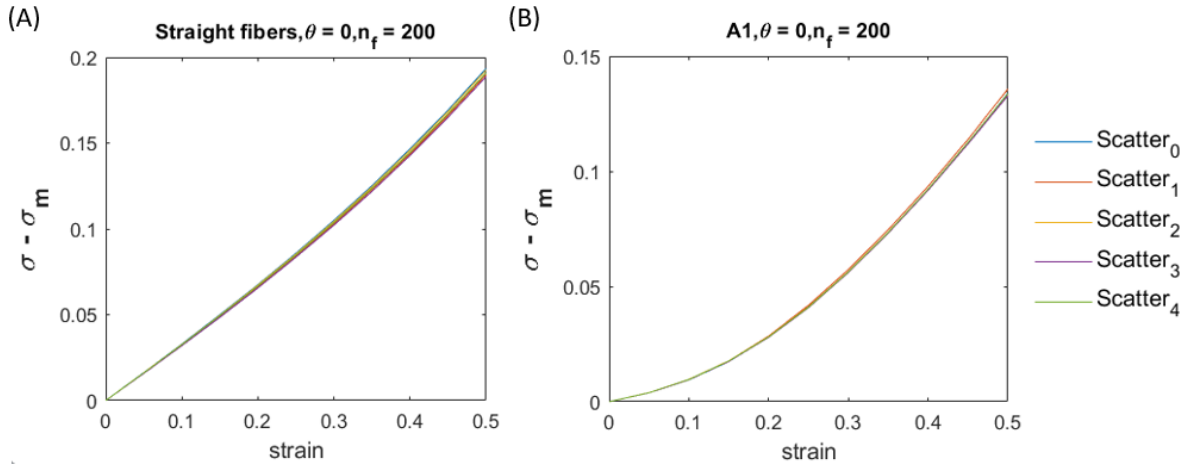

Figure 3. 9 Scatter-seed variability analysis

Difference in composite stress and no-fiber simulation stress for (A) straight fibers, and (B) Crimped fibers (geometry A1); for θ=0° and n_f=200

3.4 Discussion

The purpose of the simulations is to guide design of composites in which crimped reinforcing fibers confer strain hardening behavior. The results above show how the fiber geometry and volume fraction can be used to target the desired mechanical behavior. Yet, such simulations are computationally-expensive, and moreover require expertise in creating the geometries. It would be useful to have an approach that approximately predicts the mechanical behavior of a crimped fiber system without needing computationally-expensive multifiber simulations. Section 3.4.1 tests whether computationally-cheaper single fiber simulations, can predict the mechanical behavior of a multifiber composite. Section 3.4.2, tests whether the mechanical behavior by the

Holtzapfel-Gasser-Ogden model commonly used for tissue mechanics can predict similar results as the multi-crimped-fiber composites.

3.4.1 Equivalent Straight Fiber model

Previously [38] we showed that a single crimped fiber embedded in a softer matrix behaves like a softer fiber at lower strains and stiffer fiber at higher strains. Accordingly, it may be regarded as a equivalent straight fiber whose modulus increases with applied strain. The strain-dependent modulus (E_f^{eff}) of this Equivalent Straight Fiber (ESF) were obtained by fitting the in-fiber strain distribution to that expected for a straight fiber as per Cox's Shear Lag model. Here we test whether the same approach can be predict the strain-dependent modulus multi-fiber composites.

Simulations were conducted in the same geometry as Figure 3. 3, but with a single fiber at the center of the geometry aligned along the stretching direction. As previously, the strain distribution along the fiber was obtained and fitted to the distribution expected from the shear lag model:

$$\sigma_f(x) = E_f^{eff}\varepsilon\left[1 - cosh\left(\frac{n^{eff}}{r_f^{eff}}x\right).sech\left(n^{eff}\frac{L}{r_f^{eff}}\right)\right] \tag{3.1}$$

Here, E_f^{eff} is the effective fiber modulus which changes with applied strain, L and r_f^{eff} are the fiber length and effective fiber radius, and $n_f^{eff} = f(E_f^{eff})$. Figure 3. 10 shows the single fiber geometry along with the single fiber simulation data and the fitted Eq. 3.1 fit, for one of the fiber geometries (A2). $E_f^{eff}(\varepsilon)$ from the single-fiber simulations for the various crimp geometries are shown in Figure 3. 11, and as expected, the effective modulus of the equivalent fiber increases with strain (i.e. with uncrimping). Incidentally, the strain distribution in randomly-selected fibers

from the multifiber composite agrees well with this single-fiber strain distribution (Figure 3. 12), i.e. a typical fiber in the multifiber composite behaves similarly to that a single fiber an infinite matrix.

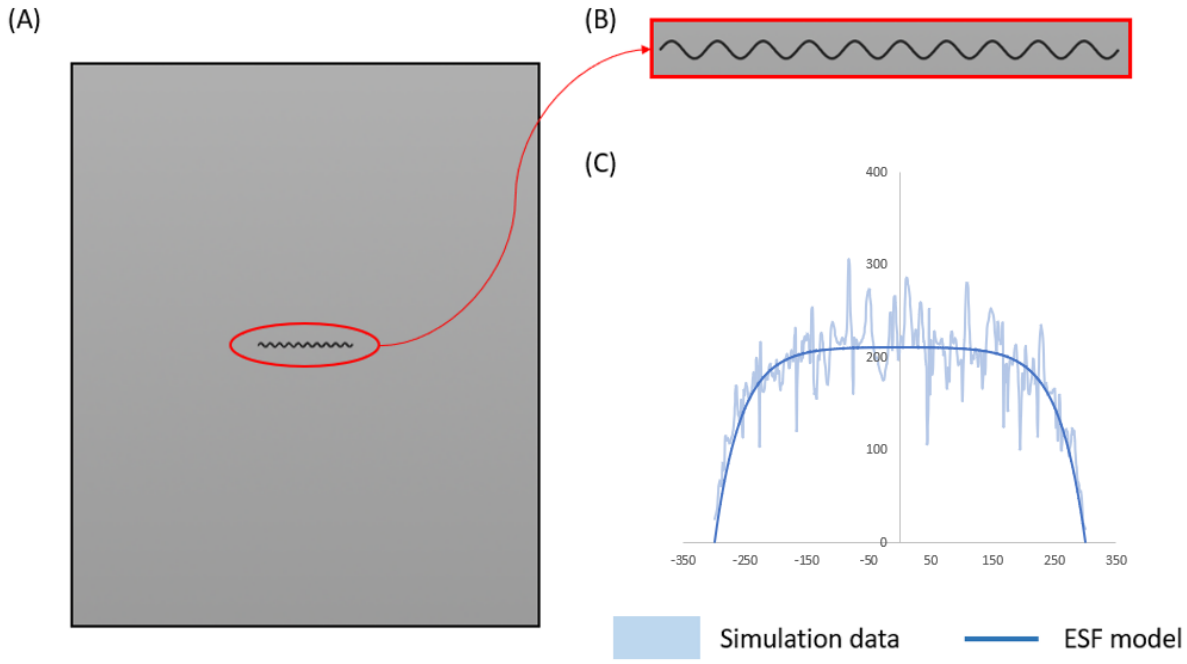

Figure 3. 10 Single fiber simulation geometry and fits

(A) Geometry of single fiber simulation for fiber geometry A2, (B) zoomed in fiber profile, and (C) stress data obtained from the single fiber simulation (pale data points) with ESF model fit (solid line); for fiber geometry A2

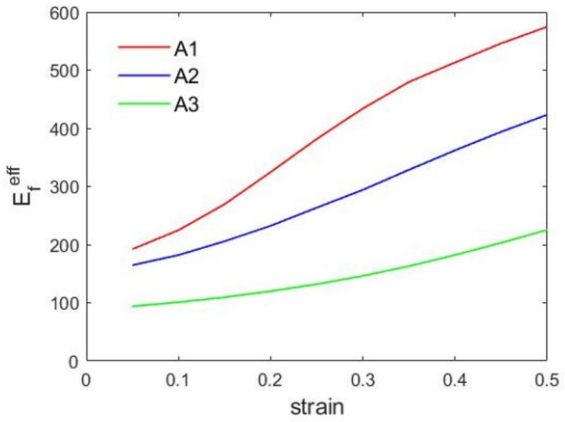

Figure 3. 11 Effective fiber modulus (E_f^eff) from single-fiber simulations using the ESF model for different crimp geometries

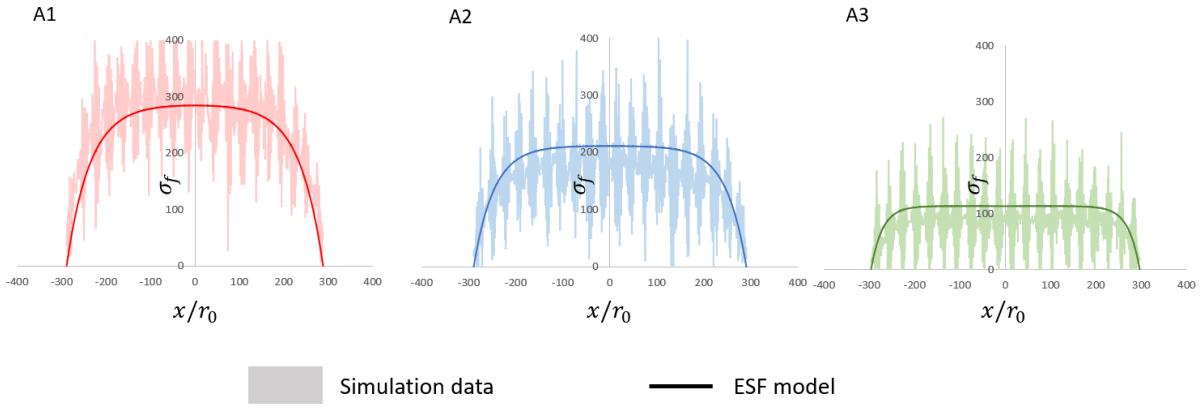

Figure 3. 12 Comparison of ESF with simulation data

Equivalent Straight Fiber model for crimped fibers using E_f^{eff} values obtained from single fiber simulations (solid line) and in-fiber stress data (light colored data points) for a randomly-selected single fiber embedded in the multifiber composite

The modulus of the composite can now be estimated from a simple volume-weighted average of the components:

$$E_{comp_{ESF}} = (1-\phi_f)E_m + \phi_f E_f^{eff} = \frac{\sigma_{matrix}(\varepsilon)}{\varepsilon} + \phi_f E_f^{eff} \tag{3.2}$$

Note that we have approximated $(1-\phi_f) \approx 1$ given the low values of ϕ_f. The corresponding predictions are compared with the multifiber composites in Figure 3. 13 (A and B) where the points are calculated by simply dividing the composite stress obtained from the simulations by the applied strain (σ/ε).

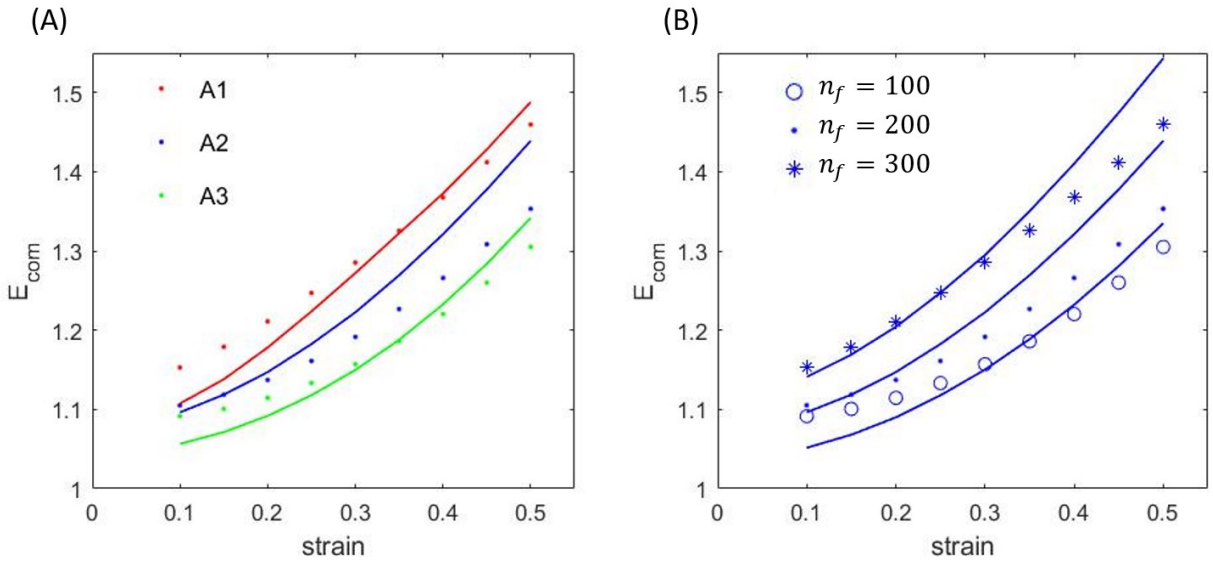

Figure 3. 13 Instantaneous composite modulus

E_{com} calculated using E_f^{eff} values from single fiber simulations (solid lines) and obtained from the multi-fiber simulations (dots) for (A) different crimp geometries, and (B) different volume fraction for A2 geometry

Figure 3. 13 shows a reasonable agreement between the multi-fiber simulation results and those predicted by the ESF model for a single crimped fiber. Thus, if a single fiber is considered equivalent to a straight fiber with a strain-dependent modulus, we can use the weighted linear approximation to estimate the composite modulus of multi-fiber composites. The predictions from the single crimped fiber are slightly higher at larger strains and slightly lower at smaller strains, nevertheless we emphasize that the solid lines are computationally inexpensive since only a single fiber must be simulated. This difference may be attributed to the interactions between fibers that occur in multi-fiber composites when the fibers are close to each other.

3.4.2 Modified Anisotropic HGO-C model

Holzapfel-Gasser-Ogden model [88] is commonly used to model the constitutive behavior of tissues since it allows the effect of fiber alignment to be accounted explicitly. We tested whether crimped fiber composites can be represented by the HGO model. We used the Modified Anisotropic HGO (MA HGO-C) [91] model for compressible materials for fitting the stress-strain curves obtained the above simulations of crimped fiber composites. Although in the HGO model, the strain hardening is attributable to strain-direction realignment of the fibers, these equations can capture any form of strain hardening including that due to crimps as considered here.

The MA HGO-C model for strain energy is as follows:

$$\Psi_{\mathrm{OGH}} = \Psi_{vol} + \Psi_{iso} + \Psi_{aniso} = \Psi_{matrix} + \Psi_{fiber} \tag{3.3}$$

where Ψ_{OGH} is the total HGO energy of the material, Ψ_{vol} is the volumetric part, Ψ_{iso} is the isotropic part and Ψ_{aniso} represents the anisotropic part of strain energy due to the fibers.

$$\Psi_{matrix} = \left[\frac{1}{2}\kappa 0(J-1)^2\right] + \left[\frac{1}{2}\mu 0(I_1 - 3)\right] \tag{3.4}$$

$$\Psi_{fiber} = \Psi_{aniso} = \frac{k_1}{2k_2}\sum_{a}^{N}\left(e^{k_2 E_a^2} - 1\right) \tag{3.5}$$

$$E_a = \kappa 0(\mathrm{I}_1 - 3) + (1 - 3\kappa)\left(I_{f_N} - 1\right) \tag{3.6}$$

where $J = \lambda_1\lambda_2^2 = \lambda_1\lambda_3^2$, when stretch $\lambda_1 = \lambda$, and the matrix is unconstrained in directions 2 and 3. κ = 0 if the fibers are perfectly aligned and $\kappa = 1/3$ if the fibers are oriented randomly (isotropic response). N is the number of fiber families. $\kappa 0$ is the bulk modulus and $\mu 0$ is the shear modulus given by $\mu 0 = E/2(1+\nu)$. Parameter k_1 represents some form of the stiffness contributed by the fibers. k_2 relates to the non-linear behavior of the composite. For this analysis

we considered there to be only two families of perfectly aligned fibers ($\kappa = 0$), oriented at an angle $\pm\alpha$ to the direction of stretch. Hence for fiber unit vector, $a_{0f} = [\cos\alpha, \sin\alpha, 0]$, we have

$$\Psi_{aniso} = \frac{k_1}{2k_2}\left(e^{k_2(I_f-1)^2} - 1\right) \tag{3.7}$$

$$I_1 = tr(C) = tr(F^T F) = \lambda_1^2 + \lambda_2^2 + \lambda_3^2 = \lambda^2 + \frac{2J}{\lambda} \tag{3.8}$$

$$I_f = a_{0f}(C\, a_{0f}) = \lambda_1^2 \cos^2\alpha + \lambda_2^2 \sin^2\alpha = \lambda^2 \cos^2\alpha + \frac{Jsin^2\alpha}{\lambda} \tag{3.9}$$

Derivative of eq (5) with respect to F gives expression for stress.

$$\sigma = \frac{1}{J} F \frac{\partial \Psi}{\partial \mathrm{F}} \tag{3.10}$$

$$\sigma_{fibers} = \sigma_{aniso} = \frac{2k_1}{J}(I_f - 1)\left(e^{k_2(I_f-1)^2}\right)(a_f \otimes a_f) \tag{3.11}$$

This gives us:

$$\sigma_{fibers} = 2\boldsymbol{k_1}\lambda^2 \cos^2\boldsymbol{\alpha}\left(\lambda^2 \cos^2\boldsymbol{\alpha} + \frac{sin^2\boldsymbol{\alpha}}{\lambda} - 1\right)\left(e^{\boldsymbol{k_2}\left(\lambda^2 \cos^2\boldsymbol{\alpha} + \frac{sin^2\boldsymbol{\alpha}}{\lambda} - 1\right)^2}\right) \tag{3.12}$$

The first principle stress (σ_{11}) is given by:

$$\sigma_{11} = \sigma_{matrix} + \sigma_{fibers} = \sigma_{matrix} + \sigma_{aniso_{11}} \tag{3.13}$$

Where

$$\sigma_{matrix=}\mu_0\left(\lambda^2 - \frac{1}{\lambda}\right) \tag{3.14}$$

In writing the above equations, where we assume two families of fibers oriented at angle $\pm\alpha$. Although in the HGO model, the strain hardening is attributable to strain-direction realignment of the fibers, these equations can capture any form of strain hardening including that due to crimps as considered here.

Eq. 3.13 provides 3 parameters, k_1, k_2 and α which must be fitted to the simulation data. Multiple combinations of these three parameters were found to give comparable fits to the data, and the following procedure was adopted to fit data for the various cases consistently. For straight fibers that are perfectly-aligned (i.e. alpha=0), as the strain approaches 0, Eq. 3.12 gives

$$\frac{\partial \sigma_{fibers}}{\partial \varepsilon} \; at \; \varepsilon \to 0 = 4k_1 \tag{3.15}$$

This can be equated to $\phi_f E_f$, which is the expected modulus for a fiber composite straight, perfectly-aligned fibers. Accordingly,

$$k_1 = \frac{\phi_f E_f}{4} \tag{3.16}$$

This value of k_1 was adopted in all cases. The parameter k_2 relates to the strain at which strain hardening appears. For well-aligned crimped fibers, the physical picture of uncrimping suggests that k_2 should be related to the strain required for geometric straightening (ε_{geo}). Specifically, fibers are expected to make a negligible contribution to the stress for $\epsilon < \epsilon_{geo}$, but increasing contributions for $\epsilon > \epsilon_{geo}$. Based on this physical insight, k_2 was selected to be the value at which $\sigma_{fiber} = 1.03 \times \sigma_{matrix}$, i.e. the fiber contribution became 3% of the matrix contribution. The value of k_2 thus obtained was nearly insensitive to the α value used. In summary, the values of k_1 and k_2 were pinned down based on the composition and the crimped geometry respectively. The remaining fitting parameter, α, was then obtained by fitting the simulation data. The corresponding fits are shown in Figure 3. 14, and all the model parameters are shown in Table

3. 2. The central observation is that within the HGO framework, the varying degrees of crimp may be regarded as equivalent to straight fibers at specific angles as illustrated in Figure 3. 15. Since according to the HGO model, higher α corresponds to a slower increase in the modulus of the composite, these fits are in accordance with our results that for a higher crimp amplitude, the onset of strain-hardening is at a higher applied strain.

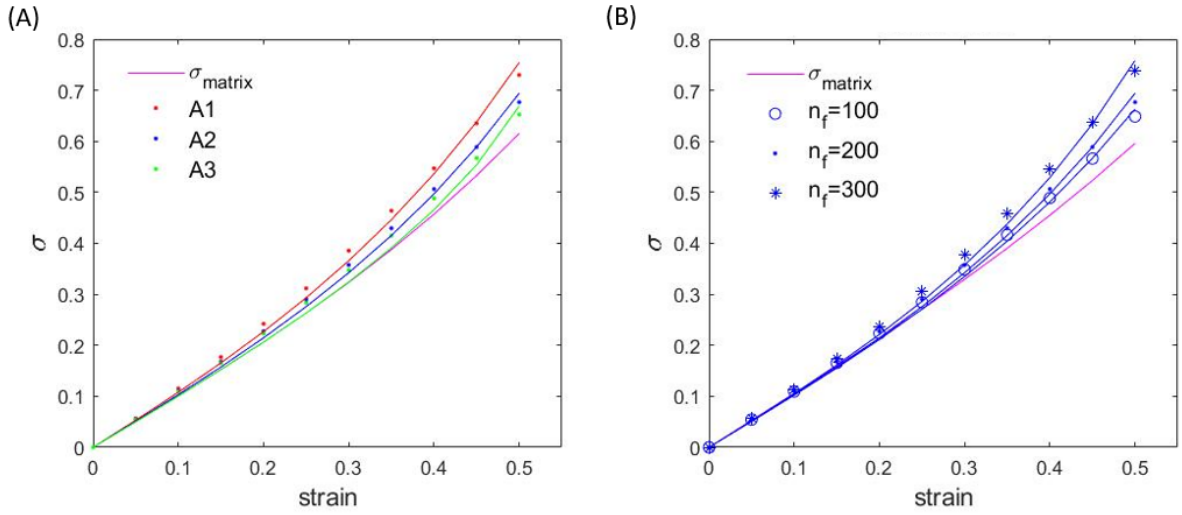

Figure 3. 14 MA-HGO-C fits

MA HGO-C fits (solid lines) and simulation data (datapoints) for (A) Different fiber geometries with $\theta = 0°$, $n_f = 200$ (B) Different volume fractions for fiber geometry A2 and $\theta = 0°$

Table 3. 2 HGO fit parameters

Parameter values used (k_1, k_2) and obtained fit (α) from the MA HGO-C model fits, for composites with different fiber geometries and different volume fractions

Fiber	n_f	E_f	ϕ_f	k_1	k_2	α (°)	R^2
A1	200	1000	4.47e-4	0.112	1	47.05	0.998
A2	200	1000	4.92e-4	0.123	3	53.57	0.998
A3	200	1000	5.54e-4	0.139	40	59.78	0.997
A2	100	1000	2.46e-4	0.0614	3	52.80	0.999

A2	300	1000	7.38e-4	0.184	3	52.81	0.997

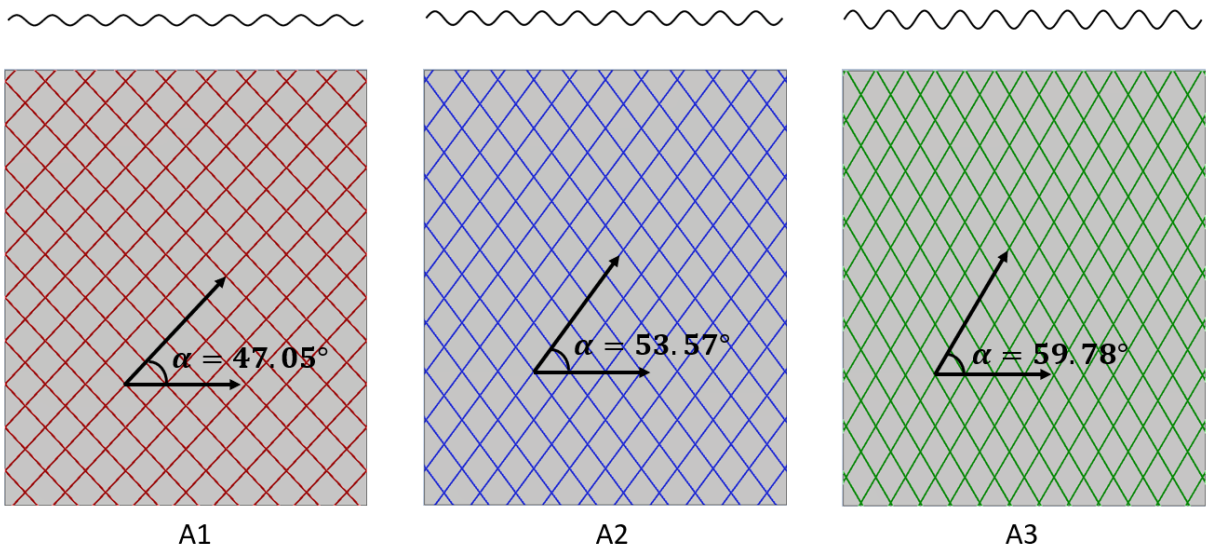

Figure 3. 15 HGO equivalent configurations

Equivalent configurations for HGO model with two families of fibers oriented at angle α to the stretch direction fitted for fiber geometries A1, A2, A3 with $n_f = 200$ and $\theta_f = 0°$ (shown on top)

3.4.3 Experimental Verification

In order to verify the results of the multi-fiber simulations, we fabricated composites with chopped fibers embedded in a soft silicone matrix. These fibers were obtained by separating the individual filaments of a polyester sewing thread. These fibers had diameter of 15μm and had a mild waviness due to the twisted nature of the sewing thread with an average amplitude to wavelength ratio of 0.05. The fibers were cut to a length of 4-5 mm and mixed with soft silicone (Ecoflex 00-20 (E_m = 40 Kpa)) after undergoing plasma treatment for better adhesion. Volume fractions of the fibers are listed in Table 3. 3. A major challenge in fabricating these composites is getting an orientation of the fibers. A stretch-mold setup was used in order to achieve fiber

orientation, where the mold was made out of a stiffer silicone (M4136) and after the silicone with chopped fibers was poured into the mold, the mold was stretched to a strain of 1. This allowed the fibers to orient themselves in that direction due to viscous shear forces in the uncured silicone during stretching. The mold was held in this position until the silicone cured. Figure 3. 16 (A) shows a cartoon schematic of the stretch-mold setup. Qualitatively, a reasonable fiber orientation was obtained with an approximately $\pm$ 10° variation as seen in Figure 3. 16 (B and C), which show the resulted cured sample with oriented fibers.

Table 3. 3 Volume fraction and orientation details of experimental samples

Sample	$E1_0$	$E2_0$	$E3_0$	$E2_{rand}$	$E2_{90}$
Preferred orientation	0°	0°	0°	random	90°
Measured ϕ_f (w/w)	3.95e-4	7.91e-4	1.17e-3	7.99e-4	7.83e-4

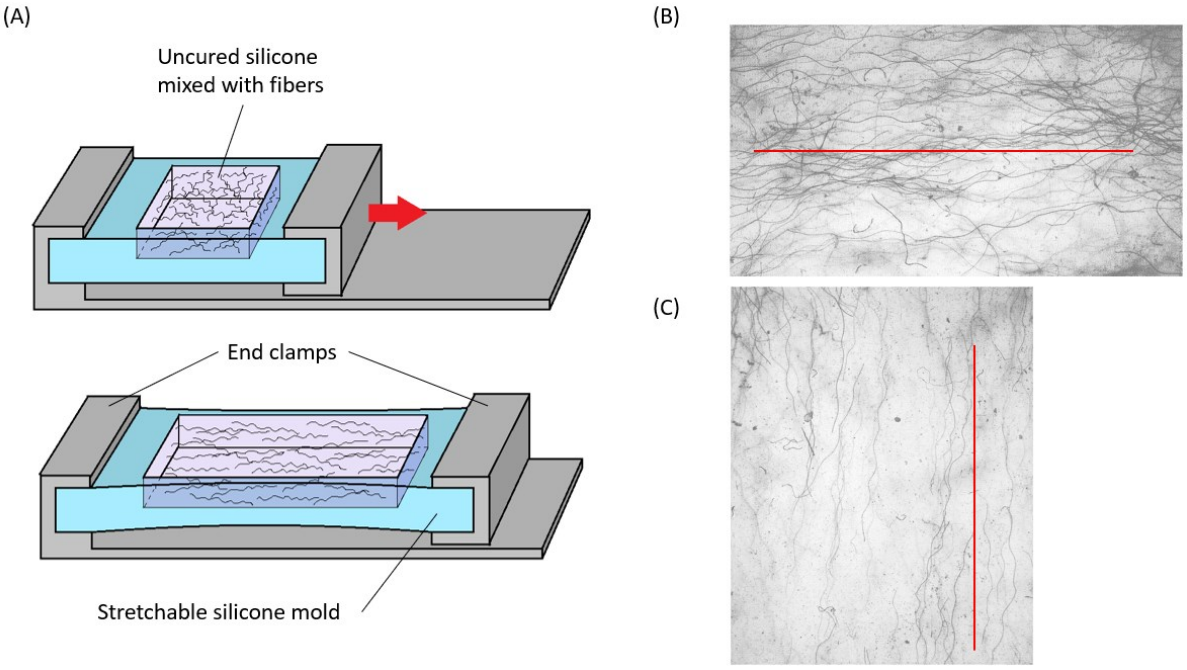

Figure 3. 16 Multifiber composites experimental setup

(A) Schematic of stretchable mold setup for achieving fiber orientation, (B) camera image of sample with fibers oriented at $\theta_f = 0°$, (C) camera image of sample with fibers oriented at $\theta_f = 90°$

The effect of volume fraction and orientation on the composite behavior seen in the simulations was verified by doing tensile stretch tests on the cured samples. Similar plots as those in section 3 were plotted, where the composite stress was compared against stress for the silicone without any fibers. Relative increase in stress ($(\sigma - \sigma_m)/\sigma_m$) are shown in Figure 3. 17, for different volume fractions (A), and for different fiber orientations (B).

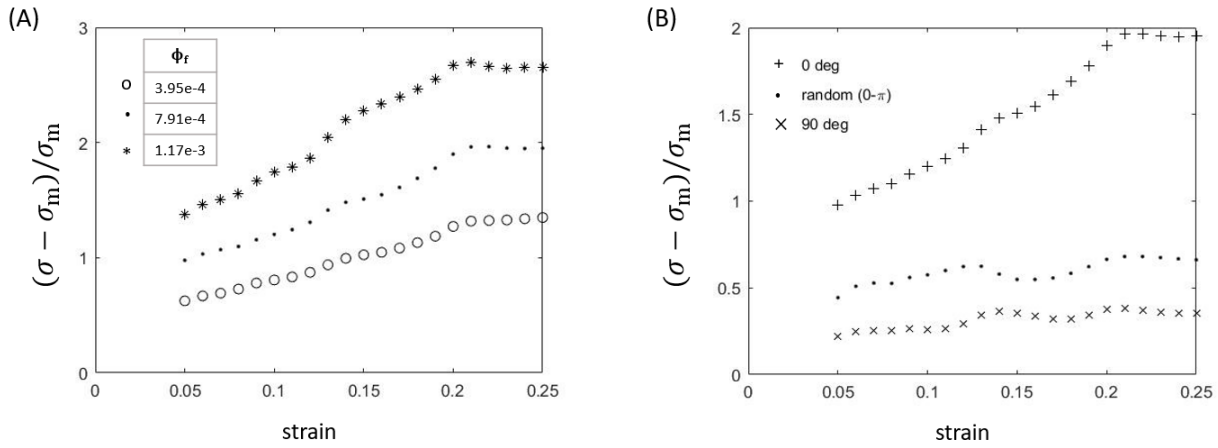

Figure 3. 17 Tensile test results for experimental samples

Relative increase in stress with respect to no-fiber silicone for (A) different fiber volume fractions ($\theta_f = 0°$) and (B) Different fiber orientations ($\phi_f = 7.91\text{e-}4 \pm 1\%$)

Consistent with the simulations, the fiber contribution increases with increasing fiber volume fraction and is maximum when the fibers are oriented in the direction of stretch. The wavy nature of the fibers is evident from Figure 3. 17, where the relative fiber contribution increases with applied strain showing evidence of some strain hardening behavior.

As seen in Figure 3. 17 (B and C), the orientation of the fibers deviates from the desired orientation by $\pm 15°$. The rate at which the stretchable mold is stretched and the viscosity of the uncured silicone affects the shear flow in the uncured silicone and can potentially affect how well the fibers get oriented. The effect of this rate of stretching the mold and viscosity needs to be quantified in order to have better control over the orientation. Volume fraction of the fibers also

affects the orientation since higher volume fraction corresponds to higher chances of the fibers getting tangled. Another challenge is to limit the gross bending of the fibers during alignment.

3.5 Summary and Conclusion

Extending our previous study for the stress transfer behavior of a composite with single stiffer crimped fiber embedded in a large matrix, we now quantify the mechanical behavior of multi-fiber composites containing crimped fibers. The response of multi-fiber composites depends upon fiber parameters like the fiber geometry (straight or crimped), fiber volume fraction and fiber orientation. This was studied for sufficiently stiff fibers (modulus ratio E_f/E_m = 1000) by varying the above-mentioned parameters. Contribution of the fibers decreases with the amount of crimped. Crimped fibers contribute less at lower strains and higher at higher strains, thus giving evidence of strain-hardening behavior. Higher volume fraction leads to higher fiber contribution to overall composite stress. Maximum contribution of the fibers is when they are all oriented in the direction of the stretch and lowest contribution is when they are all perpendicular to the direction of the stretch. The HGO model agrees with the crimped fiber composite behavior in that higher crimp amplitudes correspond to a larger HGO fiber orientation angle (α), meaning that the onset of strain hardening is at a larger applied strain. The ESF model suggested by us in the single fiber study can be extended to a multifiber study by weighted linear extrapolation based upon the mechanical response of a single fiber simulation.

We thus have a mathematical basis for a crimped fiber composite material for soft tissue substitutes, i) which gives strain-hardening response to uniaxial tension, ii) which consists of short crimped fibers which give the advantage of being flow-processible, and iii) the properties of which

can be altered by changing the fiber crimp geometry, volume fraction of orientation. This material thus can be used as soft tissue replacement for tissues with a range of mechanical behaviors. The relevance of the simulations results was shown by fabricating chopped fiber composites with stiffer polyester fibers embedded in soft silicone matrix. The central experimental challenge is the increasing difficulty of uniformly dispersing the fibers into the matrix as the fiber fraction increases. This challenge is not unique to crimped fibers, but appears even in composites of chopped straight fibers.

4.0 Concluding Remarks

In this dissertation we study the straightening of wavy structures in arteries and the role they play in the morphological and the mechanical aspects of the tissues. Part 1 presented a study on the morphological aspect where the relevance of Internal Elastic Lamina (IEL) corrugations under physiological conditions. This study strongly supports the conclusion that the arterial lumen is corrugated under physiological conditions, and the IEL contour length is at least 10% longer than the inner circumferential length of the artery under physiological conditions. It was also seen that the IEL corrugations flatten as the artery diameter increases, as seen from the reduction in corrugation amplitude (Appendix A Figure 1) and the corrugation factor (Figure1. 8) with the increase in arterial diameter. This means that as the arteries change diameter, which occurs as they dilate and constrict under physiological pulsation, the arterial lumen exhibits a dynamic topography. Such a dynamic topography can have potential function as a self-cleaning mechanism for reducing thrombotic activity[36, 37]. This can thus potentially be implemented into fabricating vascular grafts with a wrinkled lumen with dynamic topography[36, 37]. A corrugated luminal surface also provides increased surface area for nutrient transport and in case of smaller arteries, can potentially influence the flow of blood through the graft. In Section 1.01(a)(i)Appendix B, we provide a facile method for fabrication of such tubes with luminal topography. In this section we also show how the luminal corrugation wavelength and amplitude can be controlled by changing the parameters such as the thickness ratio of tube wall to lumen, prestrain applied in order to create the topography and the possible effect of the modulus ratio of the tube wall material to the lumen material. These tubes can be made to suit the size of the targeted artery and have potential applications as vascular prosthesis.

In Part 2 of this research, we made progress towards synthetic analogs to soft tissues. Biological tissues contain collagen in the form of crimped fibers which uncrimp as the tissue is stretched. The fibers bear lower loads at smaller strains and become increasingly load bearing as they uncrimp, thus imparting a strain-hardening behavior to the tissue, where in the tissue stiffness increases with increasing strain. We proposed a composite material comprising short stiffer crimped fibers embedded in a softer matrix that can show strain-hardening properties. The degree of strain-hardening of such composites can be controlled by varying the parameters like fiber crimp amplitude, fiber:matrix modulus ratio, fiber volume fraction and fiber orientation.

4.1 Comparison with the arterial wall

The synthetic composites developed in part 2 are inspired by tissues containing collagen fibers. Specifically, the crimped fibers sought to reproduce one aspect of collagen fibers, viz. that they are wavy. Only under tensile deformation do they straighten and become load bearing. Although we sought to mimic this aspect of tissues, in fact, there are many differences between our composites vs collagen-containing tissues. In this section, we will briefly comment on these differences.

The arterial wall of muscular arteries is composed of 3 layers: the innermost intima, followed by the media, and the outermost adventitia [1-5]. The intima consists of a continuous layer of endothelial cells lining the lumen of the artery. The media consists of elastin lamellae, collagen fibers and smooth muscle cells, and the adventitia primarily consists of large bundles of crimped collagen fibers and fibroblast cells [1-5]. Elastin in the arteries functions in restoring the tissue to its original configuration whereas collagen fibers exist in the form of crimped fibers which

uncrimp and provide increasing resistance to the tissue as it gets stretched, thus limiting the extent of stretch. The modulus of elastin obtained from aorta is between 0.15 – 0.41 MPa and the modulus of collagen fibers under uniaxial tests is between 300 – 2500 MPa [3, 5, 92], thus providing with a modulus ratio between 2000-5000. This compares with a ratio of 1000 used in most of our simulations.

Chow et al. [3] conducted a biaxial study on porcine thoracic aortic specimens, where in the orientations of collagen and elastin fibers in the media and adventitial were observed. Collagen fibers in the media and the adventitia are largely oriented circumferentially with the ratio of circumferentially: longitudinally oriented fibers being ~ 2 for medial collagen fibers and ~3 for adventitial collagen fibers. Thus, the arterial tissue has different mechanical properties in the circumferential and longitudinal directions. This can also be seen from the stress-strain curves from tensile tests conducted on porcine aorta [92, 93], where the stress when stretched in the circumferential direction is around 30-40% higher than that when stretched in the longitudinal direction. Collagen fibers intersect with each other with the average fiber length between intersections being around 4 times the fiber diameter[94]. This leads to crosslinking of the fibers[3, 94]. Such crosslinking is not present in our samples. Instead the fibers are dispersed individually with no physical linkages between them. Indeed crosslinking would be undesirable since they would make flow-processing impossible, whereas flow-processing is the chief benefit of chopped fiber composites.

Collagen and elastin concentrations vary in different arteries [94-96]. Collagen content (w/w dry) is around 37.5-43 % in the ascending aorta, common iliac arteries, 47-51% in the abdominal aorta and internal iliac arteries, and 33-44% in external iliac arteries, whereas elastin content is around 43-50% [94]. Change in the concentrations of collagen and elastin affects the

mechanical properties of the arteries. Concentrations of collagen and elastin also vary with age and disease [95, 96].

In order to compare the strain-hardening behavior of the arterial tissues in this study to that obtained from the multifiber simulations, we can compare the ratio of incremental modulus at 30 %:10% strain, obtained from the study by Dai et al [92] to that from our study. The 30%:10% incremental modulus ratio for arteries is around 1.9, whereas it is ~1.15 for a simulation with $n_f = 200, \frac{A}{\lambda} = 0.192$ and orientation = 0°. To reach the higher value for arteries, it would be necessary to increase the crimp amplitude, and possibly also the fiber loading.

In short, there are many variables when trying to replicate the structure of the arterial tissue. However, we propose that the mechanical response of the arterial tissue can be replicated by a composite with a simpler composition – short, stiffer crimped fibers embedded in a soft matrix. Elastin in the arteries can be said to be analogous to the soft elastic matrix, and the collagen fibers can be analogous to the stiffer crimped fibers in the crimped fiber composite. The modulus ratio modelled in this study is lower than that observed in the arteries. The anisotropic behavior due to different orientations of the collagen fibers in different layers can be achieved in case of the crimped fiber composite by changing the orientation of the crimped fibers, where the maximum increase in stress is obtained when the fibers are oriented in the direction of stretch (Figure 3. 8). Concentrations of collagen and elastin can be accommodated by fiber volume fraction in the composite. The degree and onset of strain-hardening increases with increase in fiber crimp amplitude and fiber:matrix modulus ratio. Thus, by changing the combination of fiber material and geometry parameters, the mechanical response of the crimped fiber composite can be tuned to match that of the arterial tissue.

In taking this study further, the next logical step would be to obtain the optimum combination of parameters for the crimped fiber composite in order to match the mechanical response of the arteries. This can be combined with the study in Part 1 to fabricate vascular grafts with mechanical properties similar to those of arterial tissue and with luminal topography. This study of crimped fiber composite as a synthetic tissue substitute is not limited to vascular grafts, but by finding optimal combinations of fiber parameters, can be extended to match the behavior of other soft tissues as well.

Fabrication of the synthetic material can then be done with these optimal combinations of fiber parameters. The experimental samples made in this study included composites made with fibers that were roughly 4 mm long and 15 μm in diameter. In order to fabricate samples that can substitute thin tissues like the vascular wall or skin, the fibers will have to be much smaller in size. Crimping fibers which are on the scale of few microns in length, and getting controlled and desired crimps is a challenge in microfabrication and would require more sophisticated setups than those demonstrated in this study. Another challenge is finding materials for the matrix and the fiber that are biocompatible and which have the desired mechanical properties, and this would involve biocompatibility studies. Also, the method of orienting the fibers within the matrix would need to be further developed for better control over getting the desired fiber orientation, for example, orienting the fibers circumferentially in the case of vascular grafts. Finally, flow-processing of fiber-containing composites is challenging since the viscosity increases drastically as the fiber loading increases. This is not unique to crimped fibers, but relevant to any fiber-reinforced composites. Thus careful design of flow processing would be needed to maintain fiber orientation in the final composite.

Appendix A : Investigation of the Internal Elastic Lamina – Supplementary Information

Appendix A.1 Corrugation amplitude

Average corrugation amplitude was calculated from the cross-section images. The inner boundary of the IEL obtained as points in polar coordinates Figure1. 6(C) was averaged over 5-6 wavelengths to obtain a smoothed curve that roughly passes through the middle of every amplitude. Appendix A Figure 1 shows the IEL data in polar coordinates and the averaged data. The root-mean-square deviation between the averaged curve and the IEL boundary data gave the deviation of the corrugations from the averaged central curve. The amplitude was then calculated as twice the RMS deviation. Corrugation amplitude is plotted for the cross-sections in Appendix A Figure 2.

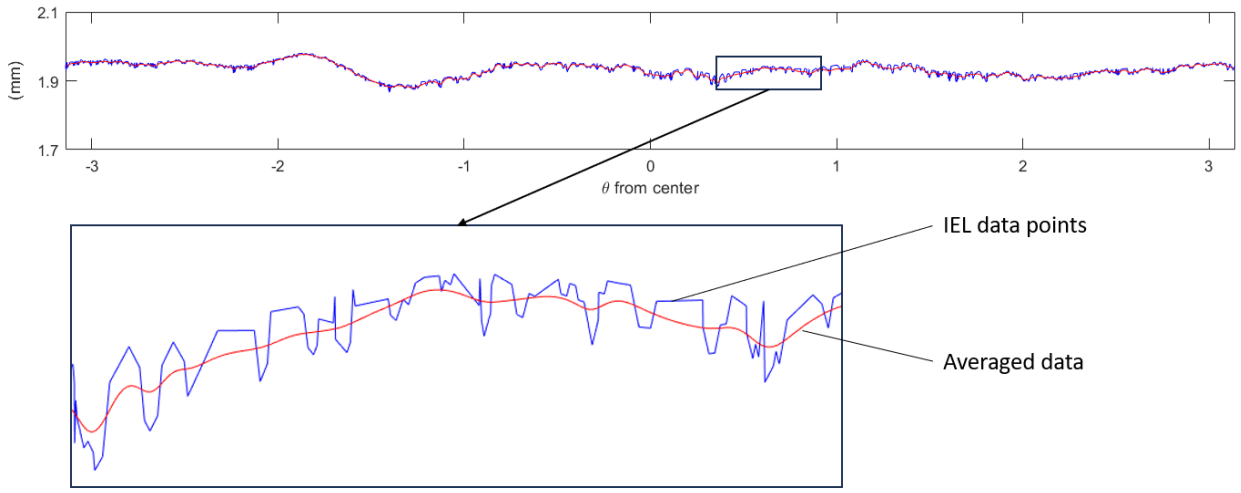

Appendix A Figure 1 Showing IEL data points and averaged data

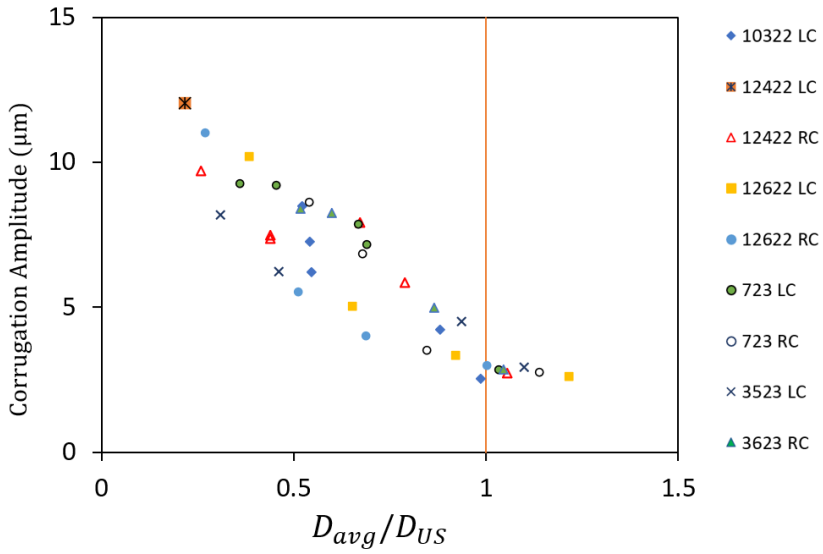

Appendix A Figure 2 Corrugation amplitude vs normalized cross-section diameter

In tandem with studies mentioned above, the corrugation amplitude, averaged over the cross-section of the artery decreases as the normalized diameter of the artery increases, showing that the IEL flattens as the arterial diameter increases. The vertical line in the figure corresponds to a cross-section diameter equal to that observed in ultrasound. The values of amplitude as the D_{avg}/D_{US} approaches 1 are less reliable due to the values of data and averaged data are very close.

Appendix A.2 Range of Artery Diameters Analyzed

Appendix A Figure 3 shows the range of artery diameters that were obtained from the animals. Normalized by the ultrasound diameter, this plot shows us where the data points fall on the x-axis in Figure1. 8.

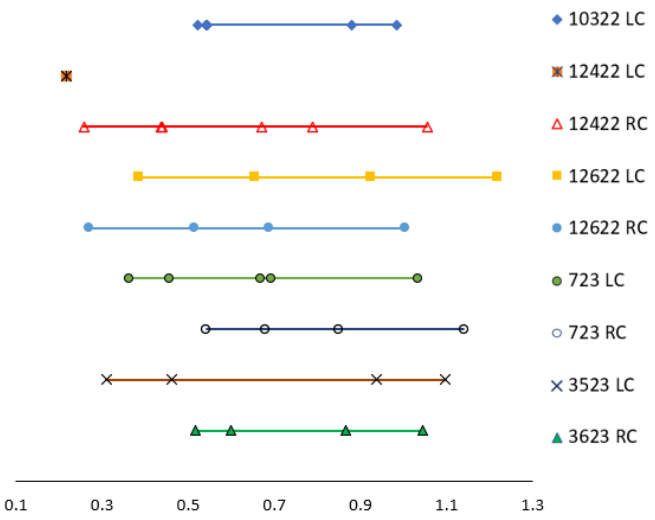

Appendix A Figure 3 Range of D_{avg}/D_{US} obtained for different arteries

Appendix A.3 IEL Contour Length for Arterial Cross-Sections

IEL Contour length (L_c) calculated from the images of arterial cross-sections was plotted against the diameter of the cross-sections (D_{avg}). It is seen qualitatively from Appendix A Figure 4, that the L_c increases with D_{avg} (shown in black dashed line). Increase in IEL contour length shows that the IEL is not inextensible but stretches as the artery is stretched.

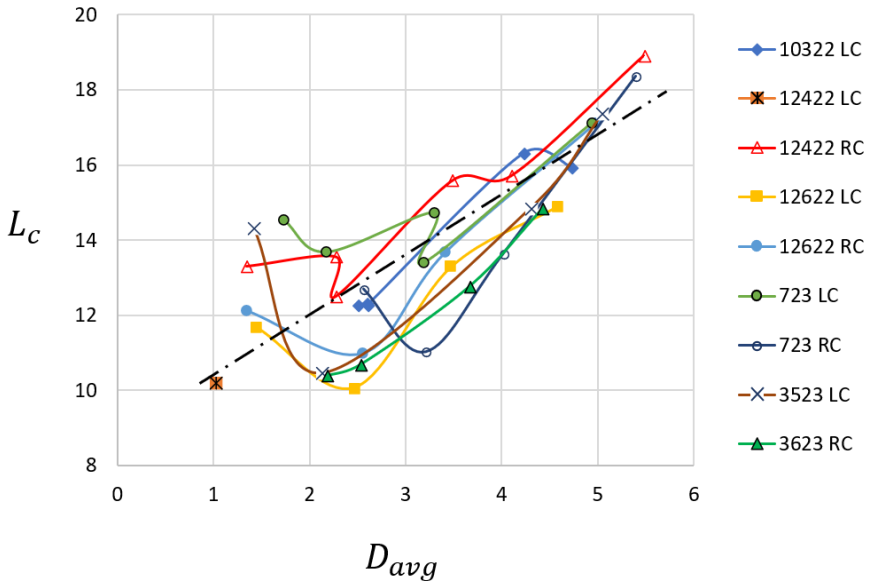

Appendix A Figure 4 L_c *vs* D_{avg} for different cross sections, showing increase in L_c with increase in diameter

Appendix A.4 Details of Study Animals

Appendix A Table. 1 lists details of the animals (pigs) whose arteries were considered in this study.

Appendix A Table. 1 Weight and gender information of pigs

Pig ID	Weight (kgs)	Gender
P10322	41	F
P12422	50	M
P12622	50	M
P723	54	M
P3523	55	M
P3623	52	F

Appendix B . Facile Method for Fabricating Elastomeric Tubes with Internal or External Microtopography

Appendix B.1 Introduction

Many surfaces within the human body are not flat, but instead have a complex surface topography[97]. Familiar examples itself include fingerprints[98], papillae on the tongue[99], and sulci on brain[100]. The inner surface of many conduits within the body are also highly textured, e.g. longitudinal wrinkles on the luminal surface of blood vessels[97, 101], villi on intestines [102], and circumferential wrinkles in anatomical conduits such as trachea[103], intestines[104] and esophagus[105]. Such topography often has biological functions, e.g. increasing mass transport rates due to higher surface area, regulating fluid flow, or permitting expansion without mechanical damage. Looking more broadly beyond human anatomy, textured surfaces are common in biology and include sharkskin riblets that reduce drag [106], cuttlefish or octopus papillae that help camouflage [107-109], or textures that reduce biofouling [37, 110]. These observations have inspired numerous biomimetic approaches that exploit surface topography for specific applications.

Turning to synthetic systems, conduits with luminal or external corrugated surfaces, have a number of potential applications [36, 101, 111]. The corrugations can increase surface area which is useful in increasing transport rates across membranes as observed in biological tissues [112]. Increased surface area also helps in heat dissipation from the tube surface[113, 114]. Surface topography in tubes can also help in regulating fluid flow [114]. Luminal longitudinal wrinkles in vascular conduits lead to a dynamic topography, where the surface topography changes as the

diameter of the conduit changes, which can act as a self-cleaning mechanism to reduce fouling [36, 101].

One challenge for research in this area is the difficulty of fabricating tubes with internal or external topography. Large scale manufacturing operations such as tube extrusion with a corrugated die, or by molding within a textured mold are unsuitable for research purposes due to the need for specialized expertise and equipment. Moreover, achieving features smaller than 100 micron requires complex machining to fabricate the molds and extrusion dies used in such operations. This paper illustrates a rapid prototyping method that can create small-scale topography on the inner or outer surface of elastomeric tubes. Our focus is on applications where the topography must be realized on relatively soft tubes which are capable of expansion. Such tubes are used in research on soft robotics, pneumatic actuators, as well as in our own research on developing vascular grafts with antithrombotic properties.

We take inspiration from prior research that exploits the buckling behavior of multilayered composites[115-121] to develop surface texture. The essential idea is to compress a thin stiff layer that is bonded to the surface of a softer layer. The thin layer then spontaneously buckles to give a highly wrinkled surface. The compression may be applied by various methods: unequal thermal expansion between the stiff and the soft layers [116], unequal swelling of the two layers [122], pre-stretching the softer layer prior to bonding [123], or exploiting plasticity of the stiff layer [124, 125]. In all these cases, the goal is to create a "strain mismatch" such that the thin stiff layer experiences compression, and therefore buckles. This approach has the benefit of creating wrinkled textures with length scale on the order of tens of microns over large surfaces, but without the need of microfabrication methods. Although the essential principle of exploiting the buckling of a substrate-supported thin film to realize surface texture can be applied to any geometry, the

specific fabrication methods developed previously cannot be applied easily to tubes. This is because the common methods of applying the thin film onto the surface of the soft layer (spin-coating, roll-coating, blade coating) are only suitable for flat surfaces and cannot be applied to the inner or outer surface of cylinders. One popular method for realizing a stiff-on-soft structure is to expose a silicone elastomer to UV/Ozone treatment to create a silica-like surface layer [37, 118]. While this method may work for the outer surface of tubes, it is unsuitable for the inner surface. Similarly, deposition of a thin metal film on the surface of an elastomer [116] is also unsuitable for the inner surface of tubes.

This paper shows a method for the fabrication of tubular conduits with an internal luminal or external topography. We retain the idea of exploiting the buckling of a supported thin film but use the method of spraycoating to deposit the thin layer. Spraycoating can allow for coatings as thin as 100-200 nm [126], and such coatings can readily give wrinkles with few micron wavelengths. Thus we retain the central advantage of the buckling approach that small-scale topography can be created without the need of microfabrication. While spraycoating can only be conducted on the outer surface of tubes, we show that elastomeric tubes can be inverted to realize wrinkles along the luminal (i.e. inner) surface. Finally we also show how the same method can be adapted to vary the orientation of the topography.

One further aspect of this paper is to show how soft seamless elastomeric tubes can be made easily. Traditional methods to fabricate tubes require extrusion using special pipe extrusion dies. Here we show a method to rapidly fabricate seamless elastomeric tubes by using readily available metal tubes as molds. This method would prove useful for rapid prototyping of any elastomeric tubes, even when surface topography is not needed.

Appendix B.2 Materials, Methods, and Results

The focus of this study was to develop a method of corrugating the inner surface of a tubular conduit. The same method can be used to corrugate the outer surface as well. Since this latter procedure is simpler and only requires eliminating two steps, we will not discuss it in detail but only show an example later in the paper.

As in previous research, we exploit the wrinkling instability of a thin stiff film bonded to a softer substrate. Prestretching the soft substrate during film deposition creates a strain mismatch between these two layers, thus imposing compression onto the stiff film, which then wrinkles. In our case, the softer substrate is simply an elastomeric tube. The central challenge is to deposit a thin stiff film onto the inner surface of this tube while holding the tube in a prestretched configuration.

The overall fabrication method to develop wrinkles on the inner surface is illustrated in Appendix B Figure. 1. The soft elastomeric tube was first inverted, so as to expose its inner surface, and then mounted onto a cylindrical rod which serves as a mandrel. The material forming the stiff layer was spray coated onto this surface. The coated tube was removed from the mandrel and reinverted so that the surface bearing the stiff film was now the inner surface of the tube. The crucial aspect of the procedure is that a strain mismatch between the tube and the stiff film can be created by suitable choice of the mandrel and mounting method. Specifically, by using a mandrel with a diameter larger than the inner diameter of the soft tube, we created a circumferential strain mismatch. Accordingly, the tubes developed longitudinal wrinkles when removed from the mandrel. If the tubes were mounted onto the mandrel and held with an axial stretch during coating, this led to an axial strain mismatch between the coating and the tube, and hence induced circumferential wrinkles. Introducing a twist to the tube led to helical wrinkles.

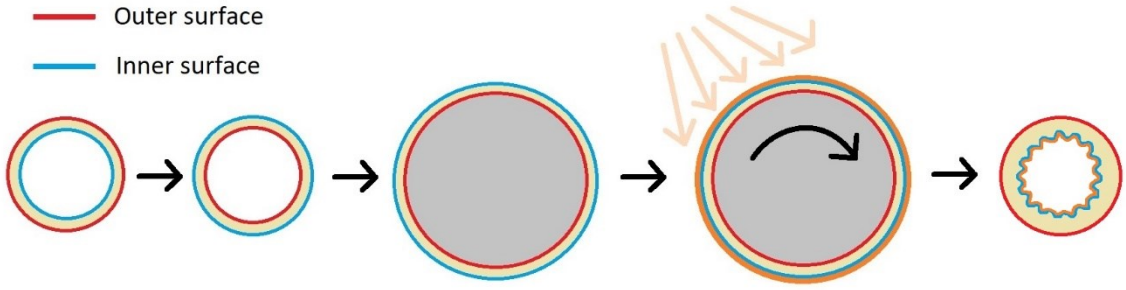

Appendix B Figure. 1 Schematic illustration of process to create inner luminal wrinkles

The above method was developed using the silicone rubber Ecoflex-20 for the soft tube and the silicone rubber Dow Corning M4136 as the stiff layer. Both materials are platinum-curing two-part formulations and have excellent mutual adhesion. Appendix B Figure. 2 shows the elastic stress-strain behavior of the two silicones used in the above study measured using uniaxial tensile test: Ecoflex-20 ($E = 0.042\ MPa$) for the soft tube, and Dow Corning M-4136 ($E = 1.58\ MPa$). Application of the method to other materials will be discussed at the end of this paper.

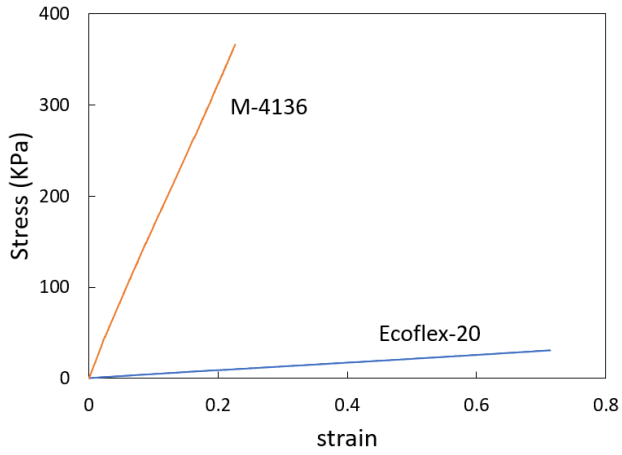

Appendix B Figure. 2 Showing tensile behavior for Ecoflex-20 and Dow Corning M-4136 silicones

Appendix B.2.1 Fabrication of Seamless Soft Tubes

Tubular conduits of inner diameter 4 mm and wall thickness of 1.1 mm were manufactured from soft silicone (Ecoflex-20) by casting in annular molds. These molds comprised a stainless-steel center rod held concentrically within a smooth-walled aluminum tube. In the first step (Appendix B Figure. 3(A)), the rod was held in place by means of 3D-printed endcaps. A gentle vacuum was applied to suck in the uncured Ecoflex-20 into the mold. The endcaps had openings through which the silicone can flow. Once the mold was completely filled as judged by silicone rising into the suction tube, the end caps were replaced with 3-D printed annular inserts which seal off the molds (Appendix B Figure. 3(B)) and the filled tubes were allowed to sit till the silicone cured. Cured silicone tubes along with the center rods were taken out of the aluminum molds, and the tubes were then removed off the mandrel. A few drops of isopropanol were found to facilitate release of the tubes from the rods and from the aluminum tubes. This procedure yielded seamless tubes with uniform wall thickness.

Note that metal rods and tubes that define the annular space that forms the mold are readily available in a wide variety of diameters. Accordingly, the above procedure can be used across a wide range of tube dimensions. Our two-step procedure was developed to avoid trapping air bubbles in the annular cavity, and sucking the uncured silicone into the annular mold completely avoids air bubbles. If a large wall thickness was desired, our two-step procedure may not be necessary; one may directly pour the silicone into the annular cavity and allow any air bubbles to simply rise upwards before the silicone cures.

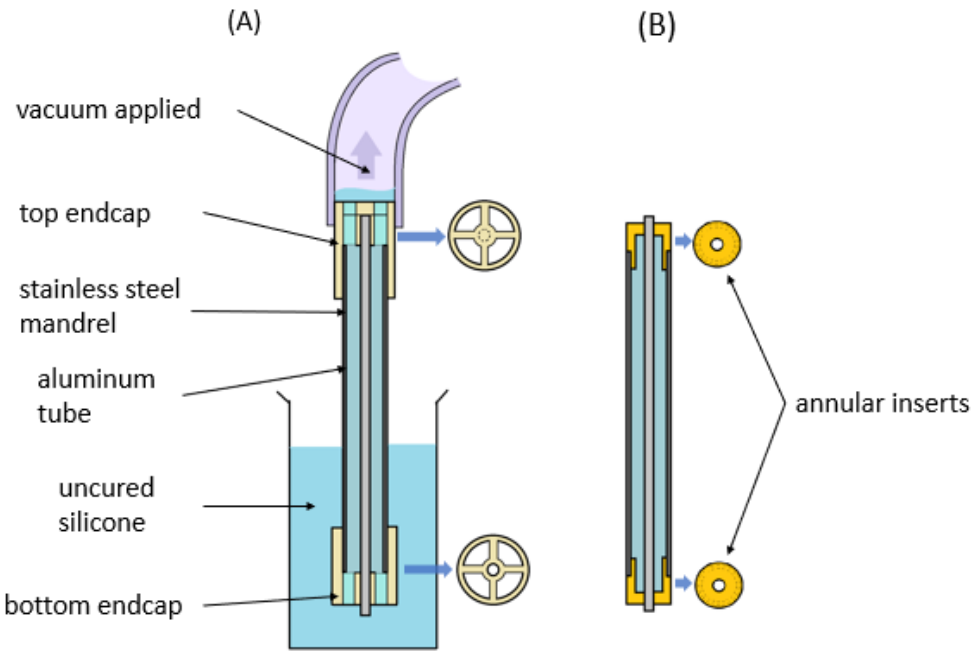

Appendix B Figure. 3 Process of making seamless silicone tubes using annular mold

(A) Custom 3D printed endcaps hold the center rod in place during suction, and (B) The center rod is held concentrically by 3D printed annular inserts during curing

These Ecoflex-20 tubes were then inverted and mounted onto rods (henceforth called "mandrels") of suitable diameter (see Results below) corresponding to the amount and type of prestrain desired, as described in the paragraph above. If the outer surface of a thick-walled tube is coated and then inverted so that it becomes the inner surface, the tube creases and this affects the uniformity of wrinkles developed due to strain mismatch between the sprayed layer and the tube. Hence, pre-inversion of the tube is to obtain uniform wrinkles.

Appendix B.2.2 Spray Coating a Thin Stiff Layer

The stiff silicone M4136 was dissolved in hexane in a 1:1 weight ratio. This ratio was chosen so that the viscosity of the solution was sufficiently low to allow spraying with an airbrush,

which was cleaned with hexane prior to the start of each experiment. The mandrel with tube and the airbrush were then mounted on the spray setup (Appendix B Figure. 4). The spray setup consists of a chuck which holds the mandrel and rotates it at 120 rpm, and a reciprocating carriage which holds the airbrush. The carriage can move up to 35 cm at speeds ranging from 0.2 mm/s to 8 mm/s using stepper motors controlled by an Arduino system. The spray head was located 10 cm away from the rotating mandrel and a constant air pressure of 15 psi was applied to the airbrush during spraying. The coating thickness was varied by varying the speed and number translations of the airbrush during spraying. Coated rods were then placed at 100°C to accelerate curing of the sprayed silicone layer. After the deposited layer was cured, the tubes were reinverted. The design of the spray setup and the Arduino codes controlling the stepper motors can be made available upon request. This method could be used to create wrinkles in longitudinal, circumferential or helical directions depending on the way the prestrain is applied. A larger diameter mandrel provided a circumferential pre-strain and correspondingly led to development of longitudinal wrinkles, pre-stretch in the axial direction led to circumferential wrinkles, while introducing a twist to the tube led to helical wrinkles.

The wrinkle topography was quantified by optical microscopy of cross sections of the wrinkled tubes. The tubes were first cast in a transparent silicone to prevent them from collapsing when cutting their cross sections. Thin slices of the embedded tubes were then cut and imaged to measure thickness of the deposited film, and wavelength and amplitude of the wrinkles. The effect of (i) number of coats on film thickness, (ii) translational speed of airbrush on film thickness, (iii) film thickness on wrinkle wavelength, and (iv) pre-strain on wrinkle amplitude and wrinkle direction were evaluated.

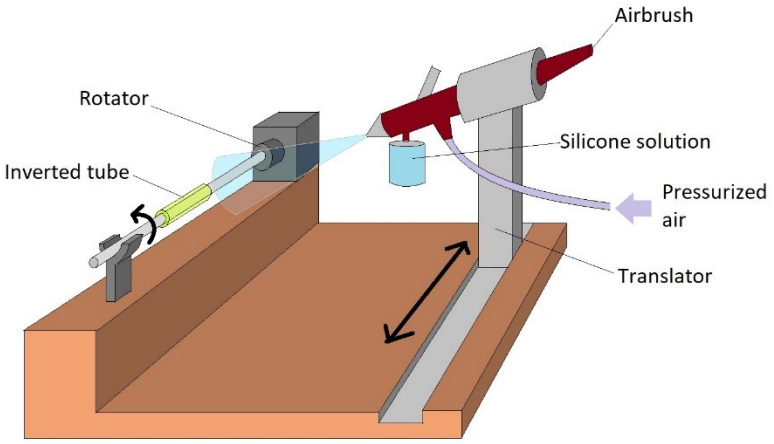

Appendix B Figure. 4 Schematic showing different components of the spray coating setup

Appendix B.2.3 Quantification of Wrinkled Topography

Appendix B Figure. 5 (A) shows the cross-sectional view of a slice of a sample as seen under the microscope. The specific example shown corresponds to mounting the inverted elastomeric tubes on a mandrel of diameter 6.24 mm before spray-coating. Upon reinverting, the image shows a strongly-wrinkled inner surface. We first discuss how the spraying parameters affect the thickness of the coating and the wrinkle morphology. In all cases, spraying successfully deposited a uniformly-thick coating whose thickness increased with number of coats, where each coat corresponded to one translation of the airbrush mounted on the translator. A slower translation speed caused more deposition per unit area of the tube and thus, slower speed corresponded to a thicker coating (Appendix B Figure. 5 (B)).

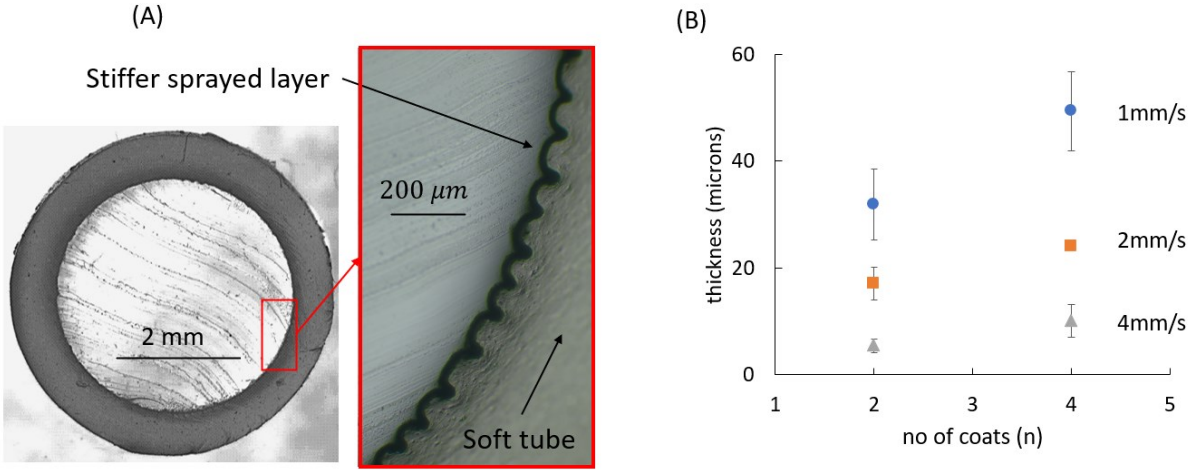

Appendix B Figure. 5 Wrinkle-lumen tube and coating thickness

(A) Cross-section of the reinverted tube with a magnified microscope image of the wrinkles, and (B) Film thickness measured for different translator speeds and number of coats

With increasing thickness of the spray-coated film, the wrinkle morphology also changed in tandem. Appendix B Figure. 6 (A) shows that the wavelength and amplitude increase almost proportionately with the thickness. The wavelengths may be compared against the theory of wrinkling of a stiff elastic film bonded to a thick soft substrate[127] which predicts

$$\lambda = 2\pi h \left(\frac{E_f (1-\nu_s)^2}{E_s (1-\nu_f)^2} \right)^{\frac{1}{3}} \tag{B1}$$

For fixed material properties, the wavelength of the wrinkles is predicted to increase proportionately with the thickness of the film. This is indeed seen in Appendix B Figure. 6 (A) for the same samples as from Appendix B Figure. 5 (B). For the values of E_f and E_s measured experimentally, the modulus ratio is roughly 38 and hence the above equation predicts $\lambda = 14.5h$. This is roughly two-fold larger than the slope of the λ vs h data in Appendix B Figure. 6 (A). A portion of this discrepancy may be the effect of prestretch; The above Eq. B1 was derived for the compression of a stiff film on a soft substrate where both layers are initially stress-free. In contrast,

here the soft elastomeric layer is prestretched which is expected to reduce the wavelength [128]. The amount of prestretch can be estimated as follows. The inner radius of the fabricated tube is 2mm. Upon inversion, and then placing onto the mandrel, this inner surface is stretched to a radius of 3.92mm. This latter value is a sum of the mandrel radius (3.12mm) and wall thickness calculated after taking into account the stretch and Poisson's ratio (t = 0.8mm). The ratio of the stretched surface to the original deformed surface is 1.96. For this value, the expectation based on accordion mechanics is roughly 69.5% decrease in wavelength [128].

The results of Appendix B Figure. 5 (B) and Appendix B Figure. 6 (A) were all obtained by placing the inverted tubes onto mandrels of diameter 6.24 mm. A separate set of experiments was conducted varying the mandrel diameter, and hence the circumferential strain mismatch at two different film thicknesses. The wrinkle wavelength was found to decrease with increasing mandrel diameter, once again in agreement with the expectation that prestretch should decrease wavelength. This was done for two different coatings (2 coats at 1mm/s and 6 coats at 1mm/s). The larger strain, and correspondingly larger coating layer was accommodated by a combination of increasing wrinkle amplitude and decreasing wrinkle wavelength (Appendix B Figure. 6 (B)).

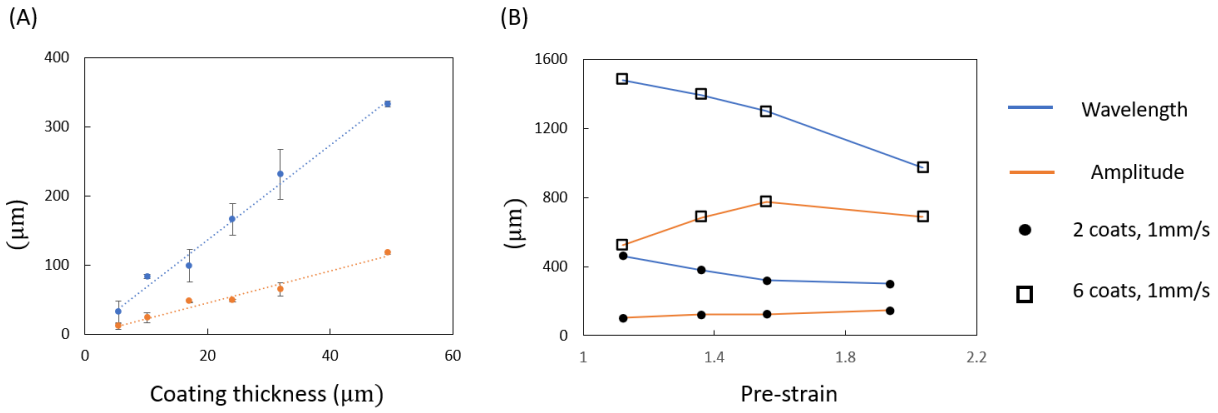

Appendix B Figure. 6 Effect of thickness and prestrain

Dependance of wrinkle wavelength (blue) and amplitude (orange) on (A) film thickness and (B) amount of pre-strain for thicker coating (squares) and thinner coating (solid circles)

Having established the basic method of achieving wrinkled topography inside a cylindrical tube, we will now illustrate several variations that alter the structure of the wrinkles. These were done with relatively large coating thicknesses (~120-150 μm) for ease of imaging. Appendix B Figure. 7 (A) illustrates a sample prepared using the same approach as Appendix B Figure. 5 and Appendix B Figure. 6, viz. placing the inverted tube onto a large diameter mandrel prior to spray coating, followed by re-inversion. The same method can be applied – much more easily – to realize tubes with wrinkles on their outer surface (Appendix B Figure. 7 (B)). In this case, inversion and re-inversion is not needed; the soft tube was directly placed onto a larger diameter mandrel.

Instead of imposing a circumferential strain mismatch using a larger diameter mandrel, we may instead impose an axial mismatch by simply fixing the tube in an elongated state onto the mandrel. In this case, since the film experiences compression along its inner surface, circumferentially-oriented wrinkles are expected. The upper image in Appendix B Figure. 7 (C) shows an example of this situation realized by inverting a tube onto a mandrel of diameter 4mm and holding it elongated by a factor of 2 during coating. In a similar manner, fixing the tube in a twisted configuration prior to spray-coating can give helical wrinkles (lower image in Appendix B Figure. 7 (C)). In this case, a twist of $360°$ was applied over a 3 cm long segment of tube. Finally, applying a combined axial and circumferential pre-strain induced a more complex pattern of wrinkles (Appendix B Figure. 7 (D and E)).

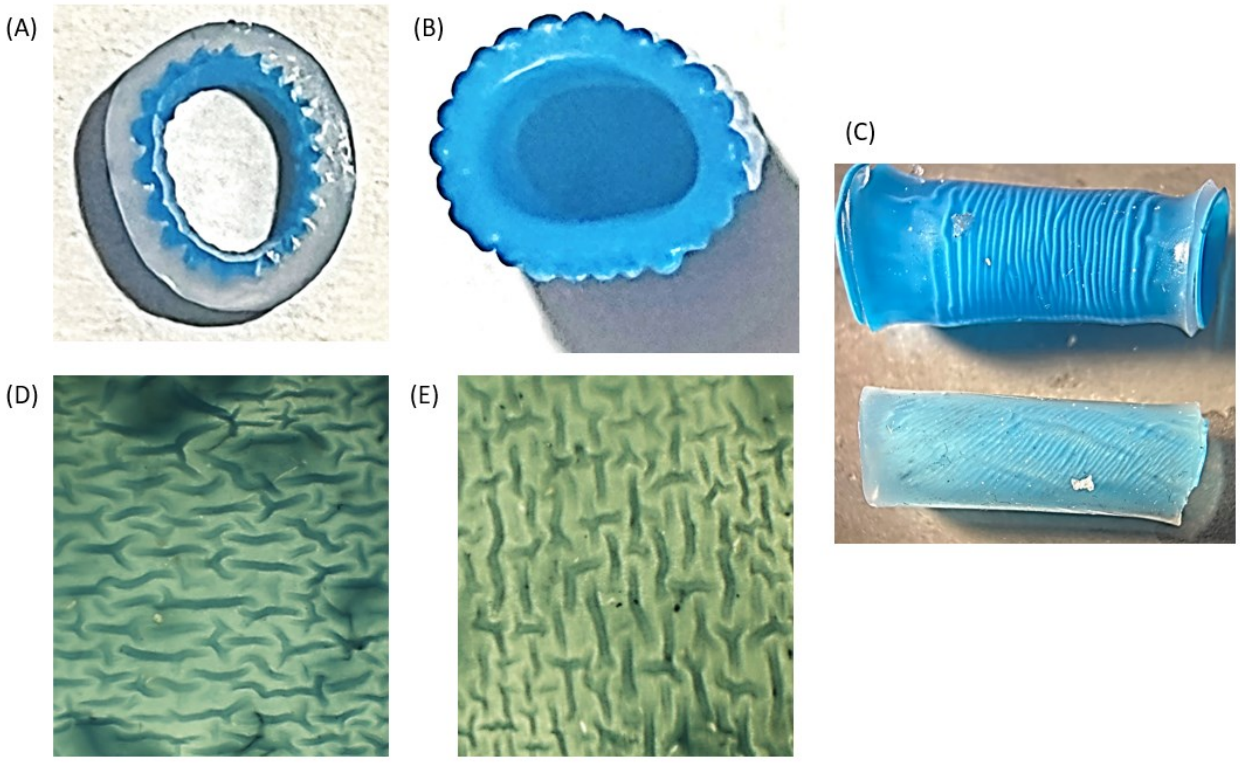

Appendix B Figure. 7 Tubes with different types of surface topographieses

Cross sections of tubes with (A) internal longitudinal wrinkles ($\varepsilon_{circ} = 1.54$), (B) external longitudinal wrinkles ($\varepsilon_{circ} = 1.54$); Tubes with (C) circumferential wrinkles ($\varepsilon_{axial} = 1$) (top) and helical wrinkles($\varepsilon_{twist} = 360° \; over \; 3 \; cm$) (bottom) visible through the tube walls; and (D) ($\varepsilon_{circ} = 1.54, \varepsilon_{axial} = 1$) and (E) ($\varepsilon_{circ} = 0.96, \varepsilon_{axial} = 1$): Through-wall microscope images of patterned wrinkles formed using combinations of different directional pre-strains

Appendix B.3 Discussion

We will now discuss some essential material considerations in applying this fabrication method, possible variations of the method, and the limitations in extending it more broadly. One key requirement is that the tube and the coated layer must have a large difference in modulus; this is a requirement for all the buckling-based methods of developing topography. A second key point

is that realizing wrinkles on the internal surface requires inverting and then reinverting elastomeric tubes. Thus, it is crucial that the elastomeric tubes be sufficiently stretchy to permit inversion. Many silicone elastomers, natural rubber, and various synthetic rubber tubes do have sufficient stretchability to permit inversion. A third requirement is that the two layers must have excellent adhesion so that they remain bonded during inversion. These latter two requirements are less relevant if wrinkles are desired on the external surface; inversion is not needed, and further, due to the smaller strains experienced, the film may be expected to remain bonded even with modest adhesion. Thus, situations with outer wrinkles may be implemented with a much wider range of materials.

We have used a simple pressure-driven spray as a coating method to create the thin stiff film on the surface. While simple and inexpensive, it requires diligent cleaning (in our case, by spraying several mL of hexane after each experiment) to prevent clogging. However, alternate methods such as electrospraying or electrodeposition may also be used, especially if very thin coatings are desired. Dipcoating is also viable, but with the crucial limitation that the elastomeric tube must be chemically incompatible with the solvent. This is because dipcoating requires the tube to remain immersed into the solvent for extended periods, and a solvent that has good compatibility with the elastomeric tube would induce large degree of swelling. This is especially true if thin coatings are desired, which require very slow dipcoating. Indeed, in our own case, dipcoating the stiff layer onto the tube using hexane as a solvent would not be viable due to severe swelling. One benefit of spraying is that the solvent can evaporate rapidly, and hence significant swelling can be avoided.

Other ways to coat the inner surface of tubular conduits include methods such as plasma sputtering[129], improvised spray-coating[130], plasma immersion[131], vapor deposition.

However, in these methods, it is difficult to induce a pre-strain to the tubes, which is necessary to develop topography using bilayer strain-mismatch.

Finally we contrast this paper against the approach taken in our own past research. In that case, a thin stiff layer is first dipcoated onto a large diameter mandrel, coated with a soft adhesive, and then inserted into a smaller-diameter soft tube as done in the study by Nath et al. [36]. Note that the soft tube must expand to accommodate the larger mandrel, thus inducing strain mismatch between the stiff layer and the tube. Upon curing the adhesive, the coated layer becomes strongly bonded to the inner surface of the tube. Upon removal of this now-bilayered tube from the mandrel, wrinkles appear as the soft tube shrinks in diameter. The central challenge of that approach is that the stiff film can undergo significant damage or even delaminate from the mandrel when inserting the mandrel into the soft tube.

Appendix B.4 Conclusion

To summarize, we have developed a method of fabricating soft elastomeric tubes with surface topography without the need of large-scale microfabrication. We have illustrated methods useful in various areas of research: (1) a method to create long, thin-walled silicone cylindrical tubes by using the annular space between a tube and a rod; (2) a spraycoating method to apply a thin coating onto a cylindrical surface with the desired strain mismatch, and (3) the idea of inverting the tubes before coating so that wrinkles can be developed on the inner surface of the tubes. All three methods are inexpensive, require little equipment, and can be used across a range of geometries making them suitable for rapid prototyping. This method can be used to create topography of a range of scale depending on the stiff layer thickness and applied pre-strain. Small

variations of the method allow the orientation surface topography to be varied, e.g. the wrinkles being oriented circumferentially or axially, or on the outer surface of the tubes. Tubes made by this method are well-suited for research on applications such as synthetic tubular prosthetics for replacing biological conduits, or conduits that resist fouling by a purely mechanical means.

Appendix C : Amplitude Variation and Fiber Strain for Single Embedded Crimped Fiber and Experimental Verification

Appendix C.1 Introduction

Stiffer fibers embedded in softer matrix provide reinforcement and stiffness to the composites. Using short fibers as reinforcement fillers gives the advantage of being able to fabricate the composites using conventional plastics processing operations such as extrusion, molding, and extrusion-based 3D printing [57, 75-80]. Compared to stiffer straight fibers, stiffer crimped fibers behave differently when embedded in a soft matrix. As the matrix is stretched, the crimped fibers initially uncrimp before developing a strain. This leads to strain hardening behavior of the composite, since crimped fibers as fillers act as softer reinforcers at lower strains and provide higher stiffness to the composite at higher strains.

Stress transfer occurring between the matrix and the fiber for a finite length straight fiber was shown by Cox's Shear Lag Theory [86]. According to this model, there is a certain length near the ends of the straight fiber that does not bear full load, whereas the middle portion of the fiber is fully loaded. This length (termed as 'shear lag length (l_s)') is dependent on the fiber modulus and the fiber aspect ratio. Calculation of l_s helps us estimate length of the fiber which does not contribute completely towards composite stiffness and thus helps us decide the minimum fiber length for such short fiber composites. This study had not been done for when the fiber is initially crimped.

In our previous study, we quantified the stress transfer occurring between the matrix and the fiber for a single finite length crimped fiber [38]. It was found that similar to a straight fiber,

there is an analogous length near the ends of the crimped fiber where the stress is lower than the fully loaded middle region of the fiber, which was termed as the 'effective shear lag length (l_s^{eff})'. In contrast to straight fiber behavior, l_s^{eff} is not constant for the crimped fiber, but increases with increase in applied strain. This is in tandem with the assumption that the fiber uncrimps at lower strains and as it uncrimps, its geometry gets closer to that of a straight fiber correspondingly increasing the resistance of the fiber to further stretch. This effective shear lag length for a crimped fiber is not only dependent on the applied strain but also on the relative stiffness of the fiber (as in the case of straight fibers) and the degree of crimp of the fiber. The degree of crimp can then quantified by the initial amplitude of crimps for the fiber. Since this portion of the fiber near the ends is not fully loaded, we can infer that this portion will not uncrimp as much as the fully loaded region. In order to determine the l_s^{eff}, we proposed an Equivalent Straight Fiber model as a modified form of the Cox's Shear Lag Model, which approximated a crimped fiber to an equivalent straight fiber whose modulus increases with strain.

In order to estimate the fraction of fiber length contributing towards reinforcement, the l_s^{eff} needs to be calculated for the crimped fiber from the fiber stress and strain. Although, the values of fiber stress and strain are possible to obtain from computational simulations, these values are difficult to measure in a physical system. In a physical setup, fiber stress cannot be directly measured but needs to be calculated from fiber strain. Markers can be placed upon the fiber and these markers can be tracked as the matrix is stretched to calculate the strain. However, this requires the markers to be on the scale of the fiber width, and presents difficulty when dealing with fibers of micron-scale diameters. In such a physical setup, however, it is still possible to directly observe the fiber profile using a camera.

This study is a follow up of the previous single crimped fiber simulation study, where our goal is to investigate whether the fraction of fiber which contributes towards composite stiffness can be quantified by observing only the fiber profile at different applied strains to the matrix. Since the crimped fiber does not fully uncrimp where there is no complete fiber loading, we suggest looking at the reduction in peak amplitudes along the fiber. This analysis is first carried out on the same set of simulations that were presented in the previous study [38]. We then provide an experimental verification of this method wherein samples were created with a single embedded crimped fiber in a softer matrix. Similar analysis was done by tracking the peaks and troughs of the crimped fiber in the experimental samples in order to find out the fraction of the fiber that uncrimps.

Appendix C.2 Methods

Appendix C.2.1 Uniaxial Stretching of Single Fiber Samples

Samples were made with a single crimped fiber embedded in the central plane of a relatively softer matrix. The samples were made in lab using 100% polyester thread filaments of diameter 15-20 μm, and Sylgard 184 silicone as the surrounding matrix. Specialized set up was used for crimping the threads and embedding them into the silicone (Appendix C Figure. 1).

The crimping setup consisted of a silicone mold with groves of wavelength 400 microns (Appendix C Figure. 1 (A)). This corresponded to the crimped threads having a wavelength which was 40-50 times the fiber radius. This ratio is similar to that for the fiber modelled in simulations in the single fiber computational study [38]. The silicone mold had gutters connected to the groves

with an outlet for vacuum. A grooved blanket with interlocking grooves was placed on top, sandwiching the threads which were laid out on the base perpendicular to the direction of grooves. Vacuum was applied in order to secure the blanket to the base mold and the entire set up was then gradually heated to 200° C. This temperature did not cause the fibers to melt but was enough to soften them in order to allow the grooves to form the fibers using plastic deformation. After a short period of time (~4 minutes), the setup was rapidly cooled by immersing in an ice bath while still applying the vacuum. Once cooled and the vacuum turned off, the grooved blanket was removed and the fibers were gently removed from the grooved base, thus retaining their crimped geometry. Appendix C Figure. 1 (C) shows the resulted crimped fibers.

The crimped fibers were cut to a length of 4 mm ensuring that there were 8-10 wavelengths in the fiber length. These threads were then plasma treated for better adhesion to the silicone and placed on thin flat silicone (Sylgard 184) slabs. An equal amount of the same silicone was then poured on top, thus embedding the threads in the central plane. The samples were allowed to cure for sufficient time before placing in the uniaxial tensile setup and were then stretched to a strain of 20-25%. Images of the fibers were taken at multiple strains using a mounted camera for image analysis (Appendix C Figure. 1 (B)).

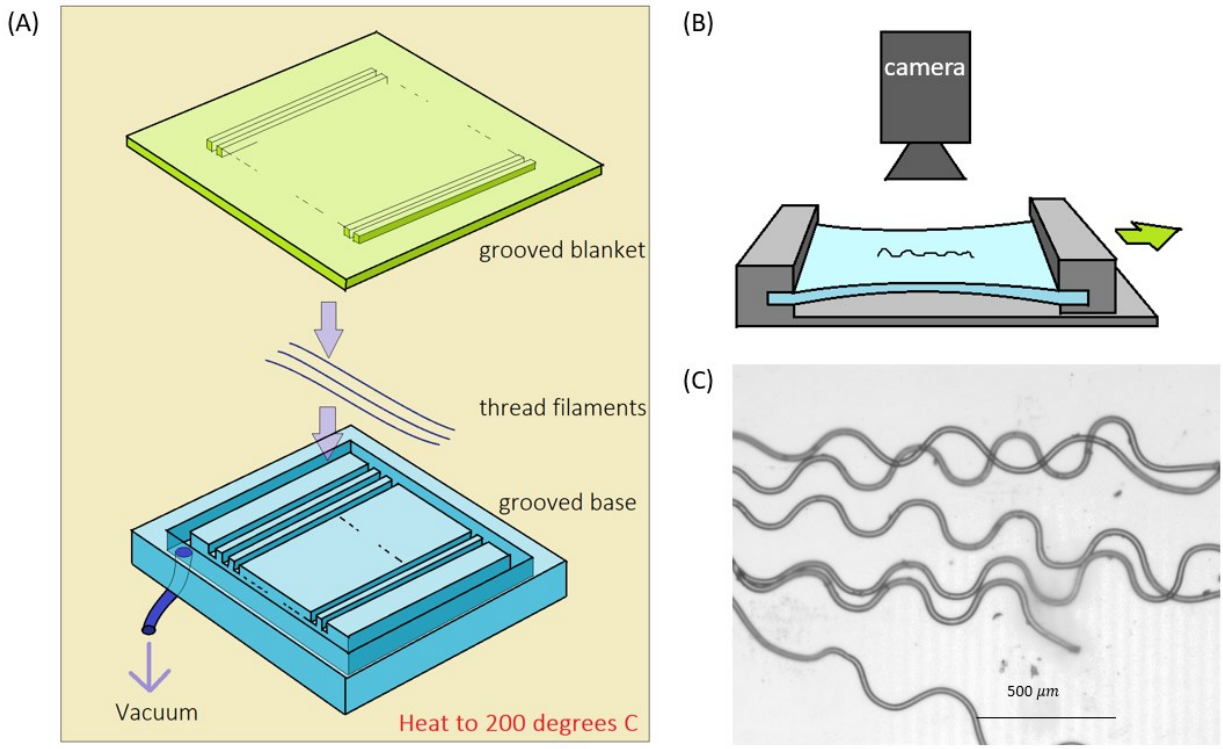

Appendix C Figure. 1 Fiber crimping setup

(A) Cartoon schematic of thread crimping setup, (B) Cartoon schematic of tensile stretch setup, and (C) resulting crimped fiber filaments

Appendix C.2.2 Image Analysis

Analysis was carried out for both the single fiber simulations from the previous study, and for the experimental samples. To obtain the fiber profile at different strains, XY coordinates of the fiber were output from the single fiber simulations. For the single fiber experimental samples, images of the fiber inside the matrix were captured at discrete values of applied strain as the matrix was stretched. Analysis of these images was done using ImageJ and Matlab softwares. Images of fibers taken with the camera (Appendix C Figure. 2 (A – top)) were converted to binary format and the fiber profile was isolated (Appendix C Figure. 2 (A – middle)). The central axis of the

fiber was mapped to straight line, in order to eliminate errors due to gross-scale bending of the fiber (Appendix C Figure. 2 (A – bottom)). Appendix C Figure. 3 shows the fiber profiles at different strains for (A) single fiber simulation, and (B) single fiber experimental sample. Here, we see that as the matrix is stretched, the fiber does not stretch uniformly. There is a variation in the crimp amplitudes (A_c) along the fiber. The dotted lines in Appendix C Figure. 3 show qualitatively that the amplitude reduces more for peaks in the middle region of the fiber as compared to the peaks near the ends. The Y-axis on the plots in Appendix C Figure. 3 (A and B) is magnified in order to emphasize the variation in the amplitudes seen along the fiber. Thus we can define a certain "penetration length" for the amplitude (l_{p_A}) which is the length of the fiber near the ends where the peak amplitude is not maximally reduced. This length can be found out by calculating the reduction in crimp amplitude for the peaks along the fiber at different strains.

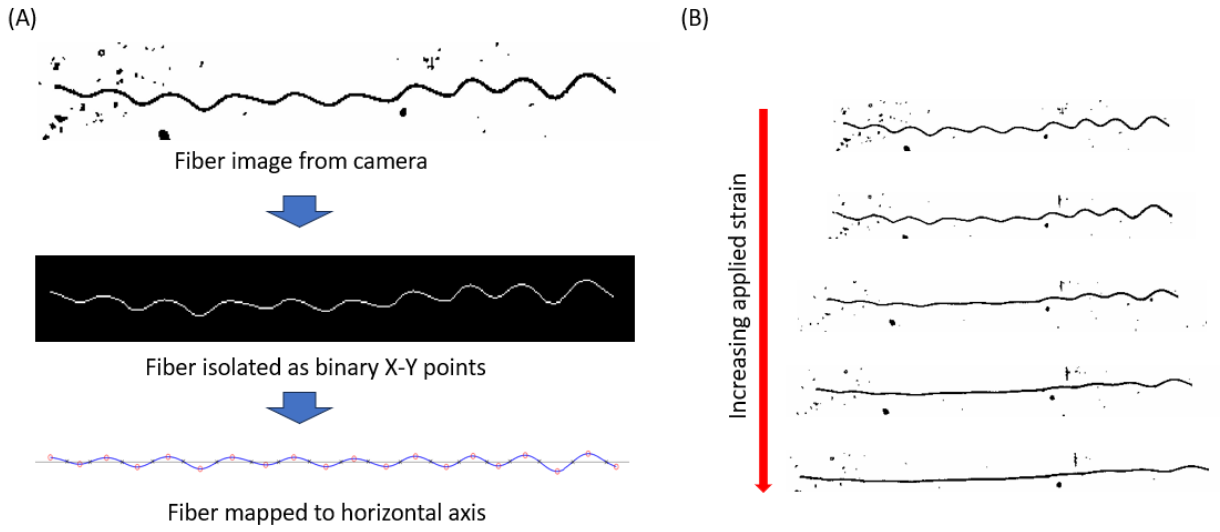

Appendix C Figure. 2 Image analysis of single fiber sample

(A) Image analysis process showing (top to bottom): camera image of single fiber sample, binary isolation of fiber profile, and plotted fiber profile with mapped peaks (red circles) and half-wavelength points (black stars), and (B) camera images of fiber profile with increasing applied strain (top to bottom)

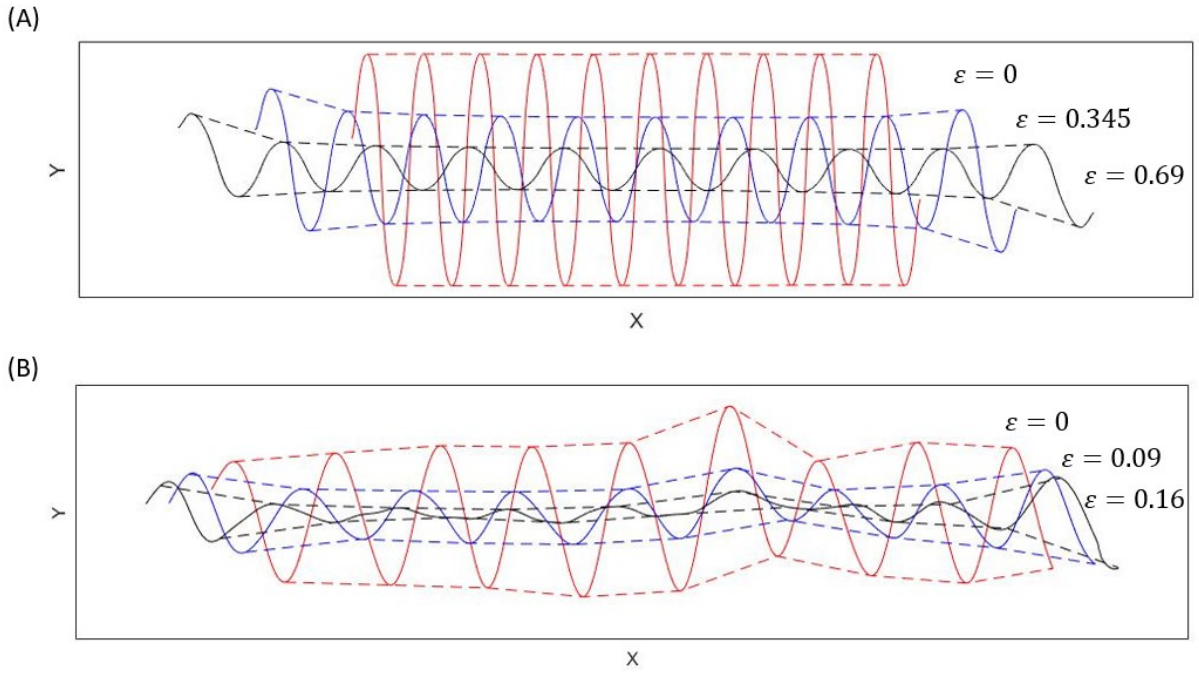

Appendix C Figure. 3 Single fiber profile under stretch

fiber profile at 3 different strains for (A) single fiber simulations $\left(\frac{E_f}{E_m} = 1000, \frac{A_{c_0}}{\lambda} = 0.19\right)$, and (B) single fiber experimental sample $\left(\frac{E_f}{E_m} = \#\#, \frac{A_{c_0}}{\lambda} = 0.08\right)$

In order to get the reduction in crimp amplitude, the peaks and troughs of the fiber profiles were calculated both for the simulations and from the camera images. These are shown as red circles in fig 2C for experimental sample. Amplitude was calculated as the distance of the peak from the central axis of the fiber and the reduction in crimp amplitude was calculated as $A_{red_i} = \left|\frac{A_{c_{0,i}} - A_{c_i}}{A_{c_{0,i}}}\right|_{\varepsilon}$, where A_{c_0} refers to the crimp amplitude of the unstretched fiber ($\varepsilon = 0$), and i refers to the i^{th} peak. For a total of 'n' peaks ($i = 1,2, \dots, n$), the plot of A_{red} vs i resembles the shape of the plot for fiber stress as given by the Shear Lag Model. Thus, in order to find l_{p_A}, an equation similar to the shear lag model was fitted to these plots. Since the shear lag model works for a range $x = \{-L, L\}$, where L is the half length of the fiber and the origin is situated at the center of the

fiber, the origin of $A_{red}\ vs\ i$ plots was also shifted to the midpoint of the fiber $\left(origin = \frac{n+1}{2}\right)$. Thus, the first peak ($i = 1$) now became $-\left(\frac{n-1}{2}\right)$ and the n^{th} peak became $\left(\frac{n-1}{2}\right)$. Eq. C1 was then fitted for the range $x = \left\{-\left(\frac{n-1}{2}\right), \left(\frac{n-1}{2}\right)\right\}$.

$$A_{red} = A_{max}\varepsilon \left(1 - \cosh\left(\frac{3x}{l_{p_A}}\right)\right)\left(\text{sech}\left(\frac{3\left(\frac{n-1}{2}\right)}{l_{p_A}}\right)\right) \tag{C1}$$

In Eq. C1, the quantity ($A_{max}\varepsilon$) is the maximum reduction in amplitude seen at the middle of the fiber, and A_{max} and l_{p_A} are the two fitting parameters. The points where the fiber profile intersects with the central axis of the fibers (inflection points) were also tracked (shown as stars in Appendix C Figure. 2 (A – bottom)). Average strain in the fiber was predicted by calculating the quarter-wavelength distances between the peaks and inflection points. Variation in amplitude along the fiber, changes in l_{p_A} with strain and the average strain in the fiber were compared in this study, for a single fiber simulation and single fiber experimental sample.

Appendix C.3 Results

Appendix C.3.1 Amplitude Variation along the Fiber

Amplitude reduction for the peaks along the fiber were calculated for 2 sets of simulations: i) comparing different relative modulus of fiber: matrix $\left(\frac{E_f}{E_m} = 10, 100 \text{ and } 1000\right)$ for initial crimp amplitude, $\frac{A_{c_0}}{\lambda} = 0.19$, and ii) comparing fibers with different initial crimp amplitudes

$\left(\frac{A_{c_0}}{\lambda} = 0.14, 0.19\ and\ 0.25\right)$ for $\frac{E_f}{E_m} = 1000$. The reduction in amplitude along the fiber was plotted against the peak number ($i = 1, \dots, n$). Appendix C Figure. 4 (A) shows the reduction in amplitude for the peaks along the fiber for a single fiber simulation with $\frac{E_f}{E_m} = 1000$ and $\frac{A_{c_0}}{\lambda} = 0.19$. However in order to get the l_{p_A}, we need to look at the A_{red} in the middle of the fiber relative to the A_{red} at the ends of the fiber. Thus, the relative difference between values of A_{red} at the center and the fiber end $\left(A_{red_i} - A_{red_1}\right)$ was considered for fitting to Eq. C1. These values along with the fits of Eq. C1 are shown in Appendix C Figure. 4 (B). Appendix C Figure. 5 shows the l_{p_A} normalized by the half range of peaks $\left(\frac{n-1}{2}\right)$, so that $l_{p_A}/\left(\frac{n-1}{2}\right)$ represents the fraction of the fiber length where the peaks are not maximally reduced. Lower the value of $l_{p_A}/\left(\frac{n-1}{2}\right)$, larger fraction of the fiber and correspondingly more number of peaks have maximal amplitude reduction. Appendix C Figure. 5 (A) shows the change in $l_{p_A}/\left(\frac{n-1}{2}\right)$ with strain for different fiber: matrix modulus ratios. We see that as the fiber becomes relatively stiffer than the matrix, the value of $l_{p_A}/\left(\frac{n-1}{2}\right)$ also increases, which means that there is a larger fraction of fiber that has lesser reduction in amplitude near the ends and hence, a larger fraction of the fiber that does not 'uncrimp' as much as that in the middle. Appendix C Figure. 5 (B) shows the change in $l_{p_A}/\left(\frac{n-1}{2}\right)$ with strain for different initial crimp amplitudes. We see that the l_{p_A} initially increases with increasing strain and then decreases. The vertical lines correspond to "geometric straightening" and are calculated as the strain needed so that the end-to-end length of the uncrimped fibers becomes equal to the contour length of the original crimped fiber, or in other words, the strain at which the fiber completely straightens out. It is seen that the largest value of l_{p_A} is when the applied strain is close to the strain required for geometric straightening. This means that initially, there is a larger part of

the fiber in the middle that has uniform maximal amplitude reduction. As the strain increases, there are lesser number of peaks which have maximal amplitude reduction. However, once the applied strain increases beyond the strain required for geometric straightening, the number of peaks with maximal reduction increases, thus showing that beyond this strain, uncrimping of the fiber propagates from the middle of the fiber outward towards the ends.

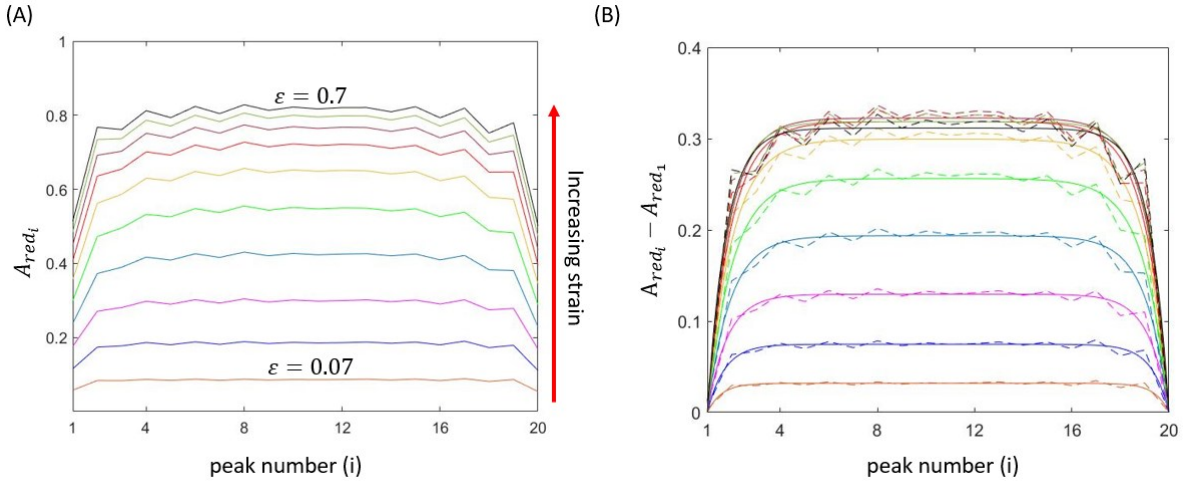

Appendix C Figure. 4 Reduction in crimp amplitude: simulations

(A) reduction in amplitude, and (B) reduction in amplitude relative to end peak with Eq.1 fits; for single fiber simulation $\left(\frac{E_f}{E_m} = 1000, \frac{A_{c_0}}{\lambda} = 0.19\right)$

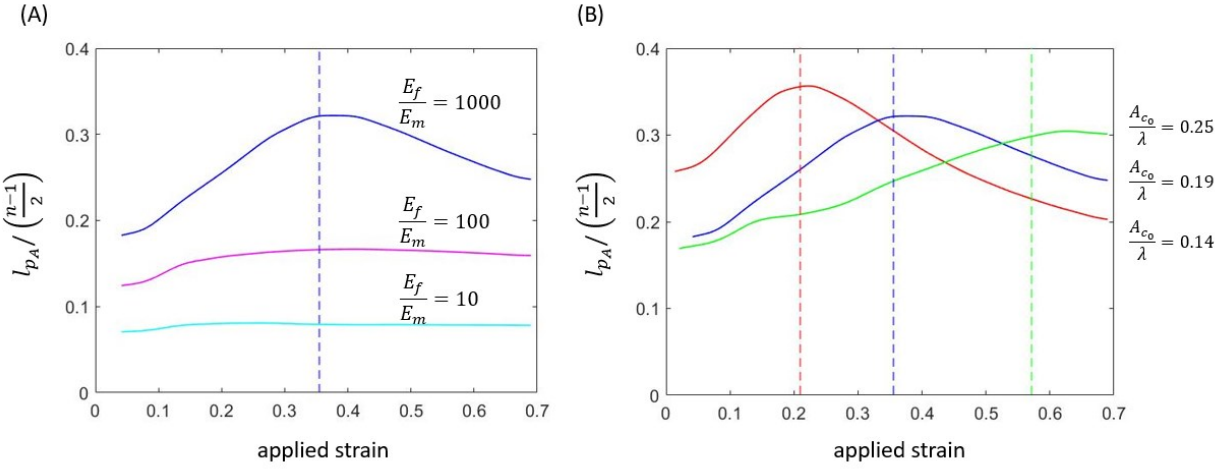

Appendix C Figure. 5 Amplitude penetration length: simulations

Amplitude penetration length (l_{p_A}) vs strain for single fiber simulation for fiber with (A) different relative modulus ratios, and (B) different initial crimp amplitude

Similar analysis to that done for fiber profiles obtained from simulations was performed on the images captured for the single fiber experimental samples. Whereas the simulations can output a very large number of XY points for the fiber profile, the experimental images are limited by the limitations in image tracking and camera resolution. Hence the points were interpolated in order to achieve higher accuracy for finding peaks and half-wavelength points. Due to these limitations, experimental analysis results have a larger variation than the simulations. A total of 3 samples were made and tested. Results for one of the sample are presented here. Since each sample was made separately, they were not exactly alike, although the results for all the samples qualitatively matched. Appendix C Figure. 6 (A) shows the amplitude reduction for a polyester fiber $\left(\frac{E_f}{E_m} \sim 500 \text{ and } \frac{\mathrm{A_{c_0}}}{\lambda} = 0.08\right)$, and Appendix C Figure. 6 (B) shows the reduction in amplitude relative to the amplitude reduction at the ends of the fiber along with fits of Eq. C1. Qualitatively, it is evident from these plots that there is a lower reduction in the amplitude near the ends similar to that observed in simulations. Plotting $l_{p_A} / \left(\frac{n-1}{2}\right)$ with applied strain also shows a similar trend to that observed in simulations, where the l_{p_A} initially increases with strain and then beyond a certain value of strain, starts decreasing, meaning that the propagation of uncrimping is outward from the middle beyond this strain (Appendix C Figure. 7).

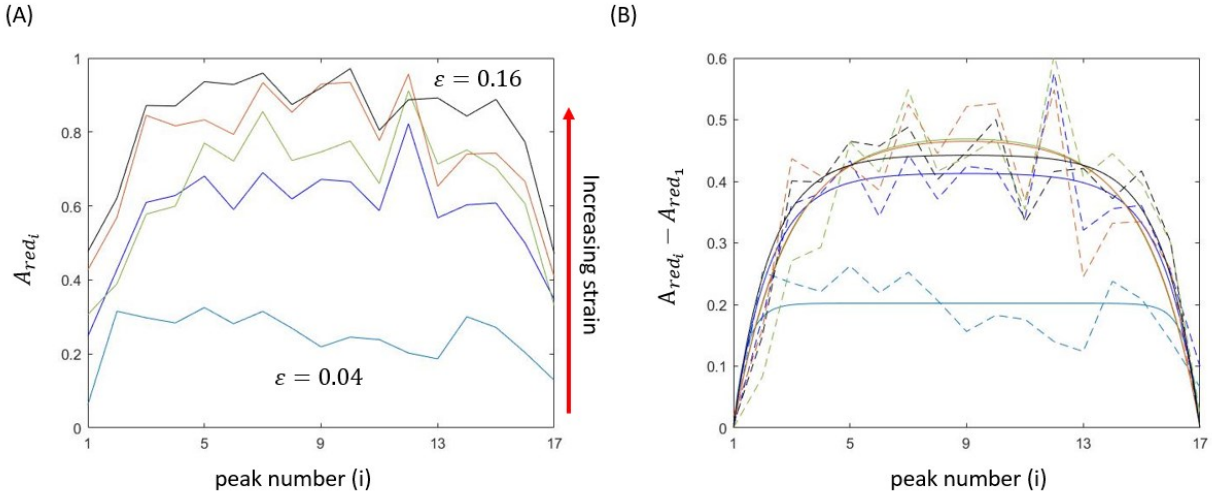

Appendix C Figure. 6 Reduction in crimp amplitude: experiments

(A) reduction in amplitude, and (B) reduction in amplitude relative to end peak with Eq.1 fits; for single fiber simulation $\left(\frac{E_f}{E_m} \sim 500, \frac{A_{c_0}}{\lambda} = 0.08\right)$

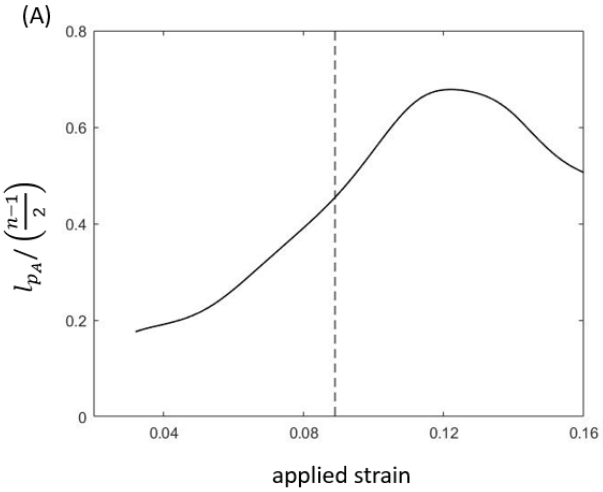

Appendix C Figure. 7 Amplitude penetration length: experiments

Amplitude penetration length (l_{p_A}) vs strain for single fiber experimental sample $\left(\frac{E_f}{E_m} \sim 500, \frac{A_{c_0}}{\lambda} = 0.08\right)$

Appendix C.3.2 Average Strain in the Fiber

Average strain in the fiber was calculated from the fiber contour length (CL) of the fiber, calculated from the fiber profile. Average fiber strain was calculated as:

$$\varepsilon_{f_{mean}} = \frac{CL_\varepsilon - CL_0}{CL_0}$$

Where the subscript indicates the applied strain to the matrix. This is plotted in Appendix C Figure. 8 for single fiber simulations and the 3 single fiber experimental samples. We can see in the plots that the mean fiber strain is lower than the applied strain. This can be attributed to the crimped nature of the fiber.

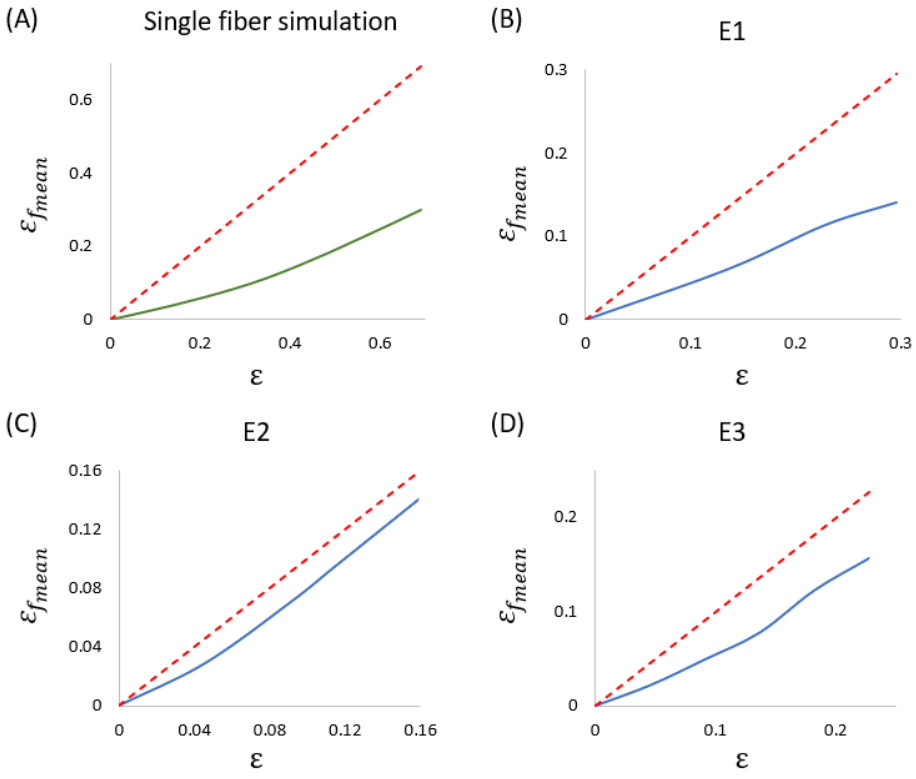

Appendix C Figure. 8 Mean fiber strain

Showing $\varepsilon_{f_{mean}}$ (solid lines) with $y = x$ line (red dashed) for (A) single fiber simulation, and (B to D) experimental samples (E1, E2, E3)

Appendix C.4 Discussion

In multifiber composites, quantifying the fraction of fiber length contributing to reinforcement of the composite is useful in deciding the minimum length of the fibers. Here, we quantify it for crimped fibers, by looking at the reduction in fiber crimp amplitudes which are calculated simply by imaging the fiber and looking at the fiber profile under different applied strains. This study shows that the fraction of fiber that uncrimps and the strain in fiber can both be calculated only from the fiber profile. This method of quantifying the fiber fraction contributing to reinforcement simply by imaging the fiber profile at different strains could be useful in assessing the fiber contribution of chopped crimped fiber to the composite without the need of computational simulations.

There are certain constraints and limitations of using this method of making single crimped fiber samples and imaging the fiber profile to obtain the l_{p_A} and fiber strain. Since the fibers are very small, handling them is difficult and thus the process of making the sample is prone to manual errors. While crimping the fibers, they need to lie exactly perpendicular to the groves of the vacuum forming mold in order to get the exact desired amplitude:wavelength ratio. Fibers that are not lying perpendicular or fibers with a gross bending might not get uniformly crimped. While the crimped fiber is laid on the silicone slab and equal amount of silicone is poured on top to ensure the fiber is central to the sample, there is little control to maintain the fiber in the central plane, and it can change the configuration slightly until the newly poured silicone cures. In order to get good images of very small fibers embedded in the matrix, the fiber needs to be in the plane perpendicular to the camera axis and in the plane of the stretch. Camera resolution needs to be sufficiently good and the matrix material needs to be transparent in order to allow through-depth imaging.

Bibliography

1. Bank, A.J., et al., Contribution of collagen, elastin, and smooth muscle to in vivo human brachial artery wall stress and elastic modulus. Circulation, 1996. 94(12): p. 3263-70.

2. Bibi S. van Thiel, I.v.d.P., Roland Kanaar, A.H. Jan Danser, Jeroen Essers, Structure and cell biology of the vessel wall, in The ESC Textbook of Vascular Biology, a.M.B. Robert Krams, Editor. 2017. p. 5-16.

3. Chow, M.J., et al., Arterial extracellular matrix: a mechanobiological study of the contributions and interactions of elastin and collagen. Biophys J, 2014. 106(12): p. 2684-92.

4. Markus Hecker, D.J.D., Vascular Mechanobiology in Physiology and Disease. Vol. 8. 2021.

5. PB, D., Mechanical properties of arteries. Physiol Rev, 1978. 52: p. 397-460.

6. Schwartz E, A.A., Blumenfeld OO, Isolation and Characterization of the Internal Elastic Lamina from Calf Thoracic Aorta. Experimental and Molecular Pathology, 1981. 34(3): p. 299-306.

7. Sandow, S.L., D.J. Gzik, and R.M. Lee, Arterial internal elastic lamina holes: relationship to function? J Anat, 2009. 214(2): p. 258-66.

8. Kirby, B.S., et al., Robust internal elastic lamina fenestration in skeletal muscle arteries. PLoS One, 2013. 8(1): p. e54849.

9. Aiello, V.D., et al., Morphology of the internal elastic lamina in arteries from pulmonary hypertensive patients: a confocal laser microscopy study. Mod Pathol, 2003. 16(5): p. 411-6.

10. Bannister CM, M.L., Mundy JE, A scanning electron microscopy study of the endothelial folds in normal and anastomosed common carotid arteries in albino rats. Br J Exp Pathol, 1975. 56: p. 329-337.

11. Greensmith, J.E. and B.R. Duling, Morphology of the constricted arteriolar wall: physiological implications. Am J Physiol, 1984. 247(5 Pt 2): p. H687-98.

12. H Z Movat, N.V.F., The Fine Structure of the Terminal Vascular Bed' I. Small Arteries with an Internal Elastic Lamina. Experimental and Molecular Pathology, 1963. 2: p. 549-563.

13. Lee MM, C.S., Morphologic effects of pressure changes on canine carotid artery endothelium as observed by scanning electron microscopy. Anat Rec, 1979. 194: p. 1-14.

14. Mayberg MR, H.O., Sundt TM Jr., Ultrastructural changes in feline arterial endothelium following subarachnoid hemorrhage. J Neurosurg, 1978. 48: p. 49-57.

15. Schwartz SM, S.D., Chi EY, Surface replicas of aortic endothelium. Lab Invest, 1980. 42: p. 507-510.

16. Svendsen E, T.A., The circumferential length of the internal elastic membrane measured by computer digitizer morphometry, and its relation to in vivo aorta diameter. Acta Anat (Basel), 1983. 117: p. 145-151.

17. Svendson, E., Some characteristics of intimal folds in the rabbit aorta. Acta Anat (Basel), 1985. 124: p. 178-180.

18. Tindall AR, S.E., Intimal folds of the rabbit aorta. Acta Anat (Basel), 1982. 113: p. 169-177.

19. Svendsen. E., T.A.R., The Internal Elastic Membrane and Intimal Folds in Arteries: Important but Neglected Structures. Acta Physiologica Scandinavica, 1988. 133.

20. Burton, H.E., R.L. Williams, and D.M. Espino, Effects of freezing, fixation and dehydration on surface roughness properties of porcine left anterior descending coronary arteries. Micron, 2017. 101: p. 78-86.

21. Choy, J.S., O. Mathieu-Costello, and G.S. Kassab, The effect of fixation and histological preparation on coronary artery dimensions. Ann Biomed Eng, 2005. 33(8): p. 1027-33.

22. Paavilainen, L., et al., The impact of tissue fixatives on morphology and antibody-based protein profiling in tissues and cells. J Histochem Cytochem, 2010. 58(3): p. 237-46.

23. Davies PF, B.D., Scanning electron microscopy: arterial endothelial integrity after fixation at physiological pressure. Atherosclerosis, 1975. 21: p. 463-469.

24. Huang X, Y.C., Yuan C, Liu F, Canton G, Zheng J, Woodard PK, Sicard GA, Tang D, Patient-specific artery shrinkage and 3D zero-stress state in multi-component 3D FSI models for carotid atherosclerotic plaques based on in vivo MRI data. Mol Cell Biomech, 2009. 6: p. 121-134.

25. McGarvey KA, R.M., Roach MR, A quantitative study of the preparation of rabbit aortic endothelial cells for scanning electron microscopy. J Microsc, 1980. 118: p. 229-236.

26. Steinman J, K.M., Stefanovic B, Sled JG, 3D morphological analysis of the mouse cerebral vasculature: Comparison of in vivo and ex vivo methods. PLoS One, 2017. 12.

27. Swinehart PA, B.D., Kardong KV, Scanning electron microscopic study of the effects of pressure on the luminal surface of the rabbit aorta. Am J Anat, 1976. 145: p. 137-142.

28. Tindall A, S.E., Diameter changes in rabbit aorta during fixation at physiological pressure. Atherosclerosis, 1984. 50: p. 223-231.

29. Nguyen N; Nath N, D.L., Tzeng E, Velankar SS, Pocivavsek L, Wrinkling instabilities for biologically relevant fiber-reinforced composite materials with a case study of Neo-Hookean/Ogden-Gasser-Holzapfel bilayer. Biomech Model Mechanobiol, 2020. 19: p. 2375-2395.

30. A. Maud , R.K., L. M. Lin , O. M. Diaz , A. R. Vellipuram, S. Cruz-Flores , and G. J. Rodriguez, Internal Carotid Artery Dilatation Induced by General Anesthesia: Technical Observation. Journal of Vascular and Interventional Observation, 2018. 10.

31. Hiroki Iida, H.O., Mami Iida, Yukinaga Watanabe, Shuji Dohi, Isoflurane and Sevoflurane Induce Vasodilation of Cerebral Vessels via ATP-sensitive K+Channel Activation. Anesthesiology, 1998.

32. Ryu, K.H., et al., Comparison of vasodilatory properties between desflurane and sevoflurane using perfusion index: a randomised controlled trial. Br J Anaesth, 2020. 125(6): p. 935-942.

33. Slupe, A.M. and J.R. Kirsch, Effects of anesthesia on cerebral blood flow, metabolism, and neuroprotection. J Cereb Blood Flow Metab, 2018. 38(12): p. 2192-2208.

34. Sullender, C.T., et al., Dynamics of isoflurane-induced vasodilation and blood flow of cerebral vasculature revealed by multi-exposure speckle imaging. J Neurosci Methods, 2022. 366: p. 109434.

35. T, A., General anesthetics and vascular smooth muscle: direct actions of general anesthetics on cellular mechanisms regulating vascular tone. Anesthesiology, 2007.

36. Nath, N.N., et al., Dynamic Luminal Topography: A Potential Strategy to Prevent Vascular Graft Thrombosis. Front Bioeng Biotechnol, 2020. 8: p. 573400.

37. Pocivavsek, L., et al., Active wrinkles to drive self-cleaning: A strategy for anti-thrombotic surfaces for vascular grafts. Biomaterials, 2019. 192: p. 226-234.

38. Pitre, N.N., et al., Crimped fiber composites: mechanics of a finite-length crimped fiber embedded in a soft matrix. Biomech Model Mechanobiol, 2023. 22(3): p. 1083-1094.

39. Fratzl, P., Collagen: Structure and mechanics, an introduction. 2008. p. 1-13.

40. Kassab, G.S. and M.S. Sacks, Structure-based mechanics of tissues and organs. 2016. 1-469.

41. Gathercole, L.J. and A. Keller, Crimp Morphology in the Fibre-Forming Collagens. Matrix, 1991. 11(3): p. 214-234.

42. Diamant, J., et al., Collagen; ultrastructure and its relation to mechanical properties as a function of ageing. Proceedings of the Royal Society of London. Series B. Biological sciences, 1972. 180(60): p. 293-315.

43. Meyers, M.A., et al., Biological materials: Structure and mechanical properties. 2008. p. 1-206.

44. Fratzl, P., et al., Fibrillar Structure and Mechanical Properties of Collagen. Journal of Structural Biology, 1997. 122: p. 119-122.

45. Rigby, B.J., et al., The Mechanical Properties of Rat Tail Tendon. The Journal of General Physiology, 1959. 43: p. 265-283.

46. Canham, P.B., et al., Effect of pressure on circumferential order of adventitial collagen in human brain arteries. Canadian Journal of Physiology and Pharmacology, 1992. 70(2): p. 296-305.

47. Hilbert, S.L., et al., Simultaneous assessment of bioprosthetic heart valve biomechanical properties and collagen crimp length. Journal of Biomedical Materials Research, 1996. 31(4): p. 503-509.

48. Maqueda, I., S. Pellegrino, and J.M. Mejia-Ariza, Characterization of a high strain composite material. Collection of Technical Papers - AIAA/ASME/ASCE/AHS/ASC Structures, Structural Dynamics and Materials Conference, 2012: p. 1-12.

49. Muthukumar, M., et al., Mechanical behavior of unidirectional composites with hexagonal and uneven distribution of fibers in the transverse cross-section. Journal of Composite Materials, 2018. 52(22): p. 2985-3000.

50. Drach, B., D. Kuksenko, and I. Sevostianov, Effect of a curved fiber on the overall material stiffness. International Journal of Solids and Structures, 2016. 100-101: p. 211-222.

51. Freutel, M., Schmidt, H., Dürselen, L., Ignatius, A., Galbusera, F, Finite element modeling of soft tissues: Material models, tissue interaction and challenges. 2014. 29: p. 363-372.

52. Gasser, T.C., Ogden, R. W., Holzapfel, G. A., Hyperelastic modelling of arterial layers with distributed collagen fibre orientations. 2006. 3: p. 15-35.

53. Hiremath, C.P., et al., Numerical Study and Experimental Validation of Effect of Varying Fiber Crack Density on Stiffness Reduction in CFRP Composites. Journal of Materials Engineering and Performance, 2018. 27(4): p. 1685-1693.

54. López Jiménez, F. and S. Pellegrino, Constitutive modeling of fiber composites with a soft hyperelastic matrix. International Journal of Solids and Structures, 2012. 49(3-4): p. 635-647.

55. Politis, D., Finite Element Analysis of Tendon's Collagen Network in Three Dimensions. 2014.

56. Sun, C.T., Vaidya, R.S, Prediction of composite properties from a representative volume element. Compos Sci Technol 1996.

57. Krishan, K.C., Composite Materials: Science and Engineering [Book]. 2019. Chapter 2-3.

58. Freed, A.D. and T.C. Doehring, Elastic model for crimped collagen fibrils. Journal of Biomechanical Engineering, 2005. 127(4): p. 587-593.

59. Nezarati, R.M., et al., Electrospun vascular grafts with improved compliance matching to native vessels. Journal of Biomedical Materials Research - Part B Applied Biomaterials, 2015. 103(2): p. 313-323.

60. Ravi, S., Qu, Z., Chaikof, E. L., Polymeric materials for tissue engineering of arterial substitutes. 2009. 17.

61. Wang, F.J., et al., Promising poly(ε -caprolactone) composite reinforced with weft-knitted polyester for small-diameter vascular graft application. Advances in Materials Science and Engineering, 2014. 2014.

62. Hu, J.J., et al., Small-diameter vascular grafts composed of polyester/spandex fibers: Manufacturing techniques and property evaluations. Materials Letters, 2016. 171: p. 42-45.

63. Karkan, S.F., et al., Electrospun nanofibers for the fabrication of engineered vascular grafts. 2019, BioMed Central Ltd.

64. Zavan, B., et al., Electrospun pcl-based vascular grafts: In vitro tests. Nanomaterials, 2021. 11(3): p. 1-16.

65. Jeffries, E.M., et al., Highly elastic and suturable electrospun poly(glycerol sebacate) fibrous scaffolds. Acta Biomaterialia, 2015. 18: p. 30-39.

66. Chua, C.Y.X., et al., Carbon fiber reinforced polymers for implantable medical devices. Biomaterials, 2021. 271.

67. Vearick, S.B., et al., Fiber-reinforced silicone for tracheobronchial stents: An experimental study. Journal of the Mechanical Behavior of Biomedical Materials, 2018. 77: p. 494-500.

68. Stankus, J.J., et al., Hybrid nanofibrous scaffolds from electrospinning of a synthetic biodegradable elastomer and urinary bladder matrix. Journal of Biomaterials Science, Polymer Edition, 2008. 19(5): p. 635-652.

69. Fidan, I., et al., The trends and challenges of fiber reinforced additive manufacturing. International Journal of Advanced Manufacturing Technology, 2019. 102(5-8): p. 1801-1818.

70. Zampaloni, M., et al., Kenaf natural fiber reinforced polypropylene composites: A discussion on manufacturing problems and solutions. Composites Part A: Applied Science and Manufacturing, 2007. 38(6): p. 1569-1580.

71. Chang, H., et al., Recreating the heart ' s helical structure-function relationship with focused rotary jet spinning. 2022. 000(0000): p. 1-6.

72. Chazeau, L., et al., Relationships between microstructural aspects and mechanical properties in polymer based nanocomposites To cite this version : HAL Id : hal-02917761 Please cite as : Relationships between microstructural aspects and mechanical properties in polymer based. 2020.

73. Utracki, L.A., Clay-containing polymeric nanocomposites and their properties. IEEE Electrical Insulation Magazine, 2010. 26(4): p. 8-17.

74. Loos, M.R. and I. Manas-Zloczower, Micromechanical models for carbon nanotube and cellulose nanowhisker reinforced composites. Polymer Engineering and Science, 2013. 53(4): p. 882-887.

75. De, S.K.a.W., J.R., Short Fibre-Polymer Composites. 1996, Cambridge, Englang: Woodhead Publishing.

76. Ratner, B., Hoffman, AS., Shoen, FJ., Lemons, JE, BIOMATERIALS SCIENCE An Introduction to Materials in Medicine 2nd Edition. 2004: Elsevier Academic Press.

77. Zhong, W., et al., Short fiber reinforced composites for fused deposition modeling. Materials Science and Engineering A, 2001. 301(2): p. 125-130.

78. Shao Yun Fu, B.l., Science and engineering of short fi bre reinforced polymer composites Related titles.

79. Young, R.J., Composite micromechanics: From carbon fibres to graphene, in Woodhead Publishing Series in Composites Science and Engineering, Structural Integrity and Durability of Advanced Composites, C.S. P.W.R. Beaumont, A. Hodzic, Editor. 2015, Woodhead Publishing. p. 3-23.

80. Komal, U.K., Lila, M. K., Chaitanya, S., Singh, I, Fabrication of Short Fiber Reinforced Polymer Composites, in Reinforced Polymer Composites: Processing, Characterization and Post Life Assessment, P.K.a.S. Bajpai, I, Editor. 2019, Wiley.

81. Huang, Z.M., et al., Tensile strength prediction of short fiber reinforced composites. Materials, 2021. 14(11).

82. Peel, L.D. and D.W. Jensen, Response of fiber-reinforced elastomers under simple tension. Journal of Composite Materials, 2001. 35(2): p. 96-137.

83. Curtin, W.A.a.t., N., tensile strength of fiber reinforced composites: application to polymer matrix composites. Composite Materials, 1998. 32.

84. Fu, S.Y.L., B.; Mai, Y. W., Science and Engineering of Short Fibre Reinforced Polymer Composites, ed. B.M. Lauke, Y. W. 2009: Elsevier Science.

85. Hull, D.a.C., T. W., Introduction to Composite Materials 2nd edition. 1996.

86. Cox, H.L., The elasticity and strength of paper and other fibrous materials. British Journal of Applied Physics, 1952. 3(3): p. 72-79.

87. Maas SA, E.B., Ateshian GA, Weiss JA, FEBio: Finite elements for biomechanics. Journal of Biomechanical Engineering, 2012. 134(1).

88. Holzapfel, G.A., Gasser, T.C. & Ogden, R.W, A New Constitutive Framework for Arterial Wall Mechanics and a Comparative Study of aterial Models. Journal of Elasticity, 2000. 61: p. 1-48.

89. Yixin Hu, T.S., Bolun Wang, Denis Zorin, Daniele Panozzo, Fast Tetrahedral Meshing in the Wild. ACM Trans. Graph, 2020. 39.

90. Maas, S.A., et al., FEBio: finite elements for biomechanics. J Biomech Eng, 2012. 134(1): p. 011005.

91. Nolan, D.R., et al., A robust anisotropic hyperelastic formulation for the modelling of soft tissue. J Mech Behav Biomed Mater, 2014. 39: p. 48-60.

92. Dai, J., et al., Mechanical Properties of Aortic Artery by Uniaxial Tensile Tests under Physiological Condition, in 4th International Conference on Biometric Engineering and Applications. 2021. p. 98-103.

93. G, A.I.A., et al., Methodology for Mechanical Characterization of Soft Biological Tissues: Arteries. Procedia Engineering, 2015. 110: p. 74-81.

94. Liyanage, L., et al., Multimodal Structural Analysis of the Human Aorta: From Valve to Bifurcation. Eur J Vasc Endovasc Surg, 2022. 63(5): p. 721-730.

95. Pal, S., et al., A mechanistic model on the role of "radially-running" collagen fibers on dissection properties of human ascending thoracic aorta. J Biomech, 2014. 47(5): p. 981-8.

96. Tsamis, A., N. Stergiopulos, and A. Rachev, A structure-based model of arterial remodeling in response to sustained hypertension. J Biomech Eng, 2009. 131(10): p. 101004.

97. Eskandari, M. and E. Kuhl, Systems biology and mechanics of growth. Wiley Interdiscip Rev Syst Biol Med, 2015. 7(6): p. 401-12.

98. Wu, J.Z., et al., A structural fingertip model for simulating of the biomechanics of tactile sensation. Med Eng Phys, 2004. 26(2): p. 165-75.

99. Iwasaki, S.I., et al., Comparative morphology of the primate tongue. Ann Anat, 2019. 223: p. 19-31.

100. Budday, S., P. Steinmann, and E. Kuhl, The role of mechanics during brain development. J Mech Phys Solids, 2014. 72: p. 75-92.

101. Xie, Q., et al., Dynamic surface antifouling: mechanism and systems. Soft Matter, 2019. 15(6): p. 1087-1107.

102. Shyer, A.E., et al., Villification: how the gut gets its villi. Science, 2013. 342(6155): p. 212-8.

103. Shepard, J.O., E.J. Flores, and G.F. Abbott, Imaging of the trachea. Ann Cardiothorac Surg, 2018. 7(2): p. 197-209.

104. Monkhouse, W.S. and W.F. Whimster, An account of the longitudinal mucosal corrugations of the human tracheo-bronchial tree, with observations on those of some animals. J. Anatomy, 1976. 122: p. 681-695.

105. Morrow;, j.B., et al., The Ringed Esophagus: Histological Features of GERD. American Journal of Gastronomy, 2001. 96: p. 984-989.

106. Fu, Y.F., C.Q. Yuan, and X.Q. Bai, Marine drag reduction of shark skin inspired riblet surfaces. Biosurface and Biotribology, 2017. 3(1): p. 11-24.

107. Allen, J.J., et al., Comparative morphology of changeable skin papillae in octopus and cuttlefish. J Morphol, 2014. 275(4): p. 371-90.

108. Allen, J.J., et al., Cuttlefish use visual cues to control three-dimensional skin papillae for camouflage. J Comp Physiol A Neuroethol Sens Neural Behav Physiol, 2009. 195(6): p. 547-55.

109. Gonzalez-Bellido, P.T., et al., Neural Control of Dynamic 3-Dimensional Skin Papillae for Cuttlefish Camouflage. iScience, 2018. 1: p. 24-34.

110. Richards, C., et al., Bio-inspired Surface Texture Modification as a Viable Feature of Future Aquatic Antifouling Strategies: A Review. Int J Mol Sci, 2020. 21(14).

111. Bozzoli, F., L. Cattani, and S. Rainieri, Effect of wall corrugation on local convective heat transfer in coiled tubes. International Journal of Heat and Mass Transfer, 2016. 101: p. 76-90.

112. Tadimeti, J.G.D., et al., Corrugated membrane surfaces for effective ion transport in electrodialysis. Journal of Membrane Science, 2016. 499: p. 418-428.

113. Zhang, H., et al., Experimental study of heat transfer performance in a mini-corrugated pipe coupling nanofluids and pulsating wave. Powder Technology, 2023. 426.

114. Abu Talib, A.R. and A.K. Hilo, Fluid flow and heat transfer over corrugated backward facing step channel. Case Studies in Thermal Engineering, 2021. 24.

115. Bowden, N., et al., The controlled formation of ordered, sinusoidal structures by plasma oxidation of an elastomeric polymer. Applied Physics Letters, 1999. 75(17): p. 2557-2559.

116. Bowden, N.B., Scott ; Evans, Anthony G. ; Hutchinson, John W. ; Whitesides, George M., Spontaneous formation of ordered structures in thin films of metals supported on an elastomeric polymer. Nature, 1998. 393: p. 146-149.

117. Chen, Y., et al., Post-wrinkling behaviors of a bilayer on a soft substrate. International Journal of Solids and Structures, 2021. 214-215: p. 74-79.

118. Efimenko, K., W.E. Wallace, and J. Genzer, Surface modification of Sylgard-184 poly(dimethyl siloxane) networks by ultraviolet and ultraviolet/ozone treatment. J Colloid Interface Sci, 2002. 254(2): p. 306-15.

119. Huck, W.T., Bowden, N.B., Onck, P.R., Pardoen, T., Hutchinson, J.W., & Whitesides, G.M. , Ordering of Spontaneously Formed Buckles on Planar Surfaces. Langmuir, 2000. 16: p. 3497-3501.

120. Jeong, J., et al., Topography-guided buckling of swollen polymer bilayer films into three-dimensional structures. Soft Matter, 2017. 13(5): p. 956-962.

121. Surapaneni, V.A., et al., Groovy and Gnarly: Surface Wrinkles as a Multifunctional Motif for Terrestrial and Marine Environments. Integr Comp Biol, 2022. 62(3): p. 749-61.

122. Kim, J.W., et al., Effect of surface tension on elastocapillary wrinkling of interfacially adsorbed hydrogel disks with photothermally programmed swelling profiles. Soft Matter, 2023. 19(20): p. 3543-3550.

123. Chiche, A.S., Christopher & Cabral, João, Complex micropatterning of periodic structures on elastomeric surfaces. Soft Matter, 2008. 4.

124. Takei, A., et al., High-Aspect-Ratio Ridge Structures Induced by Plastic Deformation as a Novel Microfabrication Technique. ACS Appl Mater Interfaces, 2016. 8(36): p. 24230-7.

125. Yang, J., et al., Stretching-induced wrinkling in plastic-rubber composites. Soft Matter, 2017. 13(4): p. 776-787.

126. Susanna, G., et al., Airbrush spray-coating of polymer bulk-heterojunction solar cells. Solar Energy Materials and Solar Cells, 2011. 95(7): p. 1775-1778.

127. Huang, Z.Y., W. Hong, and Z. Suo, Nonlinear analyses of wrinkles in a film bonded to a compliant substrate. Journal of the Mechanics and Physics of Solids, 2005. 53(9): p. 2101-2118.

128. Hanqing Jiang, D.-Y.K., Jizhou Song, Yugang Sun, Yonggang Huang and J.A.R. , Finite deformation mechanics in buckled thin films on compliant supports. Proc Natl Acad Sci U S A, 2007.

129. Fujiyama, H., Inner coating of long-narrow tube by plasma sputtering. Surface and coatings technology, 2000. 131: p. 278-283.

130. Nagata;, K., et al., Method and apparatus for coating the inner surface of long tubes of small diameter, E.P. Office, Editor. 1981.

131. W Ensinger, K.V., B Enders, Inner wall coating of cylinders by plasma immersion ion implantation for corrosion protection. Surface and coatings technology, 2001. 136: p. 202-206.